



**SAMUEL WILLIAM MURPHY**

**“INFRARED MONITORING OF VOLCANOES FROM SPACE”**

***“MONITORAMENTO ORBITAL DE VULCÕES NO ESPECTRO INFRAVERMELHO”***

**CAMPINAS**

**2013**





NÚMERO: 461/2013

UNIVERSIDADE ESTADUAL DE CAMPINAS  
INSTITUTO DE GEOCIÊNCIAS

SAMUEL WILLIAM MURPHY

“INFRARED MONITORING OF VOLCANOES FROM SPACE”  
“*MONITORAMENTO ORBITAL DE VULCÕES NO ESPECTRO INFRAVERMELHO*”

Tutor/ Orientador: Prof. Dr. Carlos Roberto de Souza Filho

Co-Tutor/ Co-Orientador: Prof. Dr. Clive Matthew Martin Oppenheimer

THIS THESIS WAS PRESENTED TO THE INSTITUTE OF GEOSCIENCES AT  
THE UNIVERSITY OF CAMPINAS FOR THE PURPOSE OF OBTAINING A  
DOCTORATE IN GEOLOGY NATURAL RESOURCES.

*TESE DE DOUTORADO APRESENTADA AO INSTITUTO DE GEOCIÊNCIAS  
DA UNIVERSIDADE ESTADUAL DE CAMPINAS PARA OBTENÇÃO DO  
TÍTULO DE DOUTOR EM CIÊNCIAS NA ÁREA DE GEOLOGIA E RECURSOS  
NATURAIS.*

ESTE EXEMPLAR CORRESPONDE À VERSÃO  
FINAL DA TESE DEFENDIDA PELO ALUNO  
SAMUEL WILLIAM MURPHY E ORIENTADO PELO  
PROF. DR CARLOS ROBERTO DE SOUZA FILHO

---

CAMPINAS

2013

FICHA CATALOGRÁFICA ELABORADA POR  
CÁSSIA RAQUEL DA SILVA – CRB8/5752 – BIBLIOTECA “CONRADO PASCHOALE” DO  
INSTITUTO DE GEOCIÊNCIAS  
UNICAMP

M951i Murphy, Samuel William, 1985-  
Infrared Monitoring of Volcanoes from Space /  
Samuel William Murphy-- Campinas,SP.: [s.n.], 2013.

Orientador: Carlos Roberto de Souza Filho.  
Co-orientador: Clive Matthew Matrin Oppenheimer  
Tese (doutorado) - Universidade Estadual de  
Campinas, Instituto de Geociências.

1. Sensoriamento remoto. 2. Vulcões. I. Souza Filho,  
Carlos Roberto de, 1965- II. Oppenheimer, Clive Matthews  
Martin. III. Universidade Estadual de Campinas, Instituto de  
Geociências. IV. Título.

Informações para a Biblioteca Digital

**Título em português:** Monitoramento orbital de vulcões no espectro infravermelho

**Palavras-chaves em inglês:**

Remote sensing

Volcanoes

**Área de concentração:** Geologia e Recursos Naturais

**Títuloção:** Doutor em Ciências

**Banca examinadora:**

Carlos Roberto de Souza Filho (Orientador)

Alberto Waingort Setzer

Jurandir Zullo Junior

Paulo Roberto Meneses

Teodoro Almeida

**Data da defesa:** 31/01/2013

Programa de Pós-graduação em Geociências



UNIVERSIDADE ESTADUAL DE CAMPINAS  
INSTITUTO DE GEOCIÊNCIAS  
PÓS-GRADUAÇÃO EM GEOCIÊNCIAS NA  
ÁREA DE GEOLOGIA E RECURSOS NATURAIS

**AUTOR:** Samuel William Murphy

“Infrared Monitoring of Volcanoes from Space”.

**ORIENTADOR:** Prof. Dr. Carlos Roberto de Souza Filho

**CO-ORIENTADOR:** Prof. Dr. Clive Matthew Martin Oppenheimer

Aprovado em: 31 / 01 / 2013

**EXAMINADORES:**

Prof. Dr. Carlos Roberto de Souza Filho

Carl R. S. Filho - Presidente

Prof. Dr. Jurandir Zullo Junior

Jurandir Zullo Junior

Prof. Dr. Teodoro Isnard Ribeiro de Almeida

Teodoro Isnard Ribeiro de Almeida

Prof. Dr. Alberto Waingort Setzer

Alberto Waingort Setzer

Prof. Dr. Paulo Roberto Meneses

Paulo Roberto Meneses

Campinas, 31 de janeiro de 2013.



This thesis is dedicated to my Great-Uncle Gerry,  
a gentleman and a hero.



## Acknowledgements

There are many people that I would like to thank. They made the creation of this thesis possible and its fruition a fulfilling one.

Carlos Roberto de Souza Filho has been such an excellent supervisor that I have frequently reflected on my tremendous good fortune in having been his PhD student. The faith and encouragement showed by Clive Oppenheimer has and continuous to be of extreme importance to me. I am exceedingly thankful to Robert Wright for allowing me to visit him at the Hawaiian Institute of Geophysics and Planetology (HIGP) during a 4 month stay in the spring of 2011 (mahalo nui loa).

This work was kindly supported by various funding bodies in Brazil. The national agency *Coordenação de Aperfeiçoamento de Pessoal de Nível Superior* (CAPES) provided me with a post-graduate scholarship, *Conselho Nacional de Desenvolvimento Científico e Tecnológico* (CNPq) for the resources requires to work abroad, whilst local support was also provided by *Fundo de Apoio ao Ensino à Pesquisa e Extensão* (FAEPEX) and *Pró-Reitoria de Pós-Graduação* (PRPG) of the University of Campinas to attend conferences and an international short course on volcanology.

My colleagues here at the University of Campinas are numerous. My respects go to the *velha guarda*: Juliano Senna, Aloisio Cotta, Clemente Macia, Marcus Vasconcelos (Marquinhos), Tatiana Geler, Lucíola Magalhães, Wagner Amaral (Lobinho), Oderson de Souza Filho, as well as to some of the newer crew: Cecilia Nascimento, Drielli Peyerl, Renan Leonel, Paulo Locatelli, José Henrique Mattos (Zé), Danilo Barbuena, Monica!, Thiara Breda, Ethiane Agnoletto, Lucas Silva, Gustavo Melo (Cebola), Marco Delinardo, Maria Isabel Martins (Bel).

A special mention goes to my friends in room 5, both the girls: Mariana, Rosa, Juanita and Flávia, and the boys: Tom and Adelson

Aunty Luzia and my cousin Patrícia played a crucial role in helping me settle into Campinas, including a lengthy stay at their house. Your kindness has been life changing.

Finally thank you to my parents for your kind thoughts and encouragement.



# Samuel William Murphy



Samuel Murphy graduated from the University of Bristol (UK) with a Master in Science in Geology (2003 - 2007). In 2008 he went on to begin his first postgraduate study, on the Remote Sensing of active volcanoes, supervised by Dr. Carlos Robert de Souza Filho (University of Campinas, Brazil) and Prof. Clive Oppenheimer (University of Cambridge, UK).

In 2011 he spent a four month period as a visiting researcher at the University of Hawaii at Manoa where he worked with Dr. Robert Wright on developing synergies between satellite sensors.

He successfully concluded a doctoral study (*Doutorado Direto*) in January 2013.

During his research career Samuel has published in the top journals in both the fields of ‘Remote Sensing’ and ‘Volcanology’, i.e. *Remote Sensing of Environment* and *Journal of Volcanology and Geothermal Research*. He has also presented work at international conferences and workshops in Brazil, USA, Mexico and Italy.



It is not what we have but what we enjoy that constitutes our abundance.

Epicurus  
(BC 341-270)





UNIVERSIDADE ESTADUAL DE CAMPINAS  
INSTITUTO DE GEOCIÊNCIAS

**MONITORAMENTO ORBITAL DE VULCÕES NO ESPECTRO INFRAVERMELHO**

**RESUMO**

**Tese de Doutorado**

**Samuel William Murphy**

O monitoramento de vulcões é necessário para a mitigação do perigo que apresentam à sociedade. Esse monitoramento pode ser feito em uma escala global através de satélites. Foi com essa finalidade que este doutorado visou desenvolver metodologias para o monitoramento das atividades termais dos vulcões observados do espaço. Chegou-se a isso através do uso de uma variedade de sensores infravermelhos orbitais. Foi utilizado o sensor *Advanced Spaceborne Thermal Emission and Reflection Radiometer* (ASTER), que oferece imagens de moderada a alta resolução espacial (30 – 90 m) no infravermelho das ondas curtas (SWIR) e infravermelho termal (TIR), a fim de caracterizar o tamanho e a intensidade das anomalias termais. As bandas do TIR do ASTER conseguiram detectar anomalias súteis, o que permitiu a observação de novos precursores termais antes das erupções. O *Moderate Resolution Imaging Spectroradiometer* (MODIS) oferece imagens de alta resolução temporal (i.e. cobertura global diária), por isto foi utilizado para investigar atividade termal através do tempo. A análise de *wavelets* foi utilizado para quantificar os períodos de oscilação de tal atividade. Hyperion é um espectroradiômetro imageador e foi utilizado para demonstrar uma nova metodologia para calcular fluxo radiante de alvos termalmente heterogêneos (i.e. vulcões). Essas metodologias utilizam as melhores resoluções de cada um dos sensores: espacial (ASTER), temporal (MODIS), espectral (Hyperion) podem ser automaticamente executadas em escala global. Essa tese visa portanto apresentar uma fundação sólida onde futuros sistemas de monitoramento de vulcões podem ser baseados.

**Palavras chaves: Sensoriamento Remoto, Vulcões**





**UNIVERSITY OF CAMPINAS  
INSTITUTE OF GEOSCIENCE**

## **INFRARED MONITORING OF VOLCANOES FROM SPACE**

### **ABSTRACT**

#### **PhD Thesis**

**Samuel William Murphy**

Volcanoes need to be monitored to mitigate the risk that they pose to society. This can be done on a global scale using satellite sensors. The goal of this doctorate was to develop methods for the monitoring of volcanic thermal activity from space. This was achieved through the use of a variety of orbital infrared sensors. The Advanced Spaceborne Thermal Emission and Reflection Radiometer (ASTER), which offers moderate to high spatial resolution imagery (30 – 90 m) in the short-wave infrared (SWIR) and thermal infrared (TIR), was used to characterize the size and intensity of thermal anomalies. Its TIR channels were capable of detecting subtle thermal anomalies. This permitted the observation of new thermal precursors to eruptive events. The Moderate Resolution Imaging Spectroradiometer (MODIS) offers high temporal resolution imagery (i.e. daily global coverage). It was therefore used to investigate thermal activity through time. Wavelet analysis was used to quantify the time period over which such activity oscillates. Hyperion is an orbiting imaging spectrometer. It was used to demonstrate a new method for calculating radiant flux from thermally heterogeneous targets (i.e. such as volcanoes). These methods utilized the strengths of each sensor system, i.e. high spatial, temporal or spectral resolution. They all improve the ability to detect and/or quantify thermal anomalies from space and can be executed in an automated global basis. This thesis therefore presents a solid foundation on which the next generation global volcano monitoring system can be based.

**Keywords: Remote Sensing, Volcanoes**



# Index

---

<i>Capítulo 1. Introdução (em português)</i> .....	1
Chapter 1. Introduction.....	7
Chapter 2. Scientific Context .....	13
2.1. Observing Volcanoes from Space.....	13
2.1.1. Thermal Emission.....	15
2.1.2. Gas Plumes.....	18
2.1.3. Ash Clouds.....	19
2.1.4. Geometry.....	20
2.1.5. Mapping eruptive products.....	21
2.2. Physical Principals.....	21
2.3. Temperature, Emissivity and Blackbodies.....	28
2.4. Atmospheric Effects.....	29
2.5. Issues with infrared monitoring of volcanoes from space.....	31
2.6. Aim of this work.....	34
Chapter 3. Monitoring Volcanic Thermal Anomalies from Space: Size Matters.....	35
3.1. Abstract.....	35
3.2. Introduction.....	36
3.3. Study Areas.....	37
3.3.1. Erebus volcano.....	37
3.3.2. Láscar volcano.....	38
3.4. ASTER and data processing.....	39
3.4.1. Background areas.....	40
3.4.2. Radius pairs.....	43
3.4.3. Background temperatures.....	46
3.5. Anomalous volcanic temperatures.....	48

3.5.1. Anomalously hot pixels.....	49
3.5.2. The spatial extent of thermal anomalies.....	51
3.5.3. SWIR anomalies.....	51
3.6. Results.....	52
3.6.1. Maximum temperatures above background.....	52
3.6.2. The spatial extent of thermal anomalies.....	57
3.6.2.1. Erebus.....	58
3.6.2.2. Láscair.....	60
3.7. Discussion.....	63
3.7.1. Scatter in maximum $\Delta T$ at Erebus.....	63
3.7.2. Background temperatures at other volcanoes.....	66
3.7.3. Monitoring implications.....	67
3.8. Conclusion.....	68
Chapter 4. MODIS and ASTER Synergy for Characterizing Thermal Volcanic Activity ..	69
4.1. Abstract.....	69
4.2. Introduction.....	70
4.3. Study areas.....	73
4.4. Metrics for volcanic thermal activity.....	73
4.4.1. MOD* (High temporal resolution volcanic radiance) .....	73
4.4.2. AST* (Size of anomalous areas) .....	77
4.5. Wavelet analysis.....	80
4.6. Results.....	81
4.6.1. Time series.....	81
4.6.2. Wavelet power spectra .....	87
4.7. Discussion.....	90
4.8. Conclusion.....	91

Chapter 5. Calculating Radiant Flux from Thermally Mixed Pixels.....	93
5.1. Abstract.....	93
5.2. Introduction.....	94
5.3. Existing methods for calculating radiant flux.....	96
5.3.1. Dozier Technique.....	96
5.3.2. Wooster Technique.....	97
5.3.3. Model-fitting approach.....	98
5.4. Reliability of radiant flux estimates.....	99
5.5. A spectral library approach.....	100
5.6. Monte Carlo testing.....	102
5.7. Hyperion data processing .....	103
5.8. Results.....	104
5.8.1. Monte Carlo runs.....	104
5.8.2. Radiant flux from a lava flow at Kliuchevskoi, Russia.....	107
5.9. Discussion.....	109
5.10 Conclusion.....	109
 Chapter 6. Future Prospects and Conclusion.....	 111
6.1. Recapitulation .....	111
6.2. Future of infrared sensors .....	113
6.2.1. High spatial resolution missions .....	114
6.2.2. High temporal resolution missions .....	114
6.2.3. Non-governmental satellite sensors .....	115
6.2.4. Unmanned Aerial Vehicles.....	115
6.2.5. User demand.....	116
6.3. Conclusions .....	116

<i>Capítulo 6. Perspectivas Futuras e Conclusões</i> .....	119
6.1. <i>Recapitulação</i> .....	119
6.2. <i>Futuros Sensores Infravermelhos</i> .....	121
6.2.1. <i>Missões de alta resolução espacial e espectral</i> .....	121
6.2.2. <i>Missões de alta resolução temporal</i> .....	123
6.2.3. <i>Sensores não governamentais</i> .....	123
6.2.4. <i>Veículos aéreos não tripulados (VANTs)</i> .....	124
6.2.5. <i>Demanda do usuário</i> .....	124
6.3. <i>Conclusões</i> .....	125
References .....	127

## List of Figures

---

- 1.1. Volcanic ash plume traversing South America as seen by MODIS
- 2.1. A schematic of polar and geostationary orbits.
- 2.2. Example of exitance (M) and irradiance (E)
- 2.3. Divergence of photon trajectories controlling loss of irradiance with distance
- 2.4. Examples of solid cone geometries
- 2.5. Decrease in projected source area with angular distance from normal
- 2.6. An infinitesimal area on a hemisphere
- 3.1. Location of Mount Erebus, Antarctica
- 3.2. Location of Láscar Volcano, Chile
- 3.3. Box-shaped background areas at Erebus and Láscar
- 3.4. Sample background temperature from box-shaped background areas at Erebus and Láscar
- 3.5. Average deviation in background temperatures from ring-shaped areas at non-active topographic peaks
- 3.6. Average deviation in background temperatures from ring-shaped areas at Erebus and Láscar

- 3.7. The size and location of the optimal ring-shaped background area at Erebus and Láscar
- 3.8. Time series of background temperatures at Erebus and Láscar
- 3.9. Probability density functions of background z-scores at Erebus and Láscar
- 3.10. Time series of maximum temperature above background at Erebus and Láscar
- 3.11. Photograph of Láscar's collapsed crater (taken on 10<sup>th</sup> December 2009)
- 3.12. Time series of the size of thermal anomalies at Erebus and Láscar
- 3.13. A vaporous plume at Erebus as seen through VNIR, SWIR and TIR derived images.
- 3.14. Thermal precursor to Láscar eruption as depicted by an increase in high temperature events
- 3.15. Another thermal precursor to an eruption at Láscar as shown by a dip in moderate and high temperature anomalies.
- 3.16. Graph showing the effect of subpixel mixing on ASTER temperature retrievals.
- 4.1. Histograms of Normalized Thermal Index (NTI) at a) Erta 'Ale, c) Kīlauea, c) Kliuchevskoi, and d) Láscar.
- 4.2. Anomaly frequency maps at a) Erta 'Ale, c) Kīlauea, c) Kliuchevskoi, and d) Láscar.
- 4.3. Time series of MOD\* at a) Erta 'Ale, c) Kīlauea, c) Kliuchevskoi, and d) Láscar.
- 4.4. Comparison of ASTER and MODIS spatial resolution
- 4.5. Thermal precursor to lava flow at Kliuchevskoi

4.6. Example of ASTER's ability to detect relatively subtle thermal anomalies compared to MODIS

4.7. Wavelet transforms of MOD\* time series

4.8. Time slices from wavelet transforms

5.1. The model fitting accuracy of the spectral library approach for a) 'current-class' and b) 'future-class' sensors

5.2. Accuracy of radiant flux estimates using the spectral library approach

5.3. Accuracy of 3-component temperature solutions using the spectral library approach

5.4. Accuracy of 3-component subpixel area solutions using the spectral library approach

5.5. Radiant flux maps of a lava flow at Kliuchevskoi

## List of Tables

---

2.1. Orbital sensors used for infrared observations of volcanoes

3.1. Model fit parameters of background temperatures at Erebus and Láscar

5.1. The central wavelengths used to create the spectral libraries

6.1. Up and coming, state-funded satellites of use for infrared volcano monitoring.

## Acronyms and Abbreviations

---

AST*	ASTER metric of thermal anomaly size
AST_09T	ASTER surface leaving TIR product
ASTER	Advanced Spaceborne Thermal Emission and Reflection Radiometer
ATSR	Along Track Scanning Radiometer
AVHRR	Advanced Very-High Resolution Radiometer
AVIRIS	Airborne Visible/Infrared Imaging Spectrometer
AVO	Alaska Volcano Observatory
BET EF	Bayesian event tree model for eruption forecasting
BGVN	Bulletin of the Global Volcanism Network
BT	brightness temperature
BT*	thermally anomalous brightness temperature
DEM	Digital Elevation Model
DN	digital number(s)
EnMap	Environmental Mapping and Analysis Program
EO-1	Earth Observing 1
ERS	European Remote Sensing Satellite
ESA	European Space Agency
FLIR	Forward-looking infrared
GIS	Geographical Information Systems
GLONASS	‘Globalnaya Navigatsionnaya Sputnikovaya Sistema’ (in Russian) or ‘Global Navigation Satellite System’ (in English)
GOES	Geostationary Operational Environmental Satellite
GPS	Global Positioning System
HCl	hydrogen chloride
HF	hydrogen fluoride
HRIS	High Resolution Infrared Radiometer
HypsIRI	Hyperspectral Infrared Imager

IFOV	Instantaneous Field of View
InSAR	Interferometric Synthetic Aperture Radar
IR	infrared
JERS	Japanese Earth Resource Satellite
JMA	Japanese Meteorological Agency
JPSS	Joint Polar Satellite System
L1a	ASTER data processing level 1a
L1b	ASTER data processing level 1b
LAADS	Level 1 and Atmosphere Archive and Distribution System
LP DAAC	Land Processes Distributed Active Archive Center
MAPD	mean absolute proportional difference
MIR	mid infrared
MOD*	MODIS metric of volcanic radiance at approximately 4 microns
MOD021KM	MODIS data product of calibrated radiance (Terra satellite)
MOD03	MODIS geolocation product (Terra satellite)
MODIS	Moderate Resolution Imaging Spectroradiometer
MODTRAN	Moderate Resolution Atmospheric Transmission
MODVOLC	MODIS global thermal volcano monitoring product
MSG	Meteosat Second Generation
MTSAT	Multi-Functional Transport Satellite
NASA	National Aeronautics and Space Administration
NEM	Normalized Emissivity Method
NEAT	noise equivalent temperature variation
NOAA	National Oceanic and Atmospheric Administration
NPP	National Polar-orbiting Partnership
NTI	Normalized Thermal Index
OMI	Ozone Monitoring Instrument
OPS	Optical Sensor (on JERS)
PDF	probability density function
RAT	Robust AVHRR Technique
RST	Robust Satellite Technique

SEVIRI	Spinning Enhanced Visible and Infrared Imager
SRTM	Shuttle Radar Topography Mission
SWIR	shortwave infrared
TES	Temperature Emissivity Separation (i.e. a specific algorithm; Gillespie et al. 1998)
TIR	thermal infrared
UTC	Coordinated Universal Time
UV	ultraviolet
VIIRS	Visible Infrared Imager Radiometer Suite
VNIR	visible and near infrared
$\Delta T$	temperature above background



# Capítulo 1

## Introdução

---

A Terra é um sistema dinâmico. O desequilíbrio termodinâmico entre o interior e a crosta terrestre, leva a uma transferência de energia (calor) do interior em direção à crosta. Esta transferência de energia térmica em escala planetária manifesta-se mais claramente sob a forma de vulcões. Dada à magnitude desse processo, os vulcões desempenham múltiplas influências dentro do sistema terrestre e são essenciais para a compreensão do funcionamento do nosso planeta.

Ao longo da história geológica a atividade vulcânica tem provocado efeitos dramáticos sobre a composição da atmosfera, o clima da Terra, a extinção de espécies e a concentração de minerais no que, ao longo do tempo, tornou-se o que são agora corpos de minério. Os depósitos vulcânicos também oferecem informações valiosas sobre a dinâmica e composição interna da Terra através do tempo, especialmente por estes depósitos serem nossas únicas fontes de amostras do manto. Entretanto é evidente que a atividade vulcânica contemporânea também apresenta uma série de riscos para a sociedade, incluindo a perda de vidas humanas e graves impactos na economia e infraestrutura.

Grande parte dos vulcões ativos não possuem um programa de monitoramento específico, uma vez que as escalas de tempo vulcânicas frequentemente parecem longas quando comparadas às escalas de tempo humanas e os vulcões estão localizados em diferentes locais do globo. No entanto, existem cerca de 20 erupções ocorrendo simultaneamente e, tipicamente, cerca de 60 erupções ocorrem por ano no mundo. Esta lacuna no monitoramento apresenta perigo e poderá

resultar na perda de vida e bens materiais que seriam evitáveis com um monitoramento mais aperfeiçoado. Neste cenário, os sensores espaciais fornecem o único meio de preencher esta lacuna em escala global.

O perigo causado pela atividade vulcânica é um problema global que, direta ou indiretamente, afeta uma grande parte da população mundial. Considerando através de uma perspectiva sul-americana, vemos que a maioria da costa ocidental deste continente é ativa. Isso é ocasionado principalmente pela subducção da placa de Nazca sob a placa Sul-americana e tem implicações para todo o continente, já que áreas vastas podem ser afetadas por plumas de cinzas vulcânicas. Um exemplo é a erupção de 1993 do Lászar (Chile) que causou a queda de tephra (i.e. cinzas vulcânicas) em Porto Alegre (Brasil) apesar da distância de 1800 km. Mais recentemente (i.e. junho de 2011), a atividade do vulcão Puyehue (Chile) formou uma nuvem de cinzas que foi do Chile e atravessou a Argentina chegando até ao Oceano Atlântico (Fig. 1.1).

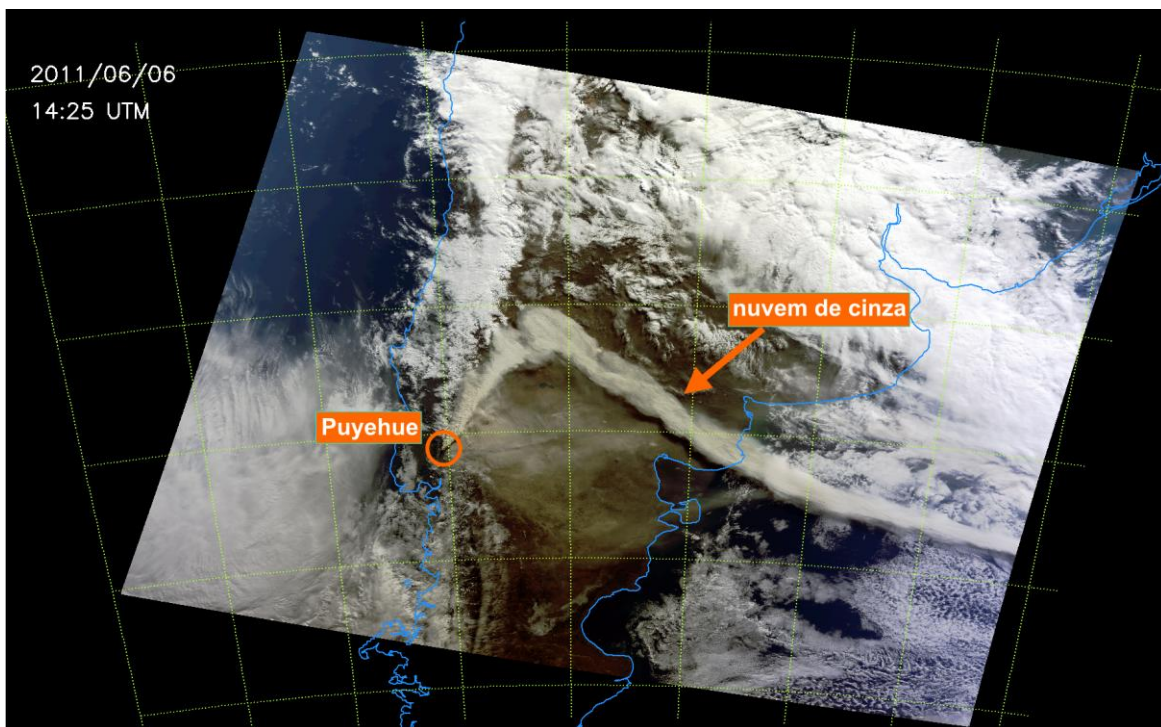


**Figura 1.1.** Imagem de MODIS (cor verdadeira) da erupção de Puyehue (Chile) em junho de 2011. A nuvem de cinzas viajou NNE e depois ESE, atravessando a Argentina. Voos foram cancelados na Argentina, Brasil e outros países sul-americanos.

Como resultado, voos de chegada e partida do aeroporto internacional de Buenos Aires (situado cerca de 1400 km de distância do vulcão) foram cancelados, incluindo aqueles com embarque de passageiros brasileiros. A tendência é que transtornos como esses ocorram com mais frequência no futuro, devido à crescente densidade do tráfego aéreo na região. A consequência de tais atividades vulcânicas pode incluir enormes danos financeiros gerados pelo impacto adverso nos negócios e comércio. Um exemplo é a parada do espaço aéreo europeu por vários dias em março de 2010, em função da erupção do Eyjafjallajökull (Islândia). É imperativo, portanto, desenvolver técnicas de monitoramento através das quais seja possível desenvolver um sistema eficaz para minimizar os perigos causados pelas erupções.

O objetivo deste trabalho consistiu em explorar o uso de imagens de satélite para a observação e quantificação de anomalias termais vulcânicas. As metodologias desenvolvidas para detectar e descrever tal atividade foram projetadas para ser implementadas em um contexto de monitoramento. Desta forma elas podem ser executadas automaticamente por um computador e são globalmente aplicáveis.

Há uma ampla variedade na capacidade dos sensores orbitais devido à relação entre a resolução espacial, a temporal e a espectral. Foi investigado nesse trabalho o uso de diferentes tipos de sensores os quais fornecem, coletivamente, uma alta resolução em cada categoria. Isso é importante porque os fenômenos vulcânicos ocorrem ao longo de escalas temporais e espaciais extensas e cujo comportamento apresenta forte dependência do comprimento de onda. Imagens de alta resolução espacial podem ser utilizadas para restringir o tamanho, forma, localização e orientação de anomalias termais. Dados de alta resolução temporal podem ser usados para monitorar mudanças dinâmicas na atividade térmica e observar eventos efêmeros. A alta resolução espectral permite a melhor caracterização da energia radiante e oferece a possibilidade de realizar análises *subpixel*.

Os dados dos seguintes sistemas de sensores existentes foram utilizados na pesquisa: i) o *Advanced Spaceborne Thermal Emission and Reflection Radiometer* (ASTER), que fornece imagens de alta resolução espacial (30 m) no infravermelho de ondas curtas (SWIR, 1,5 - 3  $\mu\text{m}$ ) e média resolução espacial (90 m) no infravermelho termal (TIR, 8-13  $\mu\text{m}$ ); ii) o *MODerate Resolution Imaging Spectroradiometer* (MODIS), que fornece imagens de alta resolução temporal no SWIR, no infravermelho médio (MIR, 3 - 5  $\mu\text{m}$ ) e no TIR; e iii) o Hyperion, que é um espectrômetro imageador no SWIR. Os dados destes sistemas foram analisados no contexto

da atividade vulcânica, descritos por relatórios de campo, com o objetivo de explorar o seu potencial como precursores de erupções.

O sensor ASTER é capaz de detectar anomalias termais sutis utilizando suas bandas no TIR. Imagens deste sensor foram usadas para quantificar o tamanho e intensidade de anomalias termais durante uma série de tempo decenal em uma gama de vulcões: Erebus (Antártica), Lásçar (Chile), Kīlauea (Havaí), Erta ‘Ale (Etiópia) e Kliuchevskoi (Rússia). Nos vulcões Lásçar e Kliuchevskoi foram identificados precursores termais relacionados à atividade eruptiva. Tais precursores podem formar a base de futuros sistemas automatizados de alerta.

MODIS foi utilizado para caracterizar a atividade do Lásçar, Kīlauea, Erta ‘Ale e Kliuchevskoi. Muitas das imagens ASTER e MODIS foram adquiridas contemporaneamente, uma vez que os dois sensores estão a bordo do mesmo satélite (i.e. Terra). Isto permitiu explorar a sinergia entre os dois sensores. A atividade térmica, detectada pelo MODIS, foi descrita usando uma medida simples de radiância vulcânica. Foram realizadas também análises avançadas de séries temporais utilizando dados MODIS através de *wavelets*. Isso permitiu investigar a periodicidade na série de tempo observada, permitindo assim a quantificação do intervalo durante o qual a radiância aumentava e diminuía e o período de repouso entre os eventos, o que fornece indicações importantes sobre a probabilidade de futuras erupções (Marzocchi e Zaccarelli, 2006) e, portanto, sua quantificação objetiva poder contribuir para os esforços de previsão no futuro.

Para detectar anomalias termais é necessário quantificar o comportamento normal, bem como os desvios anormais. Isso exigiu o desenvolvimento de uma abordagem inovadora para a seleção da temperatura de *background* para os dados ASTER, bem como a definição de limiares de anomalia específicos para o MODIS. Anomalias termais em dados Hyperion foram identificados utilizando um limiar de radiância. Uma vez identificada uma anomalia, é fundamental que as métricas utilizadas para descrever a atividade vulcânica térmica sejam viáveis. Ao longo dos últimos 30 anos, uma grande quantidade de atenção tem sido dada à análise *subpixel* de imagens de alvos vulcânicos. Isto ocorre devido às superfícies vulcânicas ativas serem, com frequência, termicamente heterogêneas em relação à escala espacial de um pixel. Isso quer dizer que um único valor de temperatura ou radiância não descreveria toda a complexidade térmica de superfícies com atividades vulcânicas.

Neste estudo foi explorada a capacidade de espectrômetros imageadores, tais como Hyperion, para resolver características *subpixel* (i.e. o número, tamanho e temperatura das

componentes isotérmicas menores de um pixel). Tal objetivo foi atingido através do desenvolvimento de um método para a modelagem inversa do espectro de radiação, a partir do qual as características *subpixel* podem ser derivadas. Este método foi testado utilizando testes do tipo Monte Carlo que mostrou a precisão da metodologia desenvolvida (erros entre 3 e 5%). Todavia, mesmo neste nível de precisão, não foi possível resolver de forma confiável as características *subpixel*. Teoricamente a precisão do modelo, se aprimorada, poderia aumentar a confiabilidade nas soluções *subpixel*. Na prática, porém, isto não é possível devido às limitações na precisão de medida dos espectros de radiação. Assim, é improvável que se possa, de forma confiável, determinar características *subpixel* de imagens de vulcões ativos por meio de informação espectral. Tal fato tem implicações profundas, dada a extensão em que os autores anteriores tentaram resolver estes parâmetros durante as últimas três décadas.

Sendo assim, definimos uma solução alternativa. Fluxo radiante e excitância são duas métricas (relacionadas) que podem ser utilizadas para descrever, de forma confiável e significativa, a atividade térmica mesmo de superfícies com altos gradientes de temperatura. Por meio destes dados, desenvolvemos um método para calcular estes parâmetros que é computacionalmente eficiente e, portanto, rápido o suficiente para ser executado por computadores à bordo dos sistemas de sensores para processamento em rota. Nós fornecemos um exemplo prático desta abordagem utilizando dados do Hyperion de um fluxo de lava no vulcão Kliuchevskoi.

Esta tese está organizada da seguinte forma. Uma revisão fundamental de princípios científicos e do estado da arte é fornecida no Capítulo 2. Este é seguido por capítulos que são compostos de artigos que foram publicados, aceitos ou prestes a serem submetidos em revistas internacionais. O Capítulo 3 explora a utilização do ASTER para caracterizar o tamanho e intensidade das anomalias térmicas nos vulcões Lásçar e Erebus. O Capítulo 4 investiga o desenvolvimento de uma sinergia entre ASTER e MODIS, bem como a demonstração da utilização da análise de *wavelet* em dados MODIS. O Capítulo 5 explora o uso de espectrômetros para calcular fluxo radiante. E o Capítulo 6 considera o futuro do sensoriamento remoto de vulcões e fornece uma conclusão geral.



# Chapter 1

## Introduction

---

The Earth is a dynamic physical system. The thermodynamic disequilibrium between the hotter terrestrial interior and the colder terrestrial crust leads towards a net transfer of heat energy in the direction of the cold space through which the planet traverses. This transfer of heat energy on a planetary scale manifests itself most clearly in the form of volcanoes. Given the magnitude of this process volcanoes play a number of influential roles within the Earth system and are integral towards our understanding of how the planet works.

Throughout geological history volcanic activity has had dramatic effects on the composition of the atmosphere, the climate of the Earth, the extinction of species and the concentration of minerals into what have now become ore bodies. Volcanic deposits also offer valuable insights into the dynamics and composition of the Earth through time; including our only samples of the mantle. Clearly, however, contemporary volcanic activity also poses a number of hazards to society including loss of human life and severe impacts on economy and infrastructure.

Volcanic time scales often appear long compared to human time scales, furthermore volcanoes are dispersed around the globe, consequently most active volcanoes have no dedicated monitoring program. Yet, at any one time, there are some 20 eruptions occurring simultaneously and there are typically around 60 eruptions per year. This perilous monitoring gap will inevitably

result in the avoidable loss of life and material property. Spaceborne sensors provide the only means at present for filling this gap on a global scale.

Volcanic hazard is a global issue that directly or indirectly affects a large proportion of the world's population. From a South American perspective the majority of the West coast of this continent is volcanically active, principally due to subduction of the Nazca Plate below the South American Plate. This has implications for the entire continent given the truly enormous areas that can be affected by volcanic ash plumes. The 1993 eruption of Láscaar (Chile) caused tephra (i.e. volcanic ash) fall-out over Porto Alegre (Brazil) some 1800 km away. More recently (i.e. June 2011) activity at Puyehue volcano (Chile) formed an ash plume that traversed from Chile through Argentina into the Atlantic Ocean (Fig. 1.1).

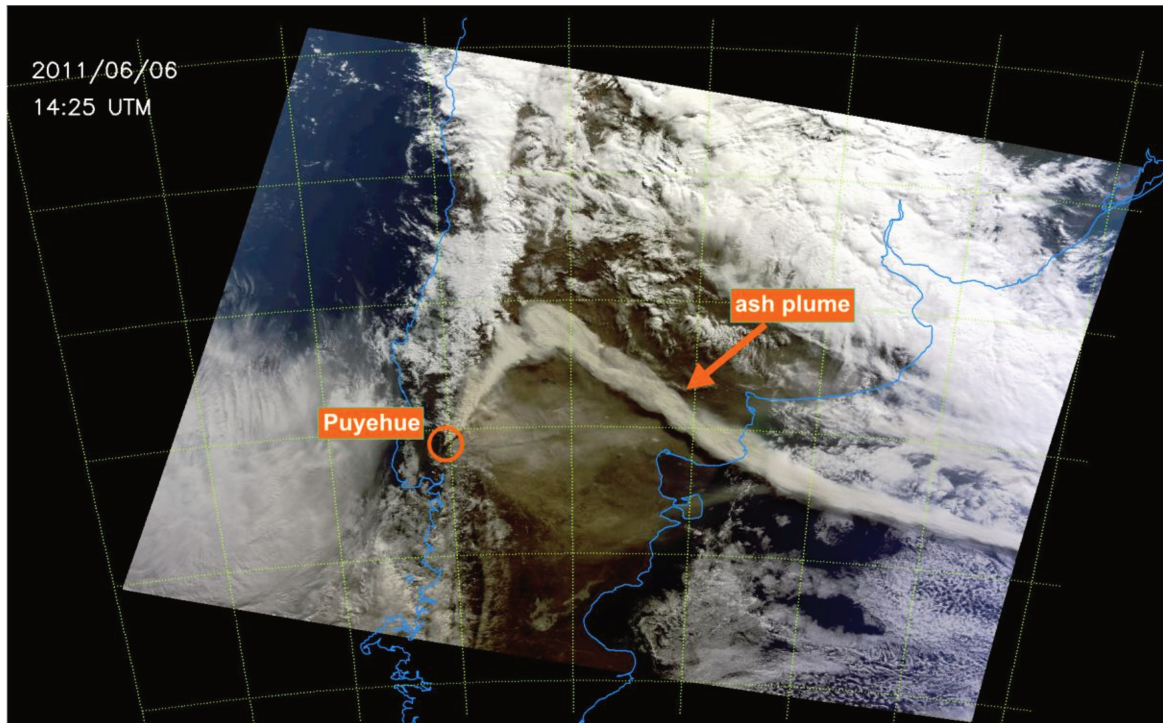


**Figure 1.1.** A MODIS true colour image of the Puyehue (Chile) eruption in June 2011. The ash plume is seen travelling NNE before sweeping ESE across Argentina. Flights were cancelled at Argentinean, Brazilian and other South-American airports.

Flights, including those to be boarded by Brazilian passengers, were cancelled to and from Buenos Aires International Airport (i.e. situated some 1400 km away from the volcano). Disruptions such as these are likely to occur more frequently in the future due to the ever

increasing density of air-traffic in the region. The consequences of such disruptions can include potentially enormous financial loss through adverse affects on business and trade, as recently occurred after European airspace was closed for a few days in March 2010 following the eruption of Eyjafjallajökull (Iceland). It is therefore imperative to develop monitoring techniques upon which effective hazard mitigation strategy can be based.

The aim of this thesis is to explore the use of infrared imagery from satellite sensors for the observation and quantification of volcanic thermal anomalies. The methodologies developed to detect and describe such activity have been designed for implementation in a monitoring context; thus they can be executed automatically by a computer and are globally applicable. This thesis therefore works towards improving the global volcano monitoring system.

Orbital sensors have a wide variety of capabilities that are borne out of a trade-off between spatial, temporal and spectral resolution. Image data from a single sensor system might therefore have a high resolution in up to two of these categories; but not all three. This is primarily due to limitations in existing imaging technology and data transfer rates. I investigated the use of different sensor types that collectively provide high resolution in each category. This is of importance because volcanic phenomena occur over wide temporal and spatial scales and exhibit strong wavelength dependent behaviour. High spatial resolution images can be used to constrain the size, shape, location and orientation of thermal anomalies. High temporal resolution data can be used to monitor dynamic changes in thermal activity as well as to observe ephemeral events, and high spectral resolution allows radiant energy to be better characterized, and offers the possibility to carry out advanced subpixel analysis.

Data from the following existing sensor systems were utilised in this research: i) the Advanced Spaceborne Thermal Emission and Reflection Radiometer (ASTER), which provided high spatial resolution imagery in the Short-Wave InfraRed (i.e. SWIR, 1.5 - 3  $\mu\text{m}$ ) and moderate spatial resolution imagery in the Thermal InfraRed (i.e. TIR, 8 - 13  $\mu\text{m}$ ); ii) the MODerate Resolution Imaging Spectroradiometer (MODIS), which provided high temporal resolution imagery in the SWIR, mid wave infrared (i.e. MIR, 3 - 5  $\mu\text{m}$ ) and TIR; and iii) Hyperion which is a SWIR imaging spectrometer. The data from these separate sensor systems were analyzed in the context of volcanic activity, as described by field reports, and with the aim of exploring their potential as eruptive precursors.

The ASTER sensor was capable of detecting subtle thermal anomalies using its TIR bands. Images from this sensor were used to quantify the size and intensity of thermal anomalies over a decadal time series at a range of volcanoes, namely: Erebus (Antarctica), Láscar (Chile), Kīlauea (Hawai'i), Erta 'Ale (Ethiopia) and Kliuchevskoi (Russia). Thermal precursors to eruptive activity were identified at Láscar and Kliuchevskoi, such precursors might form the basis of future automated alert systems.

MODIS was used to characterize activity at Láscar, Kīlauea, Erta 'Ale and Kliuchevskoi. Many of the ASTER and MODIS images were acquired contemporaneously as both sensors are on board the same satellite (i.e. Terra). This allowed a synergy between the two sensors to be explored. Thermal activity, as seen by MODIS, was described using a straightforward metric of volcanic radiance. Advanced time series analysis was carried out on the MODIS data sets through the use of wavelets. This allowed periodicity in the time series to be investigated, allowing the quantification of the period over which thermal activity waxed and waned, as well as the length of repose between events, to be defined. Waxing, waning and repose provide important indications on the probability of future eruptions (Marzocchi and Zaccarelli, 2006) and therefore their objective quantification may contribute to forecasting efforts in the future.

In order to detect thermal anomalies it is necessary to be able to quantify normal behaviour as well as abnormal deviations from it. This required that we develop an innovative approach to background temperature selection for ASTER data as well as to define volcano specific anomaly thresholds for MODIS. Anomalies in Hyperion data were defined using a simple radiance threshold. Once an anomaly has been identified it is critical that the metrics used to describe volcanic thermal activity are both reliable and meaningful. Over the last 30 years a great deal of attention has been paid to the subpixel analysis of imagery from volcanic targets. This is because active volcanic surfaces are often thermally heterogeneous at the pixel scale. A single radiance or temperature value will therefore not capture the full thermal complexity of active volcanic surfaces.

I explored the ability of imaging spectrometers, such as Hyperion, to resolve subpixel characteristics (i.e. the number, size and temperature of isothermal subpixel components) at volcanic targets. This was achieved by developing a method for inverse modelling of radiance spectra from which subpixel characteristics could be derived. This method was tested using a Monte Carlo approach. Radiance spectra could be accurately modelled, i.e. to within 3 - 5 %.

However, even at this level of accuracy, it was not possible to reliably resolve subpixel characteristics. Theoretically improved model fitting accuracy could allow for more reliable subpixel characteristics solutions. However, in practice, this is probably not possible due to limitations in the accuracy to which radiance spectra can be measured in the first place. Thus, it is improbable that we can reliably determine subpixel characteristics of imagery from active volcanoes using spectral information alone. This has profound implications given the extent to which previous authors have attempted to resolve such parameters over the last three decades.

We advocate an alternative solution. Radiant flux and radiant exitance are two (related) metrics that can both be used to reliably and meaningfully describe thermal activity even from surfaces with strong temperature gradients. We developed a method for calculating these parameters that is computationally efficient, and therefore fast, enough to be executed by computers on-board sensor systems for on-the-fly processing. We provide a practical example of this approach using data from Hyperion, producing maps of radiant flux of an active lava flow at Kliuchevskoi volcano.

This thesis is organized in the following way. A fundamental review of scientific principals and context is provided in Chapter 2. This is followed by chapters that are comprised of articles that have been either published in, accepted by or about to be submitted to international, peer-reviewed journals. Chapter 3 explores the use of ASTER to characterize the size and intensity of thermal anomalies at Láscaar and Erebus, Chapter 4 investigates the development of a synergy between ASTER and MODIS as well as demonstrating a use of wavelet analysis on MODIS data, Chapter 5 explores the use of imaging spectrometers to calculate radiant flux and makes the case against subpixel analysis at volcanic targets. Chapter 6 looks to the future of infrared remote sensing of volcanoes from space and provides an overall conclusion.



# Chapter 2

## Scientific Context

---

### **2.1. Observing Volcanoes from Space**

Satellites provide many advantages over field-based techniques when observing volcanic behaviour. These include: global coverage, a synoptic perspective of a scene, continuity of data collection, almost zero exposure of people and equipment to volcanic hazards, and typically a much lower cost of data acquisition for the end user.

There are two principal orbits used by Earth observation satellites (Fig. 2.1); those that traverse around the Earth's poles (i.e. polar orbit) and those that stay within the plane of the Earth's equator whilst completing an orbit in a 24 hour period thus point continuously towards the same face of the Earth (i.e. geostationary).

Polar orbits have relatively low altitudes ( $< 1000$  km) and are sun-synchronous (i.e. they pass the equator at the same time of day and night). Within the typical altitude range of a polar orbiting satellite (i.e. 550 - 850 km) the orbit period will take  $99 \pm 4$  minutes. This translates into about 14.5 orbits per day. Polar orbiters are able to provide global coverage because of the rotation of the Earth.

Geostationary satellites, on the other hand, are situated at much high altitude (i.e. 35,770 km) in order to obtain the required 24 hour orbit period. Clearly a single geostationary satellite cannot image the Earth's entire surface. However a constellation of at least 5 satellites, separated by  $60^\circ$  of longitude, could provide global coverage of equatorial regions (Mouginis-Mark and Domergue-Schmidt 2000). Even so such a geostationary constellation will inevitable suffer severe distortion beyond  $\sim 50^\circ$  from the sub satellite point due to the curvature of the Earth and will also be incapable of imaging the poles.

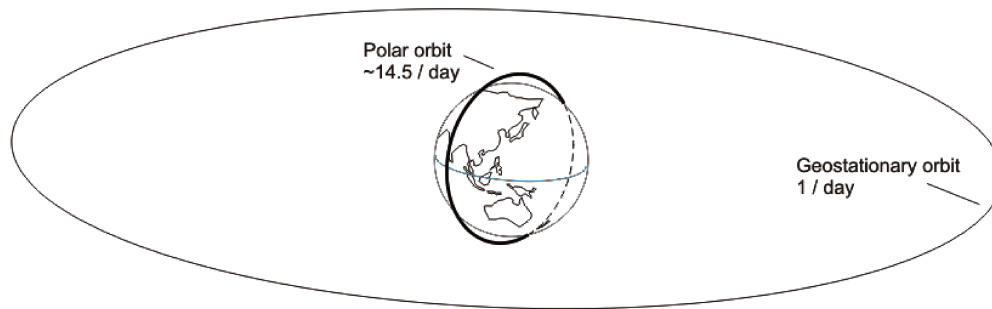


**Figure 2.1. A schematic of polar and geostationary orbits.**

An imaging sensor contains an array of detector elements; this is often referred to as a ‘focal plane array’. The response from each detector element will typically correspond to a single picture element (i.e. pixel) within an image. The angular cone of visibility of each detector element is known as its instantaneous field of view (i.e. IFOV). The area on the Earth's surface to which a single pixel corresponds is proportional to the IFOV of the detector element and the altitude of the satellite. This area is typically assumed to be well represented by discrete, non-overlapping rectangles, as this greatly facilitates computational processing and visualization of image data. The size of the rectangular area on the ground to which a single pixel corresponds is the standard way of expressing spatial resolution. The smaller the pixel size the higher the spatial resolution. In reality the IFOVs of detector elements are not rectangular and they do overlap. This can present issues when imaging hot targets with strong thermal gradients (e.g. Chapter 5). The geographical width of the area imaged by an entire focal plane array is known as the swath width. This width, as well as the orbital period of a satellite, controls the temporal frequency of polar orbiters (i.e. the time taken to acquire consecutive images of the same part of the Earth's surface).

Conversely, the temporal frequency of geostationary satellites is controlled solely by their data acquisition and transfer rate, typically providing a new image of the same portion of the Earth every 15 - 30 minutes.

Satellite sensors are often classified based on their spatial and temporal resolution. At the time of writing images with pixel sizes smaller than somewhere between 30 to 100 m are usually considered to be of high spatial resolution. Revisit periods of less than one day are considered to be high temporal resolution. Images with a pixel size of around 1 km or more are considered to be of low spatial resolution. Revisit periods of more than a couple of weeks constitute a low temporal resolution. Spectral capabilities are usually classified depending on whether a sensor system has a single, typically quite wide, waveband (panchromatic), more than one waveband (multispectral), or more than one hundred wavebands, in this case often referred to as 'channels' (hyperspectral). There exists the possibility that hyperspectral sensors will become known as imaging spectrometers. The wide variety of spatial, temporal and spectral information captured by current and past orbital sensors has been creatively adopted by the volcano monitoring community over the years. The predominant themes are discussed below.

### 2.1.1. Thermal Emission

It is possible to monitor the central driving force of volcanic activity (i.e. heat transfer) directly from space by measuring radiated electromagnetic energy. The first recorded observation of thermal volcanic activity from space was from the High Resolution Infrared Radiometer (HRIS) on board the Nimbus 1 (Gawarecki et al. 1965). Since then there have been a number of satellites used to observe thermal emissions from volcanoes (Table 2.1).

Nimbus 1 was a geostationary satellite; the HRIR sensor acquired imagery using 70mm film strips that were digitized for transmission back to Earth, using a facsimile scanner (i.e. an apparatus that determines changes in tone density). Focal plane arrays have now superseded facsimile imagers. Modern geostationary satellites include those in NASA's Geostationary Operational Environmental Satellite (GOES) series. The imager on GOES-8 (i.e. launched in 1994) was the first in this satellite series to have a mid infrared (i.e. MIR; 3 - 5  $\mu\text{m}$ ) channel. MIR wavelengths are crucial for detecting thermal anomalies at such a low spatial resolution (i.e. 4 km). Co-registered thermal infrared (i.e. TIR; 8 - 12  $\mu\text{m}$ ) imagery is often used to improve

detection capability as, given that they are insensitive to volcanic thermal phenomenon at such spatial resolutions, they can provide an indication of background conditions (e.g. Harris et al. 1997). The GOES series is principally intended to provide meteorological data. The demand for reliable up-to-date weather forecasts has resulted in the construction and launch of an ever evolving constellation of meteorological satellites. ESA's Meteosat Second Generation (MSG) series, which cover Europe and Africa, have included the Spinning Enhanced Visible and Infrared Imager (SEVIRI) since 2002. SEVIRI has a 4 and 11  $\mu\text{m}$  channel with a temporal resolution of 15 minutes and a pixel size of 3 km. The Japanese Meteorological Agency (JMA) launched the first of the Multi-Functional Transport Satellite series (MTSAT) in 2005. It provides coverage of Asia and Australasia and has 3.7 and 10.8  $\mu\text{m}$  channel with a 4 km spatial resolution. Global equatorial geostationary coverage is therefore a reality and appears likely to remain so for the foreseeable future.

**Table 2.1. Orbital sensors used for infrared observations of volcanoes**

Sensor name	Acronym	Platform	Date of first launch	Spatial Res. (m)	Temporal Res. (days)
High resolution infrared radiometer	HRIR	Nimbus	1964	8000	0.34
Thematic mapper	TM	Landsat 4/5	1972	30 - 120	16
Enhanced thematic mapper plus	ETM+	Landsat 7	1999	15 - 60	16
Advanced very high resolution radiometer	AVHRR	NOAA	1978	1100	1
Along-track scanning radiometer	ATSR	ERS	1991	1000	3
JERS optical sensor	OPS	JERS	1992	18 - 24	44
GOES imager	Imager	GOES	1994	4000	15 - 30 <b>mins</b>
Advanced spaceborne thermal emission and reflection radiometer	ASTER	Terra	1999	15 - 90	16
Moderate resolution imaging spectroradiometer	MODIS	Terra/Aqua	1999	250 - 1000	1
Advanced land imager	ALI	EO - 1	2000	30	42
Hyperion	Hyperion	EO - 1	2000	30	200
MTSAT imager	Imager	MTSAT	2005	4000	30 <b>mins</b>
Spinning enhanced visible and infrared imager	SEVIRI	Meteosat	2005	3000	15 <b>mins</b>
Visible infrared imager radiometer suite	VIIRS	NPPS	2011	375 - 750	0.5

For truly global coverage it is necessary to use polar orbiting satellites. Large swath width polar orbiters (i.e.  $\sim 3000$  km) are capable of acquiring daily images at equatorial latitudes and even more frequently towards the poles due to orbit convergence. High temporal resolution polar orbiters typically have pixel sizes of around 1 km. The Advanced Very-High Resolution Radiometer (AVHRR) was the first to measure in the MIR and also freely transmits data to

anyone with a receiving station. The Alaska Volcano Observatory (AVO) has been using AVHRR to monitor volcanoes at the Alaskan peninsula, the Aleutian Islands and the Kamchatkan peninsula since 1994. This has included the development of algorithms that automatically detect thermal anomalies and produce up-to-date visual representations of target volcanoes (e.g. Dean et al. 1996). The Along Track Scanning Radiometer (ATSR), launched on board the second European Remote Sensing Satellite (ERS - 2) in 1995 and de-orbited in June 2011, provided similar data to that of AVHRR but with an additional 1.6  $\mu\text{m}$  channel to further constrain spectral radiance from hot, spatially extensive targets. It was not until the launch of the Moderate Resolution Imaging Spectroradiometer (MODIS) however, i.e. in December 1999, that a truly global volcano thermal monitoring system could be developed. The first, and currently only, of which was MODVOLC. This monitoring system automatically scans MODIS data for hotspots and, when found, records their location, time and radiant intensity. NASA Goddard Space Flight Center sends these algorithm outputs to the University of Hawaii every 5 minutes which, in turn, are made available on the MODVOLC website ([modis.higp.hawaii.edu](http://modis.higp.hawaii.edu)). The most recent addition to the fleet of high temporal resolution polar orbiters is the Suomi NPP<sup>1</sup>. It was successfully launched on 28 October 2011. The sensor on board Suomi NPP which can be used to monitor volcanic thermal activity is the Visible Infrared Imager Radiometer Suite (VIIRS). It provides high temporal resolution (0.5 day revisit) imagery at a pixel size of 375 - 750 m.

High spatial resolution data are available from polar orbit given their proximity to the Earth. Thermal observations of volcanoes at high spatial resolution first became available with the launch of the Landsat 4 and 5 (launched in 1982 and 1984, respectively) which contained the Thematic Mapper (TM) sensor. Landsat 7, launched in 1999, also provided data from the Enhanced Thematic Mapper Plus (ETM+). These sensors each provided two SWIR channels at 30 m pixel resolution and a coarse TIR channel (i.e. 120 m/pixel for the TM and 60 m/pixel for

---

<sup>1</sup> The Suomi NPP mission was originally called just 'NPP' (i.e. NPOESS Preparatory Project), where 'NPOESS' was the National Polar-orbiting Operational Environmental Satellite System. The NPOESS program was dissolved on 1 February 2010 into separate civilian and military components. The civilian component is now under the jurisdiction of the National Oceanic and Atmospheric Administration (NOAA) and has been renamed the Joint Polar Satellite System (JPSS). The acronym NPP has been changed accordingly; it now signifies 'National Polar-orbiting Partnership'.

the ETM+). The Landsat series have been used to investigate several volcanic phenomena, including: lava flows, lava lakes, volcanic domes, fumarole fields, Strombolian vents, and warm crater lakes (e.g. Flynn et al. 2000). The launch of the ASTER sensor on the Terra satellite in December 1999 (i.e. the same satellite that carried the first MODIS sensor) provided an unprecedented number of high spatial resolution channels, with 6 in the SWIR and 5 in the TIR. Particular focus has been paid to utilizing the TIR bands to obtain surface temperature estimates, e.g. Ramsey & Dehn (2004), Pieri & Abrams (2005), Vaughan & Hook (2006), Vaughan et. al. (2008), and Carter and Ramsey (2009), but also to explore the potential for subpixel analysis (Vaughan et al. 2010).

Earth Observing 1 (i.e. EO-1) was also launched around the turn of the millennium (i.e. November 2000). It contained Hyperion, the first ever orbital imaging spectrometer. The extra spectral resolution allowed more advanced subpixel analysis to be carried out (section 2.5.). The use of high spatial (i.e. ASTER), high temporal (i.e. MODIS) and high spectral (i.e. Hyperion) resolution satellites for monitoring thermal activity from volcanoes is the main thrust of this thesis and is discussed in more detail in the following chapters.

### 2.1.2. Gas Plumes

The primary mechanism by which heat energy is transferred to the Earth's surface from volcanic systems is through the movement of volatiles (i.e. predominantly water as well as some CO<sub>2</sub>). Measuring water and CO<sub>2</sub> fluxes from space is not trivial, largely because of their high concentration in the atmosphere. Potential breakthroughs in CO<sub>2</sub> detection may arise from use of the Japanese Greenhouse gases Observing Satellite (GOSAT) or the planned second Orbiting Carbon Observer mission (OCO-2). In contrast SO<sub>2</sub> has a low atmospheric concentration which makes it relatively simple to detect using diagnostic absorption features in the UV (~0.3 μm), TIR (~8.6 μm) and even microwave (~1469 μm) wavelengths. Observation of SO<sub>2</sub> plumes from space using UV wavelengths has been ongoing since Krueger (1983) first discovered anomalies in ozone retrievals following the eruption of El Chichón (Mexico). The Total Ozone Mapping Spectrometer (TOMS) was used in initial studies; other sensors with a pertinent UV channel for SO<sub>2</sub> observation and/or quantification include the: Global Ozone Monitoring Experiment (GOME), GOME-2, SCanning Imaging Absorption spectroMeter for Atmospheric

CHartographY (SCIAMACHY), Ozone Monitoring Instrument (OMI) and Ozone Mapping and Profiler Suite (OMPS) (e.g. Hooper et al. 2012). The use of the TIR absorption feature to obtain SO<sub>2</sub> retrievals began with the High Resolution Infrared Sounder (HRIS) (Prata et al. 2003) and was followed by uses of ASTER, MODIS, AIRS and IASI for this purpose (Prata et al. 2012). Measurements of volcanic SO<sub>2</sub> from space using microwave wavelengths have been demonstrated by Read et al. (1993) using data from the Microwave Limb Sounder (MLS). However the extremely low spatial resolution of this sensor (~ 30-150 km) limit its practical applicability.

### 2.1.3. Ash Clouds

Explosive eruptions can produce large quantities of fragmented pyroclastic material. Hot ash-rich eruption clouds can often reach heights of 10 km or more and spread out laterally for thousands of kilometres. Satellites provide the only means of directly observing the entirety of such extensive features. Ash related hazards include respiratory problems, roof collapse and a potential for ash deposits to remobilize as lahars (i.e. volcanic mudflows). Unfortunately societal vulnerability to volcanic ash is increasing due to the growing number of people and cargo that are transported by air. This is because modern jet engines operate at temperatures that melt silicate-rich minerals, this can cause engine failure by the melting and solidification of ash within the turbine. The eruptions of Galunggung, Java (June 1982); Redoubt, USA (December 1989) and Pinatubo, Philippines (June 1991) all resulted in severe damage to passenger jets with repair costs running into the millions of US dollars (Miller & Casadevall 2000). Fortunately no lives were lost even though aircraft plummeted by as much as 7500 m in 16 minutes after ingesting ash and subsequently stalling (Miller & Casadevall 2000). These instances provided a strong motivation for the identification and quantification of volcanic ash plumes using satellites. Prata (1989) showed that a 10 and 12  $\mu\text{m}$  channel could be used to differentiate between ash clouds and water/ice based on their brightness temperature difference. Examples of volcanic ash retrievals include uses of MODIS (Watson et al. 2004), AIRS (Hooper et al. 2012) and SEVIRI (Prata & Prata 2012) sensors.

#### 2.1.4. Geometry

The geometry of a volcano is an extremely important control on the direction and distance travelled by a hazardous flow (e.g. pyroclastic flow, lava flow, debris avalanche or lahar). Digital elevation models (DEM) therefore form the basis for hazardous flow models (e.g. TITAN 2D, Pitman et al. 2003). The Shuttle Radar Topography Mission (SRTM), carried out during February of 2000, provided a DEM at spatial resolution of 30 m for all terrestrial surfaces between 56° S and 60° N. As of June 2009 a global DEM, created using ASTER's stereoscopic viewing capability, was released to the public (i.e. ASTER GDEM). It also offers 30 m spatial resolution.

Volcanic edifices can expand and contract in response to pressure variations from the flux of magma and volatiles in a volcanic system. Centimetre scale changes in the geometry of a volcanic edifice can be imaged from space using synthetic aperture radar interferometry (InSAR). The principle behind InSAR is that phase changes in two separate synthetic aperture radar (SAR) images, taken of the same location but at different times, provides information on the change in distance between the satellite and the target surface. It is assumed that the scattering properties of the ground remain fairly constant between acquisitions, thus variable snow and ice cover and/or dense vegetation can be problematic. Even so, many studies have been successfully carried out to show quantitative observations of topographic changes that have been attributed to, for example, magma chamber dynamics (e.g. Lu et al. 2000, Fialko & Simons 2001, Pritchard & Simons 2002, Wicks et al. 2006), sill and dike intrusion (e.g. Jónsson et al. 1999, Fukushima et al. 2005, Pedersen & Sigmundsson 2006) and faulting (Amelung et al. 2000). Currently the TerraSAR-X and COSMO-SkyMed satellite constellations provide 11 and 4 day temporal resolution respectively. ESA's Sentinel-1 satellites (i.e. launch in 2013 and 2014) will further increase the frequency at which terrestrial SAR images are acquired.

### 2.1.5. Mapping eruptive products

High spatial resolution polar orbiters with infrared wavebands can be used to map thermally anomalous surfaces. Landsat 4 and 5 have been used to map the distribution of cooling lava flows (e.g. Flynn et al. 1994) and locate the surface expression of active underground lava tubes (e.g. Harris et al. 1998). The TIR bands of the ASTER sensor facilitated the detection of more subtle thermal anomalies from pyroclastic flows and lava domes (e.g. Carter & Ramsey 2009).

## 2.2. Physical Principles

Energy is an abstract quantity which seems to be constant during all physical interactions. This characteristic has resulted in it becoming a fundamental concept in our understanding of the observable universe. Energy is required to make, move and change matter. All matter with a temperature above absolute zero will radiate electromagnetic energy. This radiant energy displays a wave-particle duality and is therefore modelled as both electromagnetic waves and physical particles (i.e. photons). The energy associated with a single photon can be expressed as:

$$q = \frac{hc}{\lambda} \quad (2.1)$$

where  $h$  is Planck's constant ( $6.626 \times 10^{-34}$  J s),  $c$  is the speed of light in a vacuum ( $2.998 \times 10^8$  m s<sup>-1</sup>) and  $\lambda$  is the photon wavelength in metres. The SI unit of energy is Joules. We are usually concerned with multiple photons. The total energy ( $Q$ ) from a wave train or burst of radiant energy is the sum of all photon energies ( $q_i$ ) in that burst

$$Q = \int_{i=1}^n q_i \quad (2.2)$$

The rate of photon energy transfer is known as the radiant flux ( $\Phi$ )

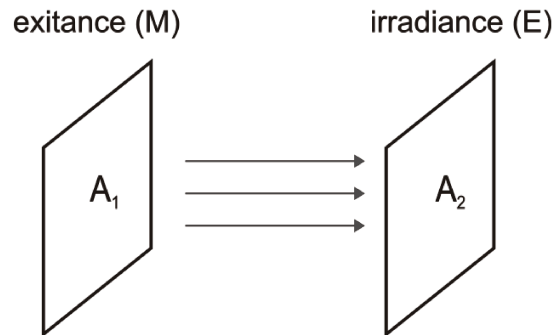
$$\Phi = dQ/dt \quad (2.3)$$

It is often necessary to quantify the radiant flux per unit area of a plane surface. This quantity is known as exitance (M) when considering photons that are leaving a given area or as irradiance (E) when they are incident upon an area.

$$M = dQ/dt/dA \quad (2.4)$$

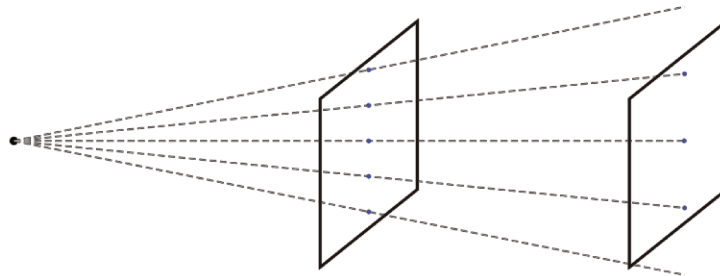
$$E = dQ/dt/dA \quad (2.5)$$

Figure 2.2 depicts a parallel wave train of photons leaving an area (A1) and moving towards another area (A2) some distance away. The radiant flux leaving area A1 is an example of exitance, the radiant flux incident upon A2 is an example of irradiance.



**Figure 2.2. Examples of exitance (M) and irradiance (E). The grey arrows depict the direction of radiant flux (i.e. photons per second).**

Figure 2.3 displays the case in which photons propagate from a point source and then transect area A1 followed by A2. The irradiance will be greater on A1 than on A2 because the photon trajectories are divergent.



**Figure 2.3. Irradiance (i.e. radiant flux per unit area) will diminish with distance from a point source due to divergence of photon trajectories.**

The decrease in irradiance from a point source is proportional to the inverse of the squared distance from that source.

$$M \propto \frac{1}{r^2} \quad (2.6)$$

A metric that is dependent on distance would be inconvenient for many applications (e.g. comparing field and spaceborne measurements). The concept of a solid angle is used to address this problem. The SI unit of a solid angle is steradians ( $\Omega$ ).

$$\Omega = \frac{A}{r^2} \quad (2.7)$$

where  $A$  is an area on the surface of a sphere subtended by an arc, and  $r$  is the radius of the sphere. A solid angle is therefore dimensionless, i.e. (equation 2.7), and can encapsulate a range of geometries from an infinitesimally narrow beam up to a sphere (Fig. 2.4).

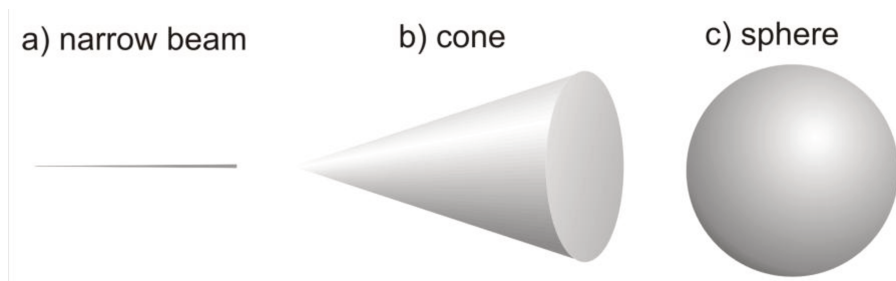


**Figure 2.4. Examples of solid cone geometries**

The radiant flux per unit steradian is called radiant intensity.

$$I = dQ/dt/d\Omega \quad (2.8)$$

Radiant intensity will not change with distance from the source (i.e. assuming that the photons are not absorbed, scattered or refracted by the medium through which they are propagating). This is because the divergence of photons matches the increase in the cross-sectional area of the solid

angle through which they are propagating (i.e. both increase as a function of distance squared from the source).

A steradian begins at single point in space. It is therefore necessary for the source area to approximate a point relative to the geometry of the solid angle through which the photons propagate. Essentially it requires there to be negligible difference between i) the radiant intensity in the hypothetical case where all photons are emitted from the centre of the source area and ii) radiant intensity in the actual case where photons are being emitted throughout the source area. This is what is meant by a point source.

However, although we can assume for mathematical convenience that photon trajectories start from the centre of the source area, the size of the source area itself is still an important control on the number of photons propagating into any given solid angle. If photons leave the surface at a uniform rate then the radiant intensity is directly proportional to the size of the source area (A).

$$I \propto A \quad (2.9)$$

Radiant intensity is also dependent on the orientation in which the photons are propagating. If exitance from the source area is isotropic (i.e. has no directional preference) then this relationship is defined by Lambert's Cosine Rule (10)

$$I_{\theta} = I_0 \cos\theta \quad (2.10)$$

where  $I_{\theta}$  is the intensity at angle  $\theta$  from the normal and  $I_0$  is intensity at the normal. A surface that follows this law is known as a Lambertian surface. Radiant intensity from a Lambertian surface is therefore greatest at normal (i.e. perpendicular to the surface) and diminishes as  $\theta$  approaches  $90^{\circ}$ . One way of conceptualizing why this occurs is by imagining the projection of the source area into the direction of the solid angle (Fig. 2.5).

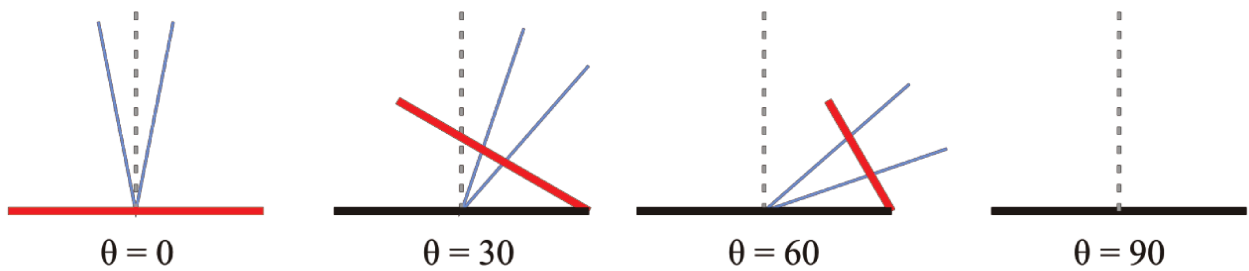


**Figure 2.5. The projected source area (red) will decrease in size as the orientation of the solid angle (blue) moves away from the normal ( $\theta$ ).**

This projected source area (red line) represents the smallest area through which all photons must pass. Note that photons are in fact emitted from the entire source area, even though they are mathematically treated as propagating from a point source through a solid angle (blue cone). If photons are radiating equally in all directions then, as the projected area becomes smaller (i.e. as  $\theta$  increases), the number of photons entering the corresponding solid angle will also diminish. Radiant intensity is therefore directly proportional to the cosine of the orientation of the solid angle from the normal.

$$I \propto \cos\theta \quad (2.11)$$

However, the brightness of a Lambertian surface will not change with viewing angle. This is because radiant intensity will diminish at the same rate as the perceived size of the area. In other words, the surface will appear smaller as viewing angle from the normal (i.e.  $\theta$ ) increases, and the radiant intensity will also decrease as  $\theta$  increase, and both of these changes occur at the same rate (i.e. proportional to  $\cos\theta$ ).

Therefore, if we divide radiant intensity by  $A\cos\theta$ , we will create a measure of photon propagation through time and space that is not dependent on the distance, or orientation, of the viewer from the source nor the size of the source area, as long as the point source assumption remains valid. This quantity is known simply as radiance.

$$L = dQ/dt/d\Omega/dA\cos\theta \quad (2.12)$$

The interaction between real surfaces and electromagnetic radiation is wavelength dependent. Modern imagers are therefore designed to be sensitive to specific parts of the spectrum. Radiance measured with respect to wavelength is called spectral radiance ( $L_\lambda$ ).

$$L = dQ/dt/d\Omega/dA\cos\theta/d\lambda \quad (2.13)$$

Spectral radiance is the fundamental metric used in the field of electromagnetic remote sensing. It is often necessary to work back from spectral radiance measurements to calculate the amount of energy being emitted or reflected from a given source area. This might be the rate of radiant energy transfer (i.e. radiant flux [W]) or the rate of radiant energy transfer per unit area (i.e. exitance [ $\text{W}/\text{m}^2$ ]). The relationship between exitance (2.4) and radiance (2.13) can be expressed as follows:

$$M = \int L\cos\theta d\Omega \quad (2.14)$$

The collection of all possible photon trajectories from a flat surface will define a hemisphere above that surface (Fig. 2.6). The integral in (2.14) must therefore be evaluated over such a geometry.

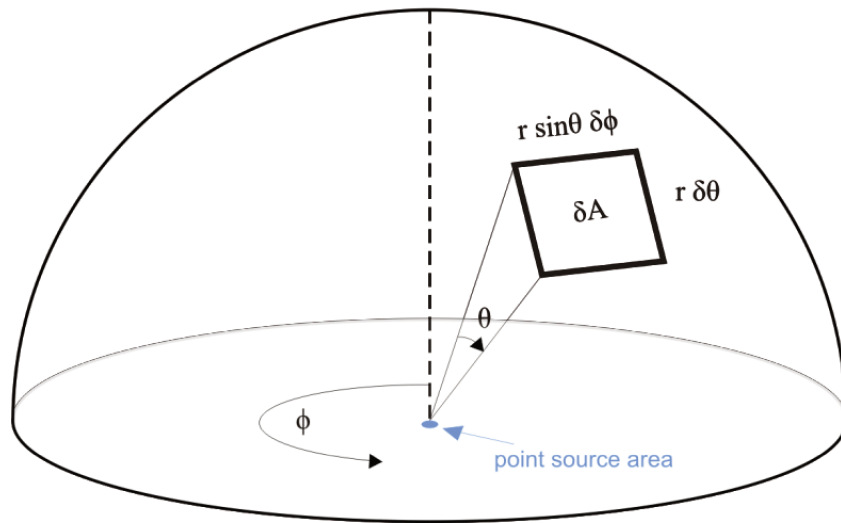


**Figure 2.6. The geometry of an infinitesimal area on the surface of a hemisphere**

It is possible to define a curved surface using infinitesimally small planar surfaces (i.e. in much the same way that infinitesimally small straight lines can be used to define a curved line). If  $\theta$  is the angle from the normal to the surface and  $\phi$  is the azimuth, then  $\delta\theta$  and  $\delta\phi$  signify infinitesimally narrow components of these angles, and  $\delta A$  is an infinitesimally small area (Fig. 2.6). This area defines an infinitesimally small solid angle. The size of  $\delta A$  can be calculated using trigonometry

$$\delta A = r^2 \delta\theta \sin\theta \delta\phi \quad (2.15)$$

We can therefore express solid angles in terms of actual angles, i.e. substituting (2.15) into (2.7)

$$d\Omega = \frac{r^2 d\theta \sin\theta d\phi}{r^2} = \sin\theta d\theta d\phi \quad (2.16)$$

A hemisphere can be defined in space by integrating over the azimuth (i.e. a circle,  $0 < \phi < 2\pi$ ) and the angular distance between the normal and the horizontal (i.e.  $0 < \theta < \pi/2$ ). Expressing exitance over these limits we have:

$$M = \int_{\phi=0}^{2\pi} \int_{\theta=0}^{\pi/2} L \cos\theta \sin\theta d\theta d\phi \quad (2.17)$$

Which, when evaluated, gives:

$$M = \pi L \quad (2.18)$$

Thus exitance and radiance are related by a factor of  $\pi$  for Lambertian surfaces. This is an extremely important relationship because it becomes possible to calculate the spectral exitance of an isothermal surface from just one spectral radiance measurement, regardless of look angle or distance from source.

### 2.3. Temperature, Emissivity and Blackbodies

A blackbody is a hypothetical body that absorbs all photons incident upon it and reemits them out again without any conversion (i.e. loss) of energy. The spectral radiant exitance from a blackbody is given by the Planck function.

$$M(\lambda, T) = \frac{2hc^2}{\lambda^5 \left[ \exp\left(\frac{hc}{\lambda kT}\right) - 1 \right]} \quad (2.19)$$

where T is thermodynamic temperature in Kelvin, h is Planck's constant ( $6.626 \times 10^{-34} \text{ m}^2 \text{ kg s}^{-1}$ ), c is the speed of light in a vacuum ( $2.998 \times 10^8 \text{ m s}^{-1}$ ) and k is the Boltzmann constant ( $1.381 \times 10^{-23} \text{ m}^2 \text{ kg s}^{-2} \text{ K}^{-1}$ ). The blackbody spectral radiance from a Lambertian surface is therefore given by

$$B(\lambda, T) = M(\lambda, T)/\pi \quad (2.20)$$

The emission of radiance from physical materials is not perfect. This results in a deviation from blackbody behaviour. Spectral radiance of real physical bodies includes a spectral emissivity ( $\epsilon_\lambda$ ) term:

$$L(\lambda, t) = \epsilon(\lambda)B(\lambda, T) \quad (2.21)$$

The temperature of a remote surface can be determined by rearranging and substituting (2.19), (2.20) and (2.21) appropriately

$$T = \frac{hc}{\lambda k \ln \left[ \frac{\epsilon(\lambda)2hc^2}{\pi\lambda^5 L} + 1 \right]} \quad (2.22)$$

However, given the extensive, varied and dynamic nature of the terrestrial surface, we often do not know spectral emissivity a priori. This results in an ill-posed problem, i.e. more unknowns than equations, because each spectral radiance measurement will have a corresponding unknown spectral emissivity term plus some unknown temperature. There has been a significant amount of

work towards resolving this so called temperature-emissivity separation problem for the case where both temperature and emissivity spectra are homogeneous at the subpixel level. A review of these techniques is provided by Dash et al. (2002).

Total radiant exitance is given by the integral of (2.19) with respect to wavelength (i.e. the Stefan-Boltzmann law).

$$Q_{\text{rad}} = \sigma T^4 \quad (2.23)$$

where  $\sigma$  is the Stefan-Boltzmann constant. This shows that the radiant energy emitted by an isothermal blackbody surface is proportional to the 4<sup>th</sup> power of temperature, and that anything with a temperature above absolute zero will radiate energy.

The wavelength at which peak radiant exitance occurs was first found by thermodynamic consideration of electromagnetic radiation. It can also be found by determining the maxima of (2.19). It is described by Wien's displacement law,

$$\lambda_{\text{max}} = b/T \quad (2.24)$$

where  $b$  is  $2897.9\mu\text{mK}$ . This relationship shows that the hotter the surface the shorter the wavelength will be at which peak radiation occurs. It is especially useful when attempting to find a suitable part of the electromagnetic spectrum for a given application. For example, when attempting to determine the land surface temperature of ambient terrestrial environments (i.e.  $\sim 300\text{K}$ ) one would expect peak radiation to occur around  $9.7\mu\text{m}$ . Alternatively, an active lava surfaces at  $773\text{K}$  would probably display peak radiation at around  $3.8\mu\text{m}$ . The actual peak will depend on the spectral emissivity of the target.

## 2.4. Atmospheric Effects

Radiation that leaves the Earth's surface must pass through the atmosphere before reaching an orbital sensor. Photons can be absorbed, re-emitted and scattered by gases and aerosols (i.e. the primary constituents of the atmosphere). This interaction is wavelength dependent. The spectral transmissivity ( $\tau_\lambda$ ) of the atmosphere is given as:

$$\tau_{\lambda} = \frac{L_{TOA}}{L_{\lambda}} \quad (2.25)$$

where  $L_{TOA}$  is spectral radiance leaving the top of the atmosphere and  $L_{\lambda}$  is spectral radiance leaving the Earth's surface.

The dominant effects on transmissivity are the concentration of  $H_2O$ ,  $CO_2$  and aerosols in the atmosphere as well as the altitude of the target surface and viewing angle of the sensor (i.e. due to their control on the path length of photons within the atmosphere). The concentration of gas species and aerosols in the atmosphere varies temporally and spatially, they must therefore be accounted for when attempting to determine the amount of radiance that has left the Earth's surface. This is typically achieved through the use of a radiance transfer code such as Moderate Resolution Atmospheric Transmission (MODTRAN). An example MODTRAN transmissivity profile from Kliuchevskoi volcano (Kamchatka) is displayed in Figure 1.

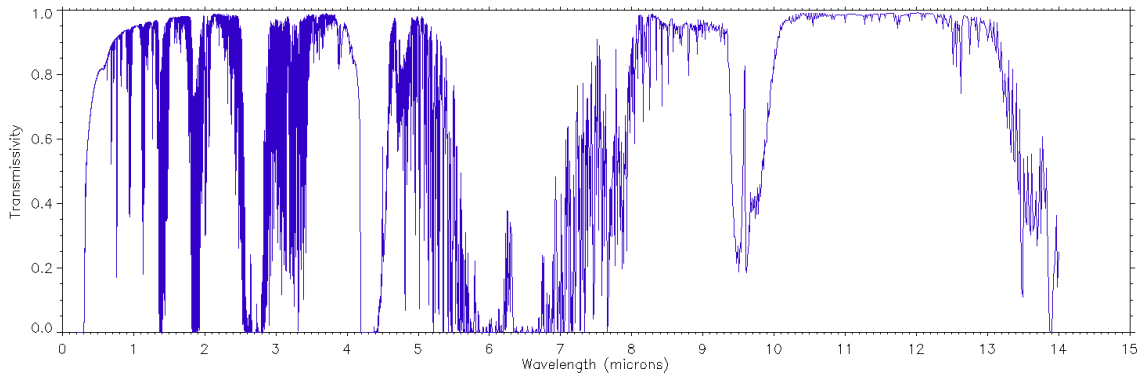


**Figure1. An example MODTRAN transmissivity profile from Kliuchevskoi volcano. The mid-latitude winter model was used for an at-NADIR sensor overpass.**

Remote sensing applications tend to utilize spectral regions in which the atmosphere is highly transmissive. These so called atmospheric windows have a fundamental control on the practical importance, and therefore nomenclature, of different spectral regions. Studies of radiant energy emitted by volcanic targets are restricted to the following spectral regions: the visible and near infrared (VNIR; 0.4 - 1.5  $\mu m$ ), the short-wave infrared (SWIR; 1.5 - 3  $\mu m$ ), mid infrared (MIR; 3 - 5  $\mu m$ ) and thermal infrared (TIR; 8 - 13 $\mu m$ ).

The spectral radiance that leaves a target surface will contain varying amounts of emitted and reflected components. The transmitted portion of that radiance will then reach a satellite detector, as will spectral radiance that is emitted and/or scatter by the atmosphere itself into the direction of that sensor. The spectral radiance,  $R_\lambda$ , can therefore be expressed as:

$$R_\lambda = \tau_\lambda \epsilon_\lambda L(\lambda, T) + \tau_\lambda \rho_\lambda R_{\lambda, D} + R_{\lambda, U} \quad (2.26)$$

where  $\tau_\lambda$  is spectral transmissivity,  $\epsilon_\lambda$  is spectral emissivity,  $L(\lambda, T)$  is blackbody radiation at temperature  $T$ ,  $\rho_\lambda$  is spectral reflectance of the surface,  $R_{\lambda, D}$  is the downwelling atmospheric spectral radiance on to the surface and  $R_{\lambda, U}$  is the atmospheric upwelling spectral radiance.

## 2.5. Issues with infrared monitoring of volcanoes from space

In order to be able to quantify volcanic thermal activity it is first necessary to be able to detect thermal anomalies. This can be achieved in a number of ways, all of which are dependent on either the spectral, spatial or temporal characteristics of the target (e.g. Steffke & Harris 2011). The most widely adopted approach is to use spectral information. This relies on setting a threshold above which a single pixel radiance value, or comparative radiance value (i.e. typically a band ratio), is considered to be anomalous. It has the benefit of being straight-forward and computationally efficient but will typically struggle to detect subtle thermal anomalies whilst maintaining a low false alarm rate.

In order to be able to detect subtle thermal anomalies it is usually necessary to analyze a pixel in terms of its spatial and/or temporal context. Perhaps the most intuitive approach is to determine if an area is significantly hotter than its surrounding. This is typically how a person might manually search for a thermal anomaly in a qualitative sense. In order to quantify this spatial approach to anomaly detection it is necessary to define a background value (i.e. a temperature or radiance value that represents the expected response from a thermally active area in the hypothetical case that it is not active). A background value in a spatial context is typically considered to be the average value within a background area. This area might be a single pixel or collection of pixels. There has been little investigation into the effect that background area selection has on anomaly detection capabilities. For low spatial resolution data this area is often

considered to be very few, i.e. often just one, pixel(s) that is/are juxtaposed to the potentially anomalous pixel. An area this proximal to the potential heat source, however, could itself contain volcanically active material. Furthermore, the effect of 'thermal blurring' (i.e. predominantly due to the point spread function of a detector element extending beyond the nominal surface area represented by a pixel) will also compromise the reliability that neighbouring inactive pixels represent the background conditions of the active pixel. For high spatial resolution data the background area is often defined manually on an *ad hoc* basis. There is therefore no guarantee of the stability of a manually selected background value. Notably there are strong, non-volcanic temperature gradients across volcanic edifices due to i) morphological aspect with respect to the solar azimuth and elevation angles, ii) altitude variations and iii) heterogeneous surface compositions. Thus the size and location of a background area might have a strong influence on the resultant background value.

Temporal methods for anomaly detection involve comparing a fixed pixel location through time (e.g. Tramutoli 1998, Pergola et al. 2004). This can be used to identify whether a consistently cool area has become warmer, or indeed whether a consistently hot area has become cooler. It is somewhat more difficult to identify temporal anomalies in an area that has shown a high level of variability during the time period under consideration. Hybrid approaches to anomaly detection (e.g. Giglio et al. 2003, Koeppen et al. 2011) do show significant promise in being able to improve subtle detection capability whilst maintaining a low false alarm rate. However, all anomaly detection schemes will be effected by ephemeral obstructions between the line of sight of the sensor and the target area (i.e. meteorological clouds, ash plumes, gas emissions and aerosols) as these phenomena have wavelength dependent effects on transmissivity and also vary both spatial and temporally.

Once a strategy for thermal anomaly detection has been selected it is usually necessary to quantify the intensity of the corresponding thermal activity. This is best achieved using metrics that are physically meaningful (e.g. temperature). A major issue with calculating surface temperatures from volcanic targets is that they are typically thermally heterogeneous at the pixel scale. Thus a single temperature value will not represent the continuous temperature distribution of the target. A number of techniques have been developed to attempt to resolve this so called 'thermal mixing' problem. They rely on the assumption that a subpixel temperature distribution can be modelled as a collection of isothermal components.

$$L_{pixel} = \sum_{i=1}^n f_i L_i \quad (2.27)$$

where  $L_{pixel}$  is the pixel radiance at a given wavelength,  $n$  is the number of isothermal subpixel components, and  $f_i$  and  $L_i$  are the size and radiance of the  $i^{th}$  component. To solve for equation 2.27 it is necessary to have at least as many spectral radiance measurements as there are subpixel thermal components. Initial attempts at subpixel thermal analysis were carried out using sensors that had just two pertinent spectral channels; they therefore assumed that just two thermal components were sufficient to reliably and accurately represent subpixel temperature distributions (e.g. Dozier 1981, Rothery et al. 1988, Oppenheimer 1991). As new sensors with a greater number of spectral channels were developed this model was extended to include three subpixel thermal components (e.g. Flynn et al. 1993, Oppenheimer 1993). It has since been shown, however, that volcanic temperature distributions cannot be reliably described using just 2 or 3 thermal components (e.g. Oppenheimer et al. 1993a, Wright & Flynn 2003). More recent attempts, which rely on model fitting of radiance spectra, have allowed the number of subpixel thermal components to be found automatically during the model fitting process (e.g. Wright & Flynn 2003). Oddly they found that model solutions with just 2 or 3 thermal components provided good spectral fits even though this was incongruent with high spatial resolution field data. This raises the question of whether or not there is a better approach for resolving subpixel components or, indeed, whether it is at all possible.

Satellite sensors will inevitably exhibit a trade-off between spatial, spectral and temporal resolution. Volcanic activity, on the other hand, manifests itself across spatial and temporal scales that vary by several orders of magnitude. A single satellite sensor will therefore only be able to monitor a small portion of on-going volcanic activity. It is therefore necessary to use multiple sensors to observe the full range of eruptive products emitted by volcanoes.

Forecasting volcanic eruptions is one of the major goals of volcanology as a whole. It is not a straight-forward task because volcanoes are highly non-linear complex systems and often display somewhat idiosyncratic behaviour. Even so, a rising magma body will often result in increased thermal activity at the surface (e.g. new and/or hotter fumarolic emission, increased ground temperature, increased crater lake temperature, the protrusion of a lava dome, etc), all of

which may precede an explosive eruption and/or flow of lava. Increased fumarolic activity was observed before two of the most deadly eruptions in historical times, i.e. Mont Pelee, Martinique 1902 with 29,000 fatalities; and Nevado del Ruiz, Colombia 1985 with 25,000 fatalities (Chrétien & Brousse 1989, Nakada 2000). Conversely, decreases in thermal activity have also been observed to precede explosive eruptions (Oppenheimer et al. 1993b). It can therefore be challenging to identify reliable thermal precursors.

## **2.6. Aims of this Work**

The overall aim of this work is to develop and test methods for improved global monitoring of volcanoes from space. The specific aims, outlined below, therefore address those issues that currently affect infrared monitoring of volcanoes using satellite observations.

- i) Improve anomaly detection capability through the investigation of methodologies for selection of background values and spectral thresholding.
  
- ii) Explore methods for quantifying volcanic thermal anomalies whilst accounting for subpixel thermal mixing. The metrics used must be as intuitive as possible to ensure adoption by the volcano monitoring community.
  
- iii) Investigate the development of sensor synergies to increase the resolution of monitoring data sets.
  
- iv) Identify new thermal precursors in order to aid those responsible for forecasting future eruptive events

# Chapter 3

## Monitoring Volcanic Thermal Anomalies from Space: Size matters

---

S. W. Murphy, C.R. de Souza Filho, C. Oppenheimer

Published in the Journal of Volcanology and Geothermal Research, 203, 48-61, 2011.

### **3.1. Abstract**

Measuring temperatures on volcanoes from space provides important constraints on the transfer of mass and heat to the Earth's surface. Time series of multispectral infrared images, acquired by the Advanced Spaceborne Thermal Emission and Reflection Radiometer (ASTER) between 2000 and 2009, were inspected to investigate fluctuations in thermal anomalies at both Mount Erebus (Antarctica) and Láscar volcano (Chile). Several thermal metrics were explored: i) maximum pixel temperatures above background, ii) the spatial extent of low, moderate and high temperature anomalies, and iii) the spatial extent of short-wave infrared anomalies. The maximum pixel temperature metric correlated to eruptive events at Láscar volcano yet displayed significant scatter at Erebus. The spatial extent of both temperature and short-wave infrared anomalies correlates well with eruptive activity at both volcanoes.

Limited variation in the size of thermal anomalies was observed at Erebus throughout the time series due to the stability of a long-lived lava lake, with the exception of a seasonal

expansion in low temperature anomalies associated with localized snow-melt at the peak. This finding has implications for the interpretation of low temperature anomalies at other volcanoes. At least two different types of precursory signals are identified at Láscaar: i) a gradual increase and ii) a dip, in the size and intensity of thermal anomalies. These thermal precursors appear to be associated with different eruptive styles. The former precedes a relatively shallow, short lived eruption; the later a prolonged eruptive period. Such thermal precursors could therefore help to constrain not only the timing but also the style and duration of an imminent eruptive episode.

### **3.2. Introduction**

Volcanoes are hazardous, non-linear systems and so require regular monitoring if timely forecasts of eruptive behaviour are to be given and if we are to improve our understanding of dynamic volcanic processes. Ideally volcanologists would have access to information from all of the world's subaerial volcanoes. This way a greater understanding of fundamental volcanic processes can contribute to the expert knowledge required to deal with specific volcanoes that may be endangering communities or property. Orbital remote sensing provides the necessary perspective to fulfil such an ideal and is often the only source of information available for many remote volcanoes.

The approach adopted in this study is to measure the temperature of active volcanoes from space using multispectral thermal infrared (TIR) images taken by the Advanced Spaceborne Thermal Emission and Reflection Radiometer (ASTER), currently the only multispectral TIR sensor in orbit with moderate (<100 m) spatial resolution imagery that is available to the civilian community. Previous authors have utilized the combined spatial and spectral resolution of this sensor to describe volcanic activity. Special consideration has been given to the reliability of terrestrial surface temperature estimates at these wavelengths (i.e. 8.125–11.65  $\mu\text{m}$ ). The metrics used to quantify such observations have included the maximum pixel temperature (Ramsey and Dehn, 2004; Vaughan and Hook, 2006; Carter et al. 2008), the average crater temperature (Vaughan and Hook, 2006) and the maximum pixel temperature above background (Ramsey and Dehn, 2004; Pieri and Abrams, 2005; Vaughan et al. 2008; Carter et al. 2008). Although these thermal parameters were all shown to correlate with volcanic activity, they do not measure the actual size of the anomaly (Carter et al. 2008). This study aims toward developing methods for

measuring both the size and intensity of volcanic thermal anomalies. We further support the investigation of TIR-based thermal anomalies by comparison to ASTER's short-wave infrared (SWIR) bands.

In order to explore an existing TIR-based parameter we first analyze temporal fluctuations in maximum pixel temperature above background. This parameter was selected because it is the most widely adopted in the previous literature, accounts for non-volcanic seasonal variations in temperature and has been shown to correlate particularly well with eruptive behaviour. We then describe the change in the size and intensity of thermal anomalies (both TIR- and SWIR based) through time at Mt. Erebus (Antarctica) and Láscar (Chile). These targets exhibit markedly different styles of volcanism and are situated thousands of kilometres apart from each other, thus providing a contrast in eruptive styles as well as demonstrating one of the advantages of the global perspective available from space.

### **3.3. Study areas**

#### 3.3.1. Erebus volcano

Erebus volcano (77°32'S, 167°10'E, 3794m) is an alkaline intraplate stratovolcano situated on Ross Island, Antarctica (Fig. 3.1) (Kyle et al. 1992; Oppenheimer et al. 2011). It contains one of the few permanent, terrestrial lava lakes. The bulk composition of its phonolitic lava appears to have remained unchanged over the last ~36 ka (Harpel et al. 2004; Esser et al. 2004; Kelly et al. 2008). The lake is thought to be sustained by magma convection via a conduit leading to a reservoir at depth. The first historical sighting of the volcano was reported in 1841 (Ross, 1847), with a lava lake having been observed in the active crater since modern observations began in 1972 (Giggenbach et al. 1973).

The permanent lake (referred to in the recent literature as Ray's lake) is sometimes accompanied by an ephemeral lake (at Werner's fumarole). Construction of the volcano began around 1.3 million years ago and is associated with crustal thinning and a possible mantle plume. The arid, polar climate in which the volcano is situated suppresses cloud cover and, coupled with the volcano's constant activity, makes Mount Erebus an excellent target for developing space-

based thermal monitoring techniques of active volcanoes (e.g. Harris et al. 1999; Davies et al. 2008; Wright and Pilger, 2008; Vaughan et al. 2010)

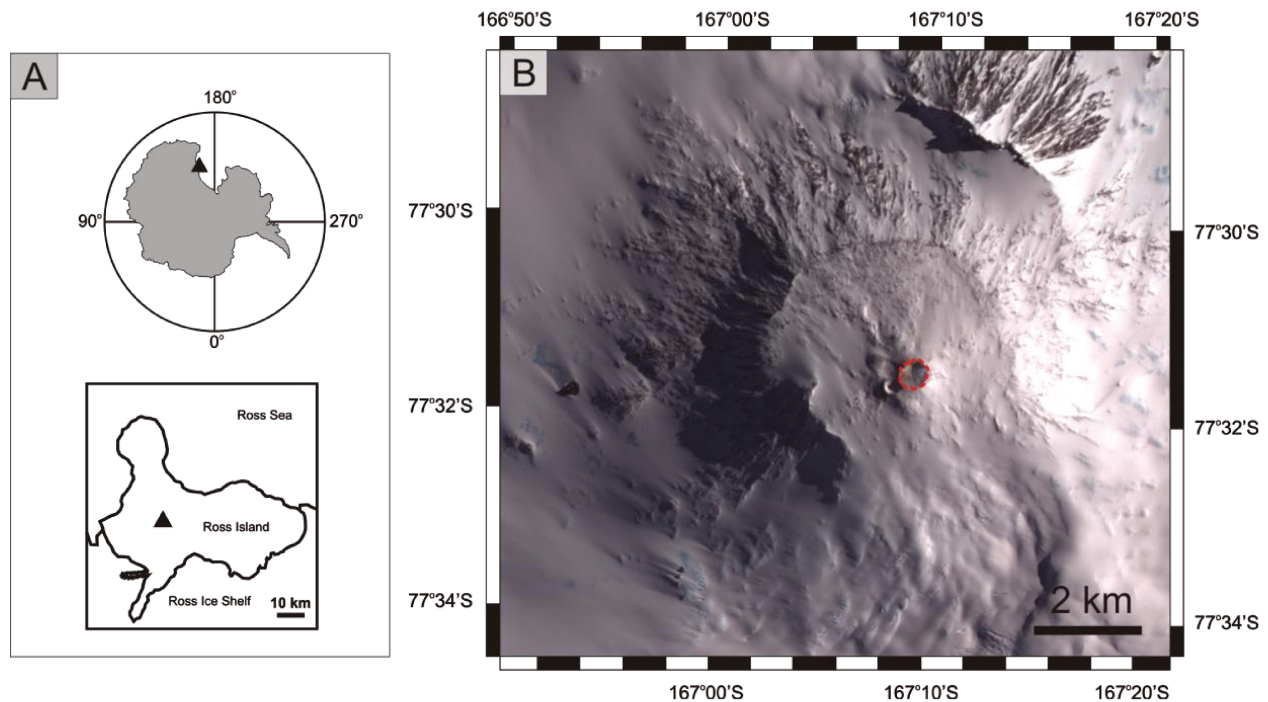


**Figure 3.1. a) The location of Mount Erebus (Antarctica) and b) an ASTER VNIR image of the volcano, taken on the 13th January 2008, with the active crater highlighted (red dashed line).**

### 3.3.2. Láscar volcano

Láscar ( $23^{\circ}22'S$ ,  $67^{\circ}44'W$ , 5592 m) is a young ( $< 50$  ka old; Matthews et al. 1997) compound stratocone situated in the Chilean Altiplano to the East of the Salar de Atacama (Fig. 3.2). It is built from porphyritic andesites and dacites (Matthews et al. 1994). Historical activity is recorded back to 1848 (Venzke et al., 2002 -). The high and arid environment is associated with limited cloud, vegetation, snow and ice cover, thus making Láscar a very suitable terrain for geological remote sensing (de Silva and Francis, 1991). These environmental factors, coupled with Láscar's persistent degassing and frequent small-to-moderate explosive eruptions, have favoured numerous remote sensing studies of Láscar volcano over the past quarter century (e.g. Francis and Rothery, 1987; Oppenheimer et al. 1993b; Wooster, 2001; Pavez et al. 2006).

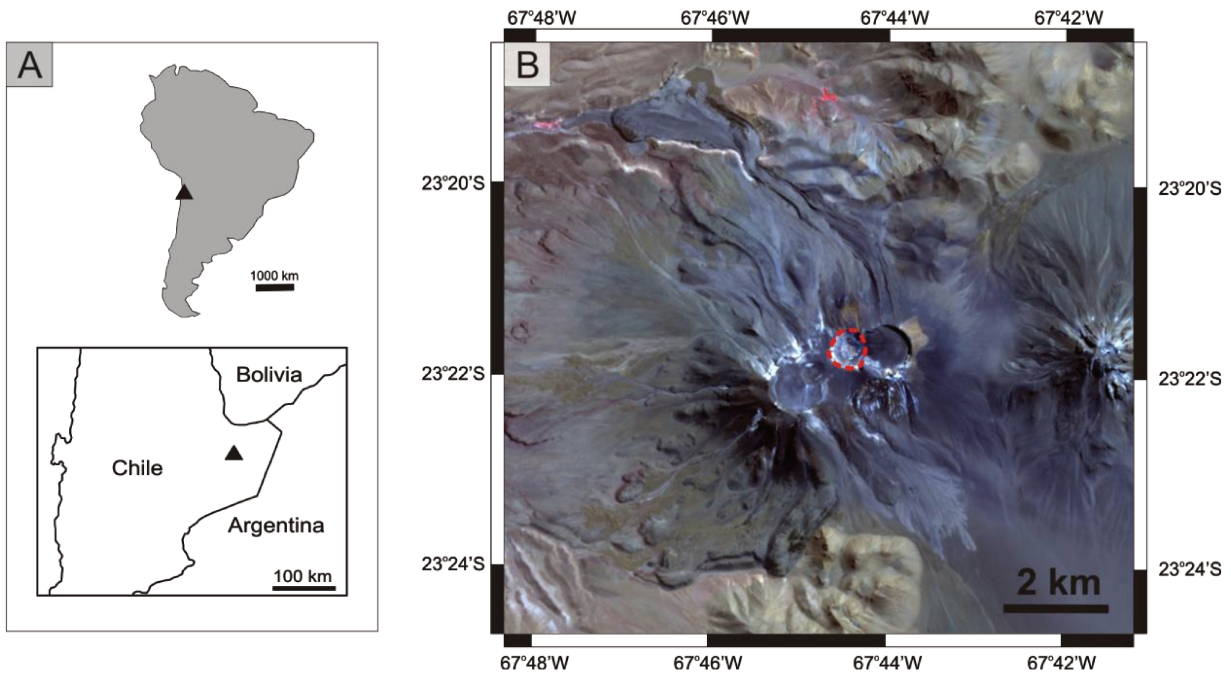


**Figure 3.2. a) The location of L ascar volcano (Chile) and b) an ASTER VNIR image of the volcano, taken on the 2nd April 2009, with the active crater highlighted (red dashed line).**

### 3.4. ASTER and data processing

The ASTER sensor, launched onboard the Terra satellite, has been acquiring multispectral images of the Earth's surface for just over a decade. The imaging wavebands of this sensor fall into three spectral regions: i) the visible and near-infrared (VNIR), with four channels from 0.52 to 0.86  $\mu\text{m}$ , 15 m spatial resolution and stereoscopic viewing capability, ii) the short-wave infrared (SWIR), which has six channels from 1.6 to 2.43  $\mu\text{m}$  and 30 m spatial resolution, and iii) five channels in the thermal infrared with 90 m spatial resolution (Yamaguchi et al. 1998). Acquisition of SWIR data ended in early 2008 due to degradation of the detector cooler system. ASTER scenes are available at various processing levels, including raw at-sensor radiance values (L1A) as well as geometrically and radiometrically corrected sensor radiance values (L1B), which can be used to derive level 2 data products, such as atmospherically corrected surface radiance or surface temperature and emissivity.

This study uses the TIR at-surface radiance data product (AST\_09T). These scenes were visually scrutinized for the presence of clouds and discarded if cloud formations were situated

over the volcano. The images were then converted into land surface temperatures using the Normalized Emissivity Method (NEM) (Realmuto, 1990) using a maximum emissivity value of 0.97. The resulting surface temperature estimates are dependent, among other factors, on seasonal and diurnal cycles as well as potential volcanic activity. To suppress non-volcanic variations through time we first calculate the background temperature,  $BT_k$ , as follows:

$$BT_k = \sum_{i=1}^n T_{i,k}/n \quad \text{where } i \in \beta_k \quad (3.1)$$

where  $T_{i,k}$  is a pixel temperature and  $n$  is the number of pixels in the background area  $\beta_k$  for the  $i^{\text{th}}$  pixel in the  $k^{\text{th}}$  scene. The background temperature is therefore the average temperature of pixels within the background area. A temperature above background,  $\Delta T$ , is found by subtracting the background temperature from a given pixel:

$$\Delta T_{i,k} = T_{i,k} - BT_k \quad (3.2)$$

Pixels close to background temperature will have low  $\Delta T$  values while volcanically heated pixels will be represented by positive  $\Delta T$  anomalies.

### 3.4.1. Background areas

As stipulated in Eq.(3.1) a background area is required to calculate a background temperature. Land surface temperatures are not homogenous. Therefore the size, shape and location of the background area will affect the background temperature. In previous studies these areas have ranged in size and location from a few pixels that are juxtaposed to anomalous regions, to 50×50 pixel arrays situated on neighbouring topographic peaks (e.g. Ramsey and Dehn, 2004; Pieri and Abrams, 2005; Carter et al. 2008; Vaughan et al. 2010). To demonstrate the potential sensitivity of background temperatures to the location of the background area we defined a square-shaped sample area (10 × 10 pixels) and moved it through 16 different, non-overlapping locations around the centre of volcanic activity (Fig. 3.3). A background temperature was calculated for 16 such footprints for each scene. We then repeated this procedure for all scenes in the data set.

With the exception of gas/aerosol plumes, reported volcanic activity is constrained within the active crater at both volcanoes. The sample areas are always situated at least 15 pixels (i.e. 1.35 km) beyond the crater centre. Inspection of temperature images reveals that the plumes have negligible thermal influence at such distances. In the presence of significant SO<sub>2</sub> in the plume the NEM algorithm is still capable of producing reliable temperature retrievals due to automatic selection of the most appropriate band (e.g. in this case either ASTER band 13 or 14, both of which avoid SO<sub>2</sub> absorption features). The background temperatures recorded by each of the footprints can therefore be considered as non-volcanic.

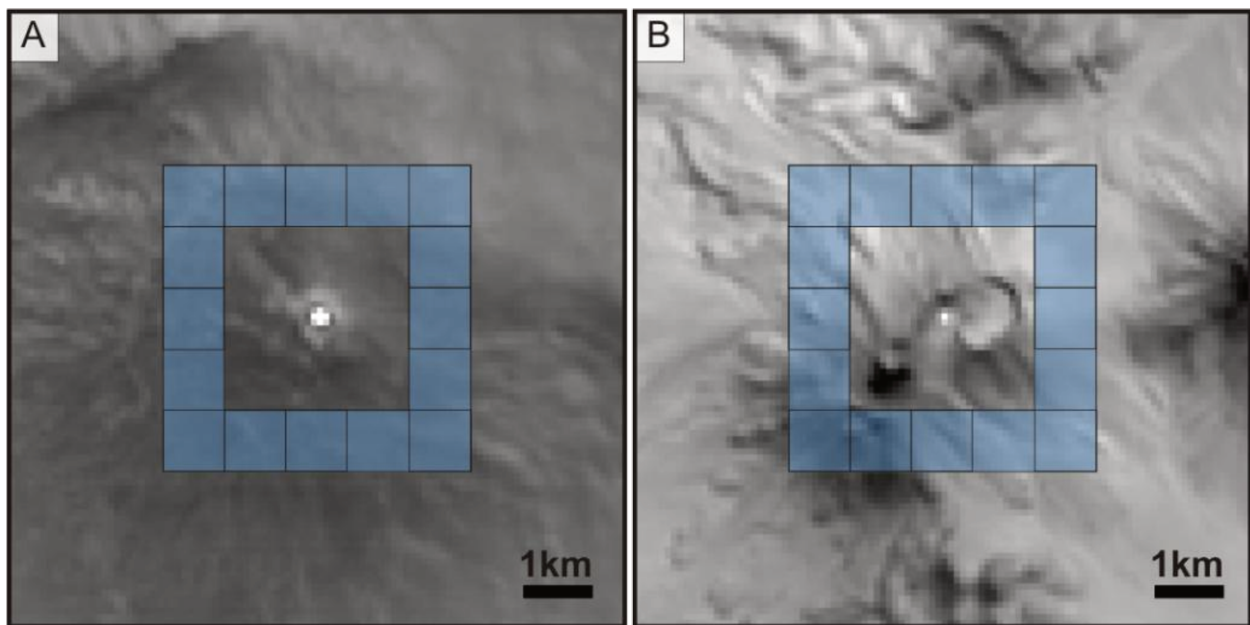


**Figure 3.3.** The box-shaped areas used to sample background temperatures at both a) Erebus and b) Láscar. The boxes are 10 pixels (i.e. 900 m) in length. North is up in both images.

The range (i.e. absolute difference between minimum and maximum) of background temperatures for the 16 grids was calculated on a scene by scene basis and plotted for a) Erebus and b) Láscar throughout the 2000–2009 time series (Fig. 3.4).

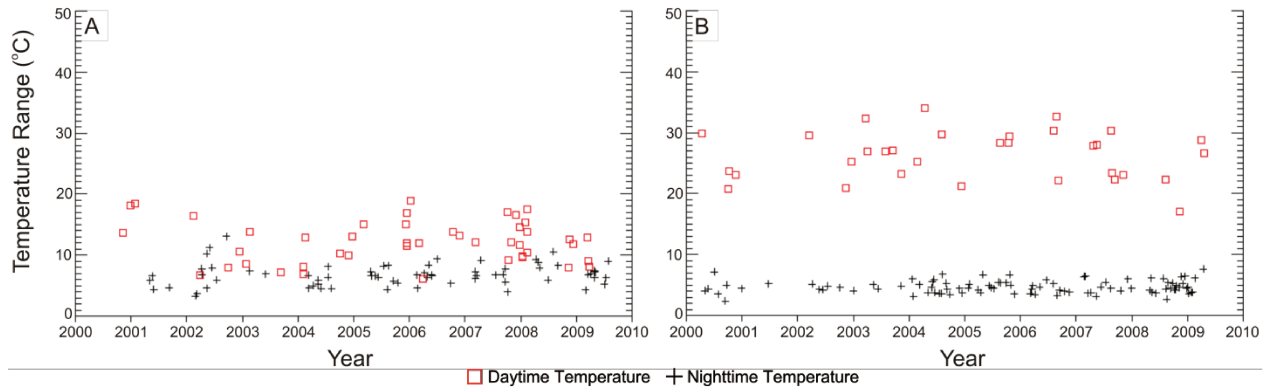


**Figure 3.4. The range in box sample temperatures at a) Erebus and b) Láscar. Red squares and black crosses symbolize daytime and nighttime scenes, respectively.**

This provides an indication of the sensitivity of a background temperature to the location of the background area. Nighttime scenes (black crosses - Fig. 3.4) tend to display a limited range in sample temperatures (i.e. means of 6.7 °C at Erebus and 4.7 °C at Láscar). This indicates that they are less sensitive to the location of the background area than the daytime scenes (red squares - Fig. 3.4) which have mean ranges of 12.2 °C at Erebus and 26.3 °C at Láscar. The maximum range in background temperatures is 18.9 °C at Erebus and 34.0 °C at Láscar. Hence there is a significant dependence of the background temperature on the location of the background area at both volcanoes, especially during the daytime. We interpreted this dependence as being predominantly due to preferential solar heating arising from variations in slope, aspect and solar azimuth at the time of image acquisition.

The sensitivity to diurnal effects as a result of slope aspect can be mitigated by defining the background area as an annulus around the active crater (as opposed to the square regions displayed in Fig. 3.3). Such a background will act to balance out topographically driven thermal heterogeneities and therefore stabilize background temperature estimates, even during the day. To define a ring-shaped area it is necessary to assign appropriate values for the inner and outer radius.

### 3.4.2. Radius pairs

To determine which inner and outer radius pair is most appropriate, sample temperatures were calculated for the area defined by all possible combinations of radius pairs that obey the following two criteria i) the inner radius may vary between 0 and 39 pixels, and ii) the outer radius may vary between 1 and 40 pixels but must be larger than the inner radius. This produces a total of 820 separate ring sample temperatures for each scene

To select the optimum radius pairs we impose two constraints. The first is based on the assumption that a radial profile of temperatures will tend to decrease monotonically toward the active crater due to topographic effects up until the point at which that profile passes through a volcanically heated area. The coldest ring temperature will therefore provide the best estimate of the non-volcanic (i.e. background) temperature in the active crater. The second constraint is that the total area of the background ring should be sufficiently large to smooth out unrepresentative pixel temperatures (e.g. due to the presence of undetected clouds and/or volcanic products, etc.). We define ‘sufficiently large’ as an area of at least 400 pixels based on the suggested size of a standardized array given by Vaughan et al. (2010). The background temperatures are not sensitive to this minimum size constraint, as shown below.

To validate the first constraint we calculated ring sample background temperatures for neighbouring, inactive volcanic peaks (i.e. Aguas Calientes for Láscar and Mount Bird for Erebus). The deviation of each ring sample from the minimum ring sample was then calculated on a scene by scene basis to locate the coldest annular regions and to facilitate comparisons through time. The average deviation of ring samples from minimum was then calculated for all scenes in order to provide a metric that indicates by how much a given radius pair will tend to deviate from the coldest sample temperature (Fig. 3.5).

As expected, ring temperatures tend to be coldest at the top of these peaks (i.e. low radii values) and to warm up progressively down slope (i.e. warmer temperatures correspond to higher radii values). Aguas Calientes displays greater thermal contrast on average between minimum and maximum ring temperatures at this scale (i.e. average range of ~9 °C at Aguas Calientes and ~6 °C at Mount Bird). This is presumably due to the more pronounced relief at Aguas Calientes as well as the stronger thermal heterogeneity in daytime land surface temperatures on the Altiplano in comparison to Ross Island.

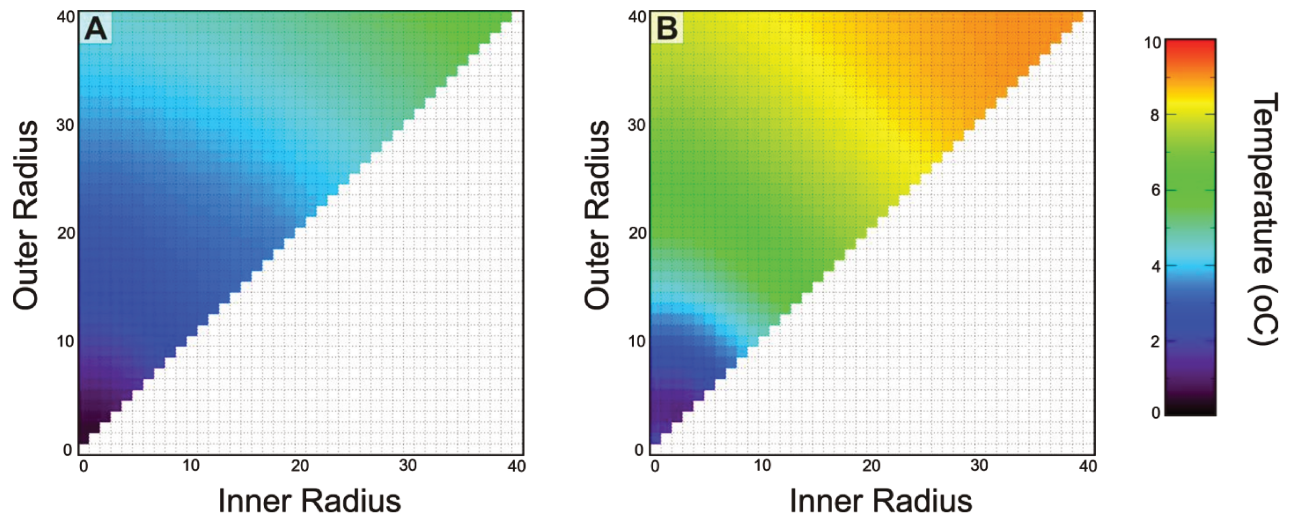


**Figure 3.5.** Average deviation of ring sample temperatures from the minimum ring sample temperature for neighbouring, non-active topographic peaks at a) Mt. Bird (Antarctica) and b) Aguas Calientes (Chile).

Volcanic heating can clearly perturb a temperature gradient, with the active region becoming significantly warmer than the surrounding area. The average deviation of ring sample temperatures from minimum is calculated for a) Erebus and b) Láscar (Fig. 3.6).

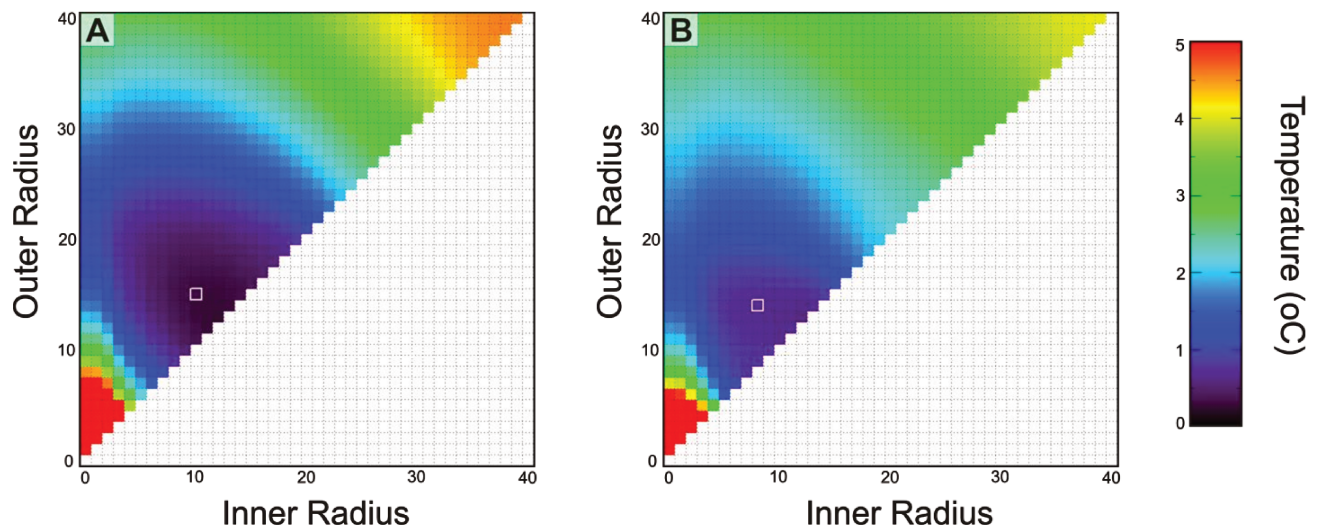


**Figure 3.6.** Average deviation of ring sample temperatures from the minimum for a) Erebus and b) Láscar volcano. Optimum radius pairs are highlighted with a white square outline.

Areas close to the active crater (i.e. low radii values) tend to be relatively hot. The coolest regions are situated fairly close to the active peak (i.e. the blue-black arc shaped region). Regions that are further out still (i.e. high radii values) tend to be relatively warm as they are situated at lower altitude. The optimum radius pairs (i.e. coldest average ring which is at least 400 pixels in size) have inner and outer radii of i) 10 and 15 pixels at Erebus, and ii) 8 and 14 pixels at Láscar. They are highlighted using a white square outline in Fig. 3.6. These optimum background areas are displayed for both a) Erebus and b) Láscar in Fig. 3.7.

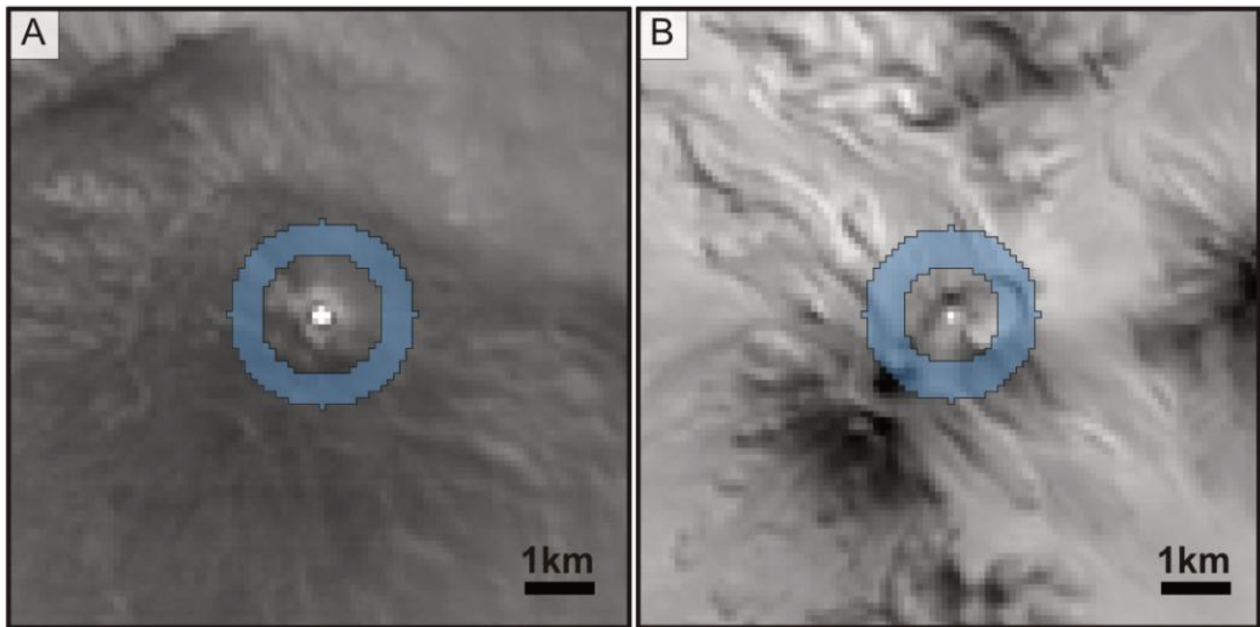


**Figure 3.7. The size and location of optimum ring-shaped background areas at both a) Erebus and b) Láscar. North is up in both images.**

Comparison between the optimum ring temperatures and the minimum ring temperatures on a scene by scene basis reveals that their average difference is  $0.29 \pm 0.25$  °C at Erebus and  $0.68 \pm 1.0$  °C at Láscar. The optimum background temperatures are therefore generally insensitive to the minimum size constraint. Even so the implementation of this constraint will yield a more reliable background temperature estimate. Furthermore, the fact that background areas are allowed to adapt to each volcano represents a crucial step toward facilitating the use of this technique on a global basis.

### 3.4.3. Background temperatures

Having defined the optimum size, shape and location of a background area it is possible to calculate the background temperature for a given scene (i.e. Eq.(1)). The background temperature is calculated for all scenes at both a) Erebus and b) Láscar (Fig. 3.8).

Comparison of background temperatures highlights climatic differences at both volcanoes. The background temperatures tend to be significantly colder at Erebus (Fig. 3.8a) than at Láscar (Fig. 3.8b), ranging from approximately  $-50$  to  $-20$  °C at the former and  $-15$  to  $35$  °C at the latter. However, the disparity between daytime and nighttime temperatures is more pronounced at Láscar. This is due to the fact that the volcano is situated at subtropical latitudes on a desert Altiplano, while Erebus is situated at polar latitudes and spends the majority of the year in either continuous darkness or continuous light, with a 24 hour diurnal cycle only occurring during the Austral spring and autumn. A recent independent field measure taken from within the active crater on the 13th December 2005 (Vaughan et al. 2010) found a background temperature value (i.e.  $-15.8$  °C) that is comparable to our concurrent value of  $-19.0$  °C measured from space.

The ASTER sensor is in a sun-synchronous orbit therefore images of a given point on the Earth's surface are acquired within a fixed time window for ascending and descending orbits. Image acquisitions of Erebus occur at either 14:05 +/-30 or 20:32 +/-20 UTC, while images of Láscar are acquired at either 14:51 +/-10 or 03:20 +/-10 UTC. The benefit of taking images at the same time of day or night is that diurnal variations in temperature are suppressed. Meteorological effects have also been minimized by screening out cloudy scenes. Seasonal effects are therefore the major influence on background temperatures in these time series. A reasonable model of this effect can be achieved through the use of a sinusoidal function (Eq. 3.3).

$$BT^* = a \sin(\omega t + \varphi) + c \quad (3.3)$$

where  $BT^*$  is the modelled background temperature,  $a$ , is the amplitude of seasonal temperature fluctuations,  $\omega$  is angular frequency (i.e.  $2\pi$  per year),  $t$  is time,  $\varphi$  is the phase (i.e. onset of the seasons) and  $c$  is the point about which the function oscillates (i.e. approximately the average temperature of the time series). The model is justifiable because seasonal effects are

predominantly controlled by a stable cyclic motion (i.e. the Earth revolving around the sun), that does not show significant perturbation over this timeframe.

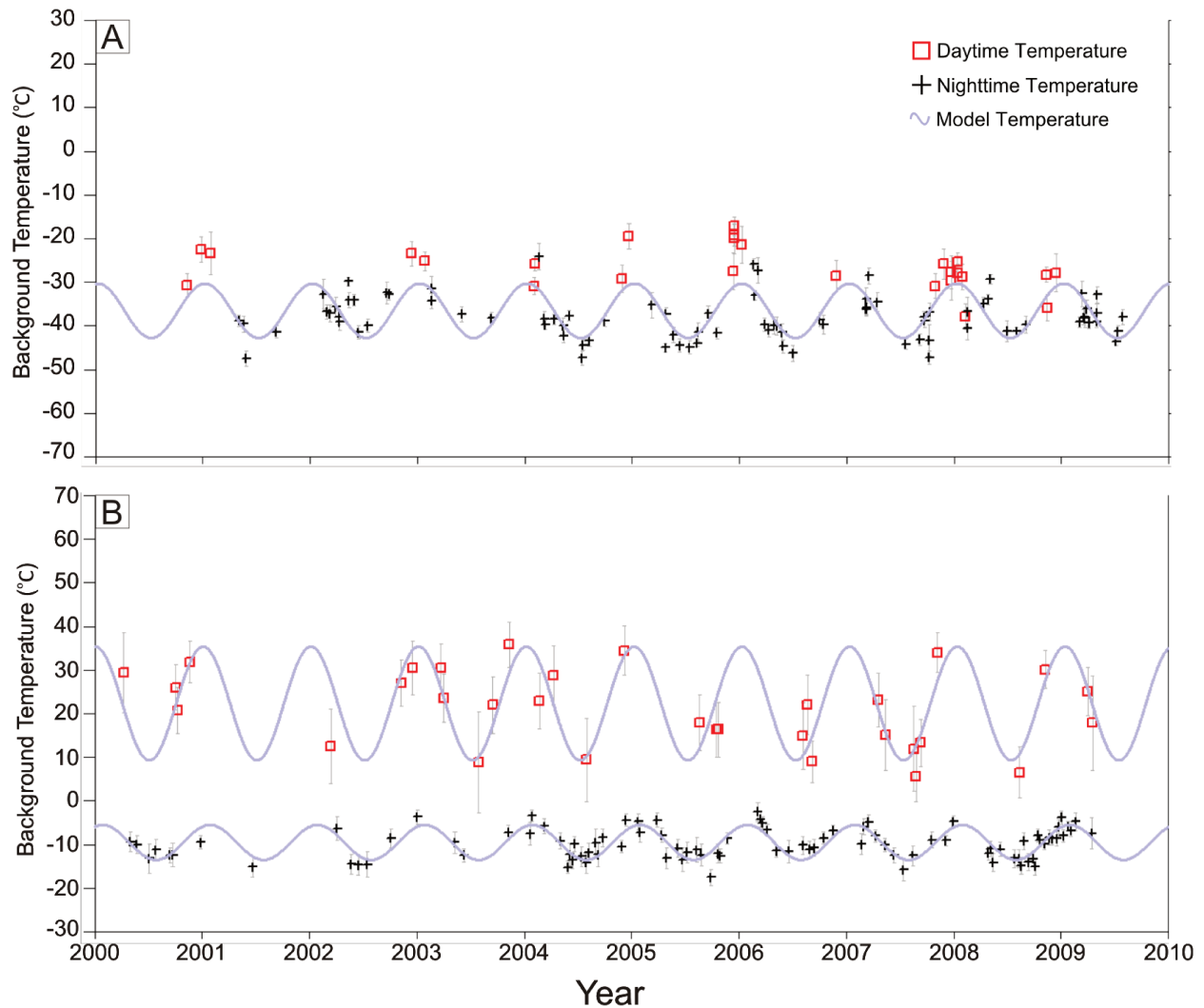


**Figure 3.8. The background temperatures of a) Erebus and b) Láscaar volcanoes from 2000 to 2009. Red squares and black crosses denote daytime and nighttime images, respectively. Error bars are one standard deviation.**

Daytime and nighttime temperatures are modelled separately for Láscaar although such a distinction is not made at Erebus as polar diurnal and seasonal cycles are somewhat synchronized. Models are fit using least-squares regression. The mean absolute error from the model is less than 4.5 °C for all data sets (Table 3.1). Láscaar daytime scenes display the largest BT\* amplitude, indicating that they are the most susceptible to seasonal variations. The best fit is

provided by Láscaar night-time series. However, we observe that while Láscaar day and night scenes should be in phase they are ~100 days apart. We attribute this discrepancy to the limited number of daytime scenes in this data set and correspondingly poorer constraint of the daytime model.

**Table 3.1. The least-squares best fit of sinusoidal model parameters on background temperatures. Mean and maximum absolute errors are also provided.**

Data Set	Amplitude (°C)	Vertical Offset (°C)	Phase (days)	Mean Absolute Error (°C)	Maximum Absolute Error (°C)
Erebus (day & night)	6.2	-36.5	42.4	3.7	13.7
Láscaar (day)	13.0	22.4	175.2	4.5	9.6
Láscaar (night)	4.0	-9.5	67.0	1.7	3.9

### 3.5. Anomalous volcanic temperatures

Although the ASTER sensor is particularly well suited to calculating terrestrial temperatures, existing metrics that describe volcanic temperatures estimates from space are limited in the sense that they do not identify all anomalous pixels. Instead they measure either the single hottest pixel temperature (e.g. Ramsey and Dehn, 2004; Pieri and Abrams, 2005; Vaughan and Hook, 2006; Carter et al. 2008; Vaughan et al. 2008), which may undergo a sub-pixel component analysis (e.g. Pieri and Abrams, 2005 and Hirn et al. 2008), or they measure a crater-averaged temperature (Vaughan and Hook, 2006). The maximum temperature above background has arguably proved the most insightful metric so far. It has been used to detect new high temperature features, such as fumaroles and lava domes (e.g. Ramsey and Dehn, 2004; Vaughan et al. 2008) as well as to describe cooler materials such as pyroclastic flow deposits and lahar deposits (e.g. Ramsey and Dehn, 2004; Carter et al. 2008). As mentioned previously, however, a significant drawback of measuring just the maximum pixel temperature is that it does not provide any spatial information regarding anomalies (Carter et al. 2008). For example, the same maximum temperature value could correspond to a small isolated anomaly on one date and a larger widespread anomaly on

another. We propose that an improved measure of volcanic activity would account for all anomalous pixels. To create such a metric it is necessary first to define an appropriate threshold for thermally anomalous pixels.

### 3.5.1. Anomalous hot pixels

For a pixel to be considered anomalously hot it must exceed the background temperature by a significant amount. Such a threshold can be determined by calculating the natural variability of  $\Delta T$ s within a dataset and then defining a statistical limit above which background  $\Delta T$ s are not expected to exceed. To achieve such a goal it is necessary to convert individual  $\Delta T$ s into a measure of variability. We use z-scores,  $z_{i,k}$ , for this purpose, given by:

$$Z_{i,k} = \Delta T_{i,k} / \sigma_k \quad (3.4)$$

where  $\Delta T_{i,k}$  is a pixel temperature above background and  $\sigma_k$  the standard deviation of the background temperature, and subscripts denote  $i^{\text{th}}$  pixels in  $k^{\text{th}}$  scenes. A z-score is therefore a normalized measure of deviation from the background temperature. The background (i.e. mean) temperature is represented by a z-score of zero. A pixel temperature that is one standard deviation above or below this mean will have a z-score of 1 or  $-1$ , respectively.

A frequency distribution (i.e. histogram) of z-scores can be converted into a probability density function (PDF) by normalizing appropriately. We determine a PDF of z-scores for all scenes at A) Erebus and B) Láscaar that were acquired by i) day and ii) night (Fig. 3.9). These PDFs represent the expected deviation of background pixels from the background temperature in units of standard deviations.

Daytime distributions are somewhat bimodal, this is presumably due to the amalgamation of two principal temperature distributions which correspond to i) surfaces on the volcanic edifice that are more exposed to solar radiation and ii) surfaces that are in shadow. Nighttime distributions are unimodal at both volcanoes and quite strongly asymmetric at Láscaar, with the mode (i.e. peak probability) occurring distinctly above the mean. This may be due to more efficient heat loss from relatively warm areas, which consequently bunches together pixel temperatures that are above the mean.

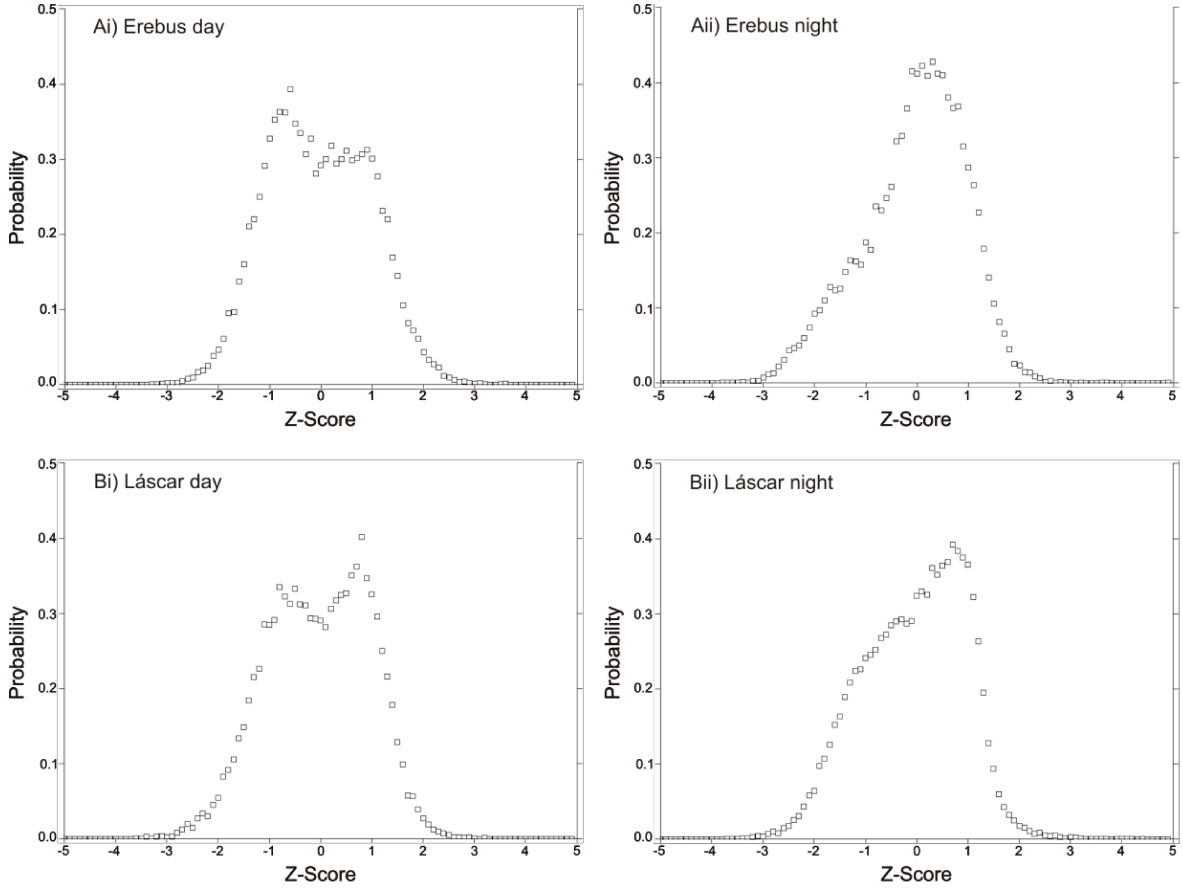


**Figure 3.9. Probability density functions of background z-scores at a) Erebus, v) Láscar during i) the day and ii) the night, calculated using all scenes in each dataset.**

We can see from these PDFs that the vast majority of pixel temperatures will not exceed the background temperature by more than two standard deviations. In particular, 99% of z-scores are below two at Láscar (during the day or night) as well as for the Erebus night time series, while 98% of scenes have z-scores below two for the Erebus daytime series.

An anomaly could be defined on a scene by scene basis by using a given z-score threshold. However, as variations in background temperatures are seasonally dependent, it follows that such a measure of anomaly would also be seasonally dependent. To introduce a more consistent measure of thermal anomaly through time we select the maximum standard deviation of background temperatures within a time series,  $\sigma_{\max}$ , and use twice its value as a threshold. A pixel is therefore considered to be anomalous if it satisfies the condition outlined in equation 3.5.

$$\Delta T_{i,k} - 2\sigma_{\max} > 0 \quad (3.5)$$

This provides a fixed criterion for detecting anomalies in a given time series and a very low false alarm rate. The maximum standard deviation of background temperatures at Erebus and Láscar are 4.9 and 11.7 °C during the day and 2.4 and 3.6 °C during the night, respectively. Temperatures above background would therefore be considered as anomalously hot if they exceeded 9.8 °C or 23.4 °C for daytime series, and 4.8 °C or 7.2 °C for nighttime series at Erebus and Láscar, respectively. We note that variability in daytime temperatures hinders subtle thermal anomaly detection. Nonetheless, the metric proposed here accounts for the natural fluctuation within a dataset and describes a statistical limit beyond which we identify volcanogenic heating.

### 3.5.2. The spatial extent of thermal anomalies

Given this quantification of ‘anomalously hot’ pixels it is possible to determine the overall size of anomalous areas by simply counting the relevant pixels. In order to focus on local volcanic effects the target area for such an anomaly search was defined as the circular region within the background area. The frequency distributions of anomalous temperatures can also be obtained by binning pixels into given temperature ranges. This discriminates, for example, large cool areas from small hot areas, thus facilitating the interpretation of thermal anomalies. Here, we classify three anomaly classes as follows: i) cool ( $\Delta T < 30$  °C), ii) moderate ( $30 < \Delta T < 60$  °C) and iii) hot ( $\Delta T > 60$  °C). We avoid defining a larger number of narrower thermal regions at present given that it may not be appropriate at this spatial resolution.

### 3.5.3. SWIR anomalies

Nighttime short-wave infrared anomalies are also calculated using an analogous background value and standard deviation threshold, although in this case to differentiate from sensor noise as opposed to seasonal or diurnal affects. We did not analyze daytime SWIR images as solar irradiation tends to significantly hinder anomaly detection at these wavelengths. It is important to note that saturation occurs frequently in the SWIR wavebands over these targets (i.e. in 84% of Erebus scenes and 48% of Láscar scenes). This arises because the upwelling radiation reaching the satellite sensors often exceeds the dynamic ranges of the various ASTER SWIR detectors and therefore limits the extent to which the SWIR channels can be used for quantitative

measurements. As such we limit classification of pixels within SWIR scenes to the binary case of being either anomalous or not anomalous.

## 3.6. Results

### 3.6.1. Maximum temperatures above background

A series of maximum pixel temperatures above background are given for a) Erebus and b) Lásca (Fig. 3.10). The Erebus time series (Fig. 3.10a) reveals considerable scatter in both daytime and nighttime scenes and no clear secular trends. On the other hand, Lásca displays a more coherent temporal pattern (Fig. 3.10b) which appears to show pronounced changes in intensity with respect to most of the reported erupted episodes at Lásca (Bulletin of the Global Volcanism Network. Lásca. 2000, 2003, 2004, 2005, 2006, 2007). The reported mid-points of these episodes are highlighted as triangles in Fig. 3.10b.

The scatter at Erebus appears to be incongruent with the limited variation in thermal output from the lava lake that has been observed using both long term orbital data (Wright and Pilger, 2008) and field thermography (Calkins et al. 2008; Oppenheimer et al. 2009). There are several potential contributing factors to this scatter. One such influence is the dependence of pixel temperatures on the fractional area of the lake within a given pixel. The size of the lake during this time period varied between  $\sim 700$  and  $1400 \text{ m}^2$  (Csatho et al. 2008; Calkins et al. 2008) while each ASTER TIR pixels corresponds to an area of  $\sim 8100 \text{ m}^2$ . The lake may therefore ‘fit’ completely within a single pixel or be divided between up to four pixels. The number of pixels within which the lava lake is imaged will influence the maximum temperature of a given scene. This dependency is modelled below (see Discussion) using a 3-component model of the lava lake system, with hot cracks, crust and non-volcanic background, to demonstrate that maximum pixel temperatures vary significantly as a function of the maximum proportion of the lava lake within a given pixel.

Other factors that may also create scatter in maximum pixel temperatures at Erebus include i) the concentration, composition and location of aerosols and gas plumes, ii) short time scale variations in radiative output from the lake due to pulsatory magma supply and gas emission, iii) the amount and temperature of spatter around the lake, iv) the disposition of other

thermal anomalies within the Erebus crater (e.g. the ephemeral ‘Werner’ lava lake), v) the background temperature itself in the case that pixel saturation occurs, vi) meteorological effects; of which air temperature, relative humidity and wind speed might have an important control on the development of fumes, and vii) the viewing geometry; which is dependent on the nadir angle of the sensor at the time of acquisition (i.e. nadir varies between  $\pm 8.6$  in both data sets), the position of the anomaly within the swath and the topography of the target area.

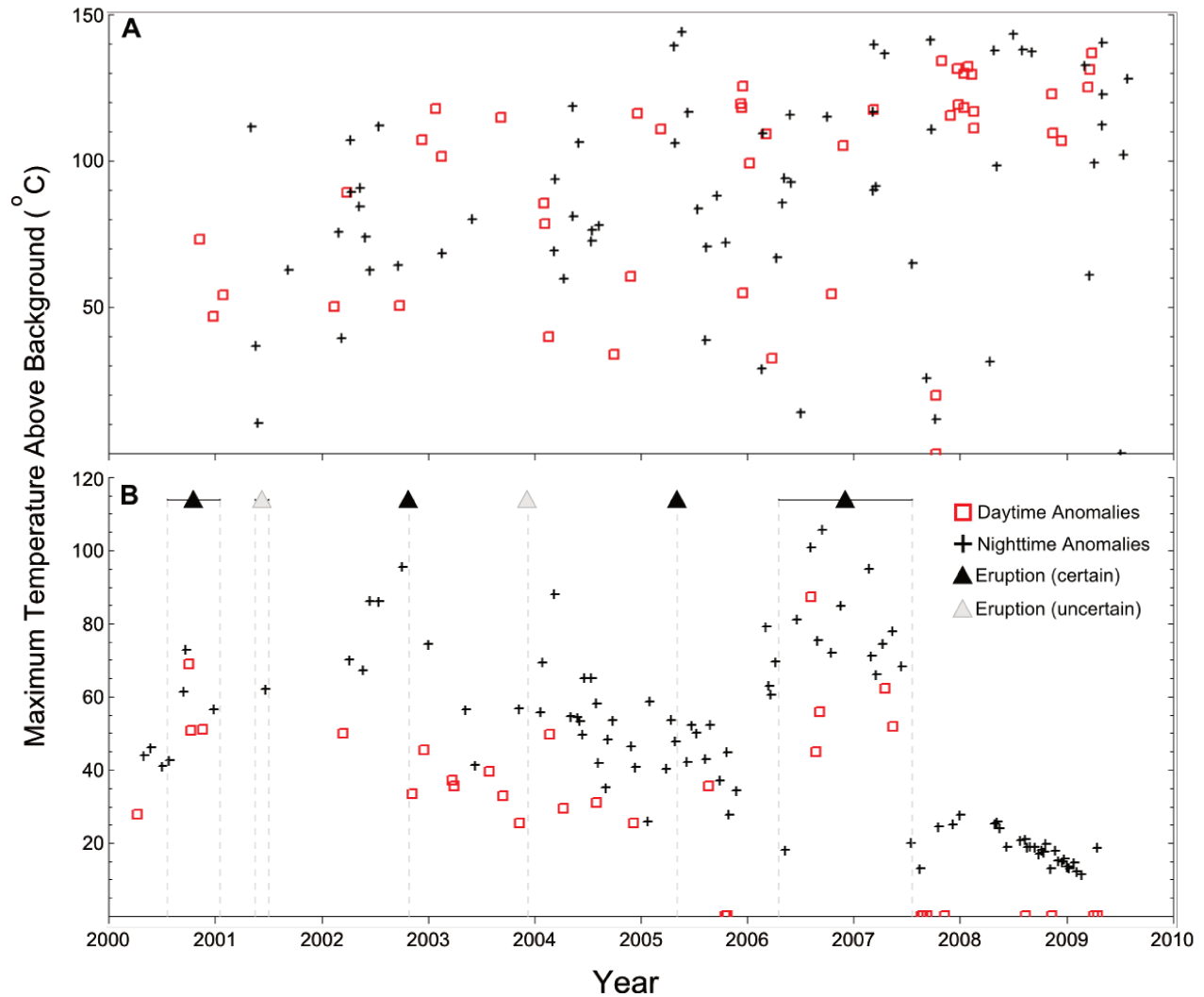


**Figure 3.10.** Maximum temperatures above background for a) Erebus and b) Láscar. Red squares and black crosses denote daytime and nighttime images, respectively. The midpoint of eruptive episodes is denoted using a triangle symbol.

The maximum temperature series at Láscaar displays a significant contrast in style. Temporal trends are discernible and appear associated with eruptive events. These trends include a) two eruptive precursors, namely i) a gradual increase before the 2002 eruption and ii) a gradual decrease followed by an increase before the 2006 eruption, b) syn-eruptive increases during the 2000 and 2006 eruptions as well as c) post-eruptive changes, with a brief increase after the 2003 eruption and sustained decrease after the 2006 eruption.

The onset of the first eruption in the Láscaar time series occurs within 7 months of the launch of the ASTER sensor. Trends preceding this eruption are therefore unclear. However maximum temperatures are higher during the eruptive episode relative to pre-eruptive values. Few data were available for 2001, with only one suitable cloud-free scene available for that year. We thus have no data bearing on the eruptive episode reported to have occurred between 4<sup>th</sup> May and 6<sup>th</sup> July 2001 (Venzke et al. 2002 -).

The October 2002 eruptive episode consisted of several small explosions that produced ash plumes ranging in height from 300 to 1500 m above the crater rim (Bulletin of the Global Volcanism Network. Láscaar. 2003). This episode was preceded by a progressive increase in maximum pixel temperatures above background (Fig. 3.10b). Lava dome growth and destruction have been associated with a number of Láscaar's past eruptions but no dome was observed in the active crater throughout 2000 - 2002 (Bulletin of the Global Volcanism Network. Láscaar. 2003). The increase in thermal output apparent from the ASTER time series is therefore likely to represent an increase in the temperature and/or flux of gas emission. Increases in fumarolic activity have also been observed before explosive eruptions at other stratovolcanoes (e.g. July 1985 at Nevado del Ruiz, Colombia [Scientific Event Alert Network. Nevado del Ruiz. 1985], July 1995 at Soufrière Hills, Montserrat [Bulletin of the Global Volcanism Network. Soufrière Hills. 1995], and May 2010 at Bezymianny, Kamchatka [Smithsonian Institute. Bezymianny Weekly Reports. May, 2010]).

Following the October 2002 eruption the active crater collapsed by several tens of meters, producing a deep, steep depression roughly 200 m in diameter and 200 m deep (Bulletin of the Global Volcanism Network. Láscaar. 2003). Fumarolic activity continued after this time and was punctuated by the occurrence of a 400 m high, grey coloured plume in December 2003 (Bulletin of the Global Volcanism Network. Láscaar. 2004). No thermal precursors are apparent before this eruption. The brief peak in maximum temperatures after the event perhaps indicates that a

temporary, post-eruptive increase in fumarolic activity occurred. Such an increase could be the result of decompression of magma remaining in the upper conduit following the expulsion of magma during the eruption, facilitating both the exsolution and transport of volatiles to the surface. Alternatively it may indicate that an active lava dome was exposed at the surface at that time.

Local residents (15–60 km from the volcano) did not report any earthquakes or explosions in relation to a Vulcanian eruption of May 2005. Nor do we observe any significant changes in maximum temperatures above background before, during or after this event. Nevertheless, an ash cloud was observed in AVHRR imagery and very fine ash fall was also reported in Salta (Argentina) ~285 km SSE (Bulletin of the Global Volcanism Network. Láscaar. 2005).

Field observations of the active crater in December 2005 (i.e. after the May 2005 eruption) revealed that the crater floor was no longer visible from the accessible (i.e. Southern) side of the crater rim, indicating that further subsidence had occurred (Bulletin of the Global Volcanism Network. Láscaar. 2006). Maximum temperatures show a gradual decrease throughout this time (i.e. from May to December 2005) and may be related to crater collapse and an overall reduction in permeability in the upper conduit. Mechanisms for such permeability reduction include: i) bubble collapse of a foamy lava, ii) precipitation of hydrothermal minerals, iii) welding and fusion of the conduit walls, and iv) increases in the dynamic viscosity and strength of magma by cooling, degassing and crystallization (Matthews et al. 1997). This trend is analogous to the behaviour described for the 1993 eruptive style (Oppenheimer et al. 1993b), at which time decreases in conduit permeability and therefore fumarolic activity (as inferred from decreases in radiant flux measured by Landsat infrared bands) were shown to precede eruptive events. We note that it is possible that the collapse of the crater may also act to obscure some of the radiance emitted by the volcano from reaching the sensor in off-nadir scenes.

Here we also observe, for the first time, an increase in maximum temperatures (i.e. ~January to April 2006) following a gradual decrease as described above. It is not clear whether this represents a sudden increase in permeability, the emplacement of a lava dome or perhaps even an unreported eruption. Maximum temperatures above background remain elevated throughout the April 2006 - July 2007 eruptive period. This could reflect a period of elevated strong fumarolic activity or possibly effusion of a lava dome. No lava dome was observed during fieldwork at the active crater carried out by one of us (S. Murphy) on 10 December 2009

(Fig. 3.11), though the crater floor was still not visible from the Southern rim of the volcano at that time.



**Figure 3.11. The collapsed active crater of Láscar volcano as seen from the Southern rim on the 10<sup>th</sup> December 2009. A lava dome is not visible, however, neither is the crater floor due to local topographic relief.**

After this final eruptive period (i.e. July 2007 onwards) maximum temperatures above background remained consistently low, with anomalies only being detected at night. A small increase in these maximum temperatures can be seen throughout the remainder of 2007. Following this a gradual decrease in maximum temperatures is observed until the end of the time series (i.e. 18<sup>th</sup> April 2009). We infer that fumarolic intensity was relatively low at this time, perhaps reflecting waning degassing of residual magma in the conduit.

### 3.6.2. The spatial extent of thermal anomalies

The spatial extents of thermally anomalous regions for both a) Erebus and b) Láscar are displayed in Figure 3.12. A separate scatter plot is used to display the size of i) low, ii) moderate and iii) high temperature anomalies, as well as iv) SWIR anomalies. Note the distinction between daytime and nighttime scenes.

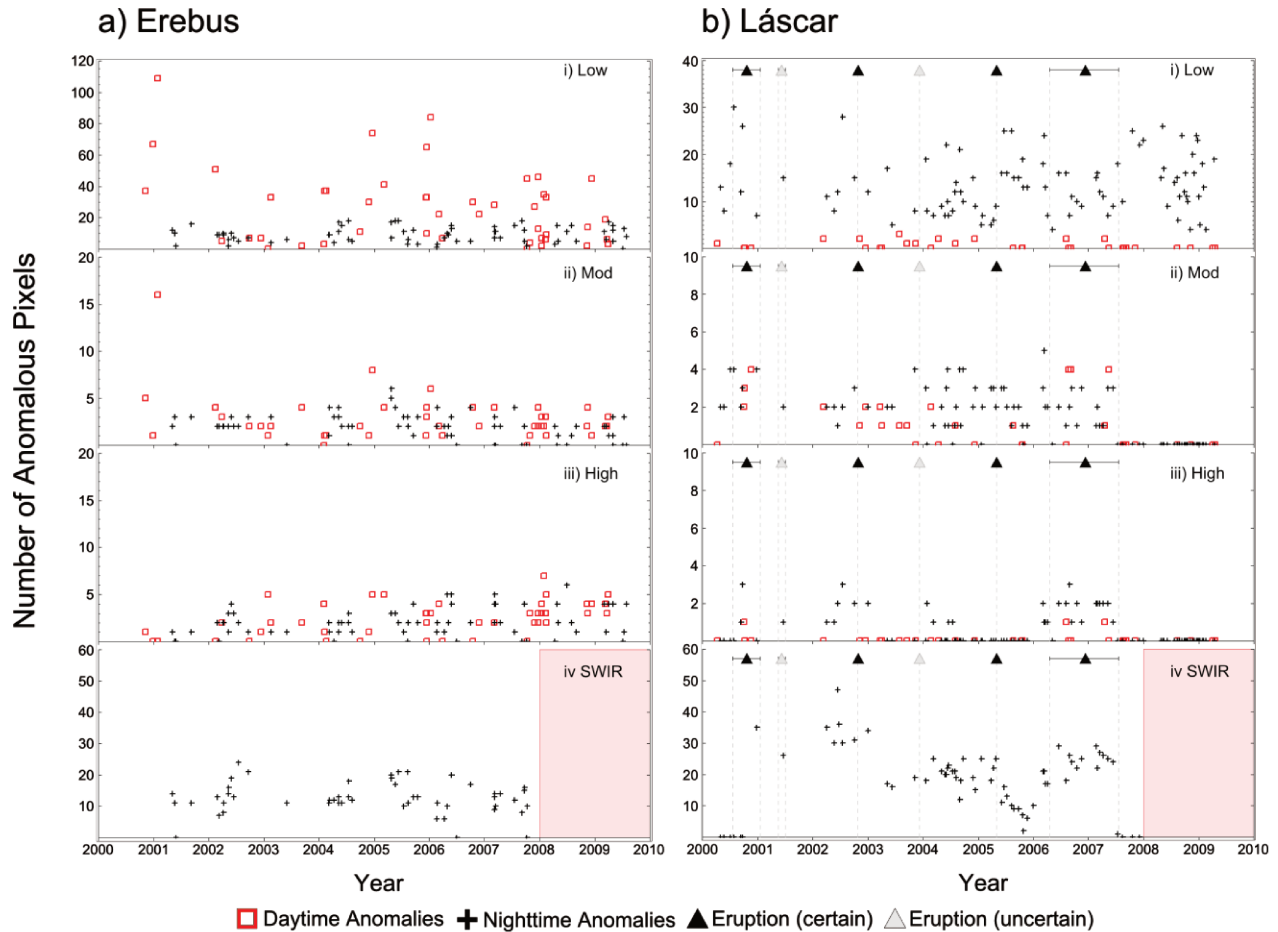


**Figure 3.12. The size of thermal anomalies at a) Erebus and b) Láscar volcano. Distinction is made between i) low, ii) moderate and iii) high temperature anomalies, as well as iv) a SWIR anomaly series (interrupted in 2008 due to the ASTERSWIR system failure). Note that temperature and SWIR pixel sizes are not the same (i.e. 90 and 30 m, respectively). Red squares and black crosses denote daytime and nighttime images, respectively.**

### 3.6.2.1. Erebus

Low temperature anomalies at Erebus (Fig. 3.12a i) display a strong dependence on solar irradiation with peaks occurring during daylight hours. Comparison with VNIR scenes indicates that these low temperature anomalies often coincide with bare rock around the Erebus crater and to Sun facing rocks beyond the caldera edge. Ideally the background area would represent all the inactive surfaces in the target area (i.e. both snow and rock in this case). However, simply incorporating the exposed rocks around the crater rim into the background area is likely to produce unreliable background temperatures given that fumarolic activity up the inner crater walls and/or the presence of plumes can thermally contaminate such proximal regions. We do not attempt to fine tune the background selection methodology here but rather emphasize the caution required in interpretation of thermal anomalies and the value of comparing the anomaly maps with the original reflectance datasets.

While the low temperature anomaly class is stable at night, the size of moderate and high temperature anomalies (Fig. 3.12a ii and iii) is stable regardless of the solar elevation angle. A notably large moderate temperature anomaly occurs on 27<sup>th</sup> January 2001. The image acquired at this time includes the full suite of ASTER sensor bands (Fig. 3.13) in which a) a thick plume, ~500m in diameter, is visible in the VNIR, b) a second thermal feature, probably Werner's fumarole, is discernible in the SWIR bands, and c) a fairly large (i.e. 16 pixel) moderate temperature anomaly and a wide-spread, low temperature anomaly are present; the former appears to be associated with the plume and the latter to exposed rock surfaces.

The SWIR anomalies, as a whole, support evidence for a consistent high temperature source. The size of these anomalies typically vary around 10 - 20 SWIR pixels, i.e. 9000 - 18,000 m<sup>2</sup> (Fig. 3.12a iv). This is larger than the known area of the lava lake by a factor of ~10 and likely results from the disparity between the lava lake signal and the immediate crater surroundings. To illustrate this point, imagine an isothermal lava crust at 500 °C and a surrounding area at 0 °C. If both radiate as blackbodies then the crust will emit  $3.4 \times 10^2 \text{ W m}^{-2} \text{ sr}^{-1} \mu\text{m}^{-1}$  of spectral radiance at 2  $\mu\text{m}$  while the ground would emit only  $1.4 \times 10^{-5} \text{ W m}^{-2} \text{ sr}^{-1} \mu\text{m}^{-1}$  at this wavelength, i.e. a difference of seven orders of magnitude. Scattering (enhanced by the gas and aerosol plume) of just a small fraction (e.g. 1%) of the lava lake radiation into the instantaneous field of view (IFOV) of adjacent detector elements would increase the size of the

anomaly such that it does not accurately map to the feature's true dimensions. Another factor that blurs SWIR anomalies is the relationship between the IFOV and detector resampling frequency. Pixels do not map perfectly to areas on the ground from which the radiation was sensed but rather correspond to upwelling radiation received from a wider solid angle defined by the detector's point spread function. Furthermore it is also possible that some hysteresis effects occur as the sensor scans over very hot targets. These factors combine to significantly smear out of the signal of high temperature features such as lava lakes. They may also contribute to increasing the variability in the size of SWIR anomalies through time. Other factors that may increase this variability include those mentioned previously as influences on maximum pixel temperatures (Section 5.1) as well as intermittent activity at Werner's fumarole (which is occasionally incandescent and which was also the site of an ephemeral lava lake in December 2004).

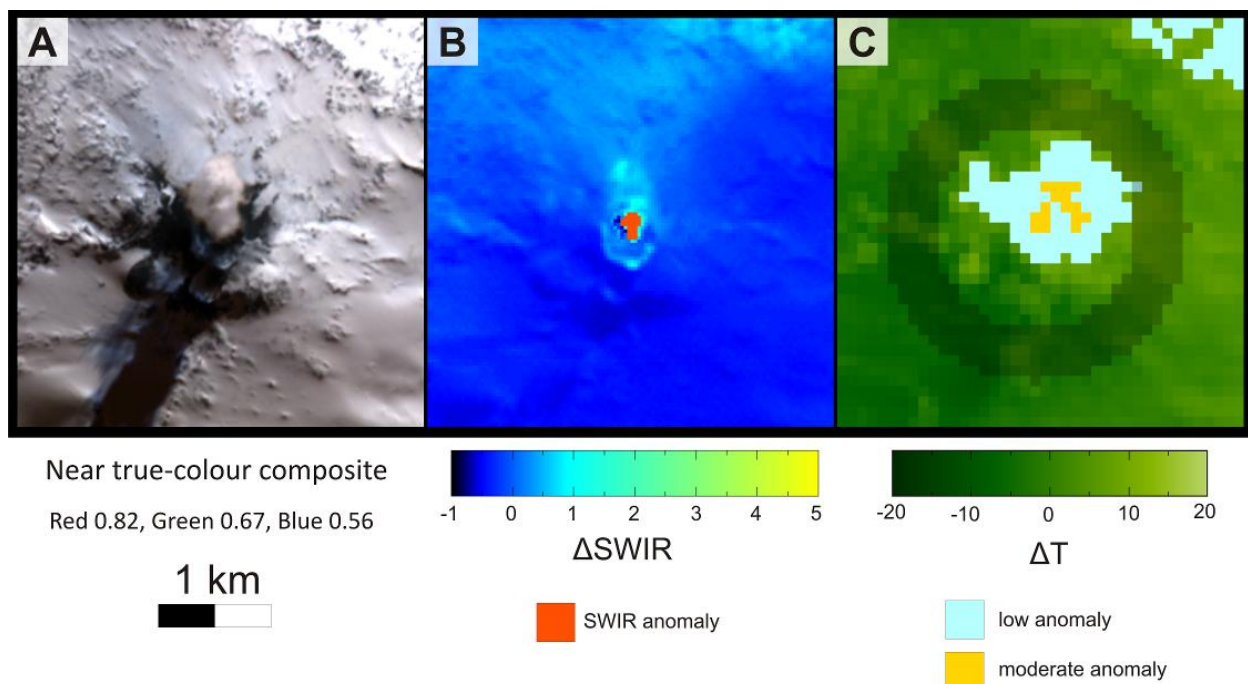


**Figure 3.13. A vaporous plume, emanating from Erebus on the 27th January 2001 at 20:25 [UTC], is visible in a) VNIR, while associated thermal anomalies are present in b) SWIR and c) temperature images. The background area is highlighted in c) as a dark ring. All images are to the same scale and North is up.**

### 3.6.2.2. Lásca

There is an increase in the size of low, moderate and high temperature anomalies during the first eruptive episode of the Lásca time series (i.e. 20<sup>th</sup> June 2000 to 18<sup>th</sup> January 2001), as was also observed in the intensity of the maximum temperature series. A SWIR anomaly is only detected toward the end of this period and at 35 pixels in size, it is one of the largest in this data set. As mentioned previously no dome was observed in the active crater at this time (Bulletin of the Global Volcanism Network. Lásca. 2003), which may indicate that this large SWIR anomaly is due to high temperature fumaroles. There may be a suggestion of a precursory increase in low and moderate temperature anomalies before this eruptive period. Again it is difficult to confirm such a hypothesis given the limited time span between the start of ASTERs operational life and the onset of this eruption.

Low, high and, to a lesser extent, moderate anomalies show a progressive increase before the third eruptive period (9<sup>th</sup> October 2002). This is analogous to the behaviour of maximum pixel temperatures and indicates that the size and maximum temperature of thermal anomalies were correlated at this time. The thermal distribution of anomalies suggests that fumarolic intensity was increasing over this time period, i.e. extensive, low temperature anomaly with an irregular, dynamic shape and a central warmer region that increases in both size and intensity (Fig. 3.14). SWIR anomalies were relatively extensive and stable in size (Fig. 3.12b iv) which is consistent with an increase in the flux and/or temperature of emissions from existing fumaroles, as opposed to any significant expansion of the fumarole field.

Low and moderate temperature anomalies display a subtle gradual decrease followed by a sudden increase shortly before the eruption on 11<sup>th</sup> December 2003. This is perhaps analogous to the behaviour of maximum temperatures before the 2006 eruption (Fig. 3.10b) as well as pre-1993 cycles (Matthews et al. 1997) which have been described above, and may therefore represent a subtle thermal precursor. No high temperature anomalies are recorded at the time and a lack of nighttime scenes precludes the search for a similar pattern in the SWIR time series.

Four separate scenes contain high temperature anomalies within the 6 month period following the December 2003 eruption. This may reflect a post-eruptive increase in fumarolic activity, as was also inferred from the maximum temperature series. Low temperature anomalies show a general decrease in size from around October 2004 until the 4<sup>th</sup> May 2005 eruption

ensues. This contraction may pertain to minor permeability decreases in the upper conduit and could be another example of a subtle thermal precursor. There was no apparent change in the size of moderate, high or SWIR anomalies before this eruption. Again this supports the hypothesis that the source of the eruption was fairly shallow and that the relationship between fluid overpressure and the mechanical strength of containing rock in the upper conduit was already somewhat critical.

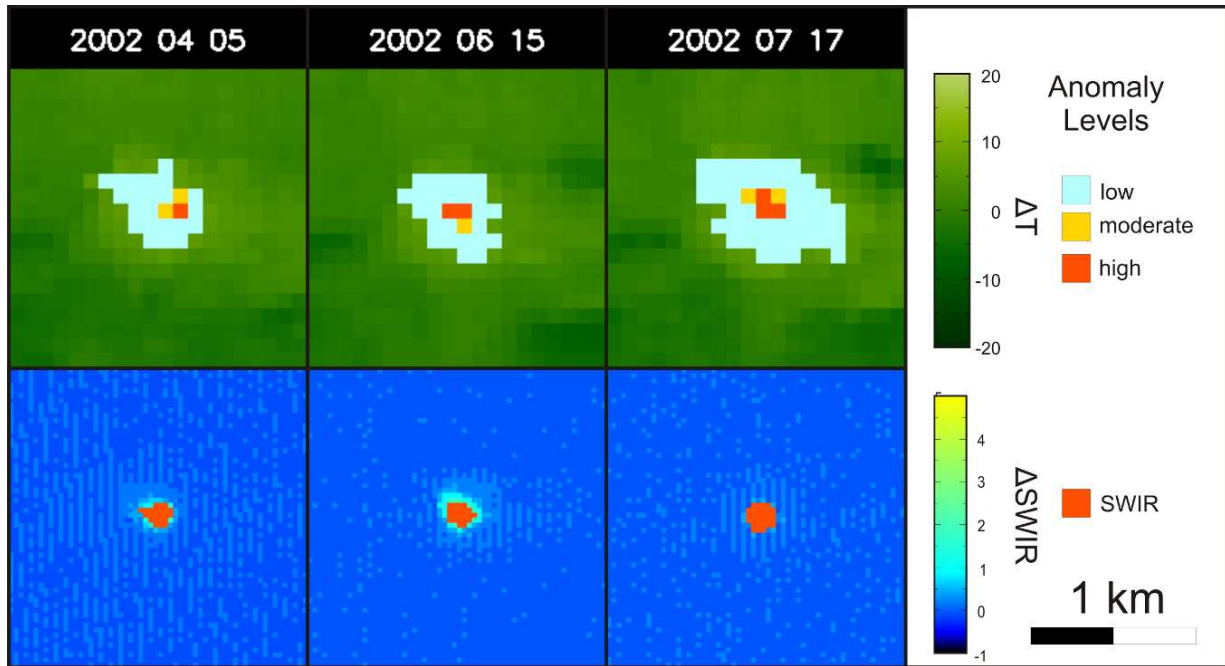


**Figure 3.14. Increase in the size of low and high temperature anomalies and a consistently large SWIR anomaly precede an eruption of Láscair on 9th October 2002 eruption. All images are to the same scale and North is up.**

The low temperature anomaly series shows a distinct increase immediately after the penultimate eruptive episode (i.e. 4<sup>th</sup> May 2005) and remains elevated up until the beginning of the last eruptive period on 3<sup>rd</sup> April 2006. Conversely the moderate and SWIR anomalies display a similar pattern to that described for the maximum temperature series, i.e. a gradual decrease followed by an increase before eruption (Fig. 3.15). The onset of this increase occurs somewhere between 2 and 4 months before the start of the subsequent eruptive episode and is even accompanied by some high temperature anomalies. We suggest that degassing was an important component of these anomalies given the extension and spatial configuration of the

contemporaneous low temperature anomalies and since no lava dome was observed during field investigations carried out at the time (Bulletin of the Global Volcanism Network. Lásçar. 2006).

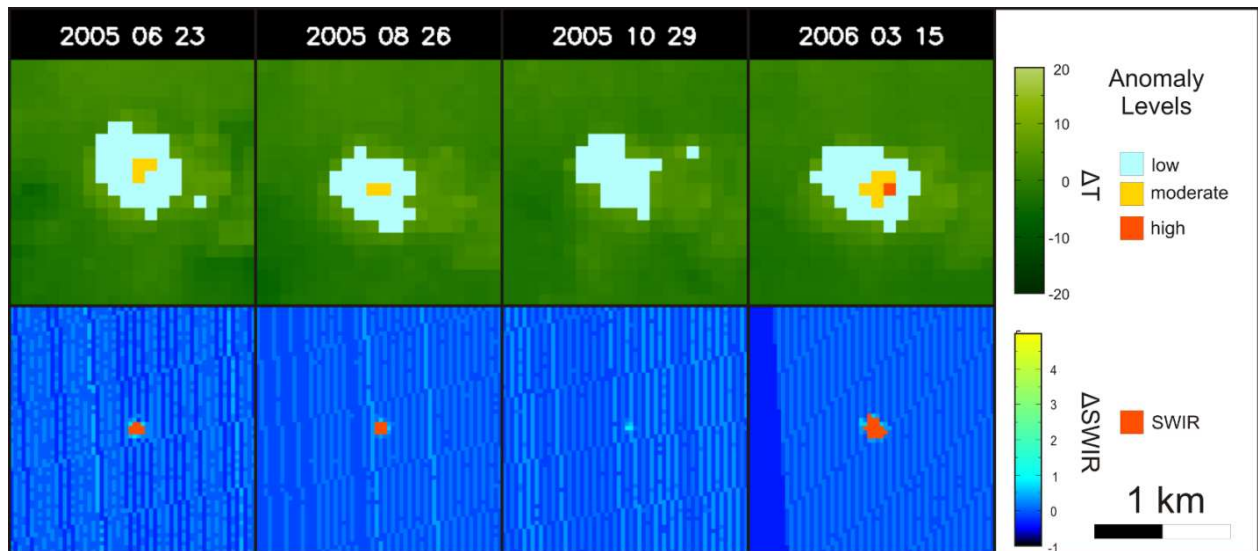


**Figure 3.15. A gradual decrease followed by an increase in the size and intensity of thermal anomalies precedes a surprisingly intense and long lasting eruptive period at Lásçar. All images are to the same scale and North is up.**

The final eruptive period (April 2006 - July 2007) is characterized by consistent high temperature and SWIR anomalies that are confined to the centre of the active crater. It is possible that lava was emplaced at this time although, as mentioned previously, field investigation did not reveal the presence of a dome. Alternatively a high temperature fumarole field may have developed on the crater floor. This is consistent with contemporaneous chemical and isotopic analyses of gas emissions from Lásçar, which show that fumaroles within the active crater have a stronger magmatic signature (i.e. high  $\text{SO}_2$ , HCL and HF) than fumaroles that are situated on the crater rim (Tassi et al. 2009). Efficient degassing of the upper conduit appears to have been sustained throughout the eruptive period. An abrupt end to moderate, high and SWIR anomalies coincide with the end of the final eruptive period. We note that low temperature anomalies remain quite large in size for approximately 6 months after this eruptive period, suggestive of dispersed fumarolic activity. The remainder of the data set displays considerable variability in the size of low temperature anomalies. This may suggest that Lásçar had entered a low level, intermittent degassing regime.

### 3.7 Discussion

The maximum temperature above background and the size of anomalous areas are both measures that can provide insight into dynamic volcanic behaviour and therefore be useful in a monitoring context. The maximum pixel temperature however can be less meaningful for sub-pixel-sized lava bodies. Several factors that may cause the resultant scattered response have been discussed above. Here we briefly explore the dependence of the maximum pixel temperatures on the maximum fraction of the lava lake in a given pixel. We then go on to comment on the size and intensity of thermal anomalies and their potential monitoring value at other volcanoes.

#### 3.7.1. Scatter in maximum $\Delta T$ at Erebus

The spectral radiance,  $L_{(\lambda,T)}$ , emitted by a surface is described by the Planck function:

$$L_{(\lambda,T)} = \epsilon_{\lambda} c_1 \lambda^{-5} / \left[ \exp\left(\frac{c_2}{\lambda T}\right) - 1 \right] \quad (3.6)$$

at wavelength  $\lambda$  and thermodynamic temperature  $T$ , and where  $\epsilon_{\lambda}$  is spectral emissivity, and  $c_1$  and  $c_2$  are the radiation constants (i.e.  $c_1 = 2\pi hc = 3.742 \times 10^{-16} \text{ W m}^2$  and  $c_2 = hc/k = 1.439 \times 10^{-2} \text{ m K}$ ; where  $h$  is the Planck constant,  $c$  the speed of light and  $k$  the Boltzmann constant). Assuming the spectral radiance and emissivity are known, the temperature of a remote surface can be estimated by rearranging:

$$T_{(\lambda,L)} = c_2 / \lambda \ln \left( \frac{\epsilon_{\lambda} c_1 \lambda^{-5}}{L} + 1 \right) \quad (3.7)$$

As the emissivity of our target area was not known we assumed a maximum of 0.97 and then applied the Normalized Emissivity Method (Realmuto, 1990) for temperature retrieval with equation 3.7. In practice, the resultant pixel-integrated temperature is weighted according to the bandpass function of the sensor and the Planck radiation distribution of the target. As the radiation emitted from a surface is non-linearly dependent on temperature (i.e. Eq. 6) any temperature retrieval will tend to diverge from the average temperature of subpixel thermal

components unless the target surface is isothermal. The magnitude of this divergence is usually small for typical terrestrial surfaces as targets tend to have limited sub-pixel thermal contrast and low temperatures (i.e. < 100 °C; Garratt, 1992). However, it can be large in the presence of a high temperature feature with strong spatial variability (such as a fissured active lava surface).

To illustrate the effect that Erebus lava lake might have on a maximum pixel temperature we model the active crater as a three component, blackbody system made up of a crust of lava at 500 °C which can have incandescent cracks at 900 °C (Calkins et al. 2008) and is surrounded by ground at -30°C. The lake can range in size from 700 to 1400 m<sup>2</sup>, the maximum fractional area of the lake within any given ASTER TIR pixel can therefore range between 2.2 and 17.3 %. The lower fractional limit is calculated by assuming that the smallest possible lake area can be equally divided between four pixels. The upper limit represents the situation in which the largest lake area is completely imaged within a single pixel. The maximum proportion of incandescent cracks within the lake is set as 0.1. This is because the maximum reported area of bubble burst (i.e. 60 m<sup>2</sup>; Calkins et al. 2008) would occupy 8.6 % of the smallest modelled lake size. The average temperature of a 3 component thermal system is given by

$$T_{average} = f_h T_h + f_c T_c + f_b T_b \quad (3.8)$$

where *f* is the fractional area of a component at temperature *T*, and the subscripts *h*, *c* and *b* denote hot incandescent cracks, lava crust and non-active background, respectively. The measured pixel temperature (i.e. equation 3.7), on the other hand, depends on the sum of the individual radiance components (i.e. equation 3.9), which is not linearly related to temperature and will therefore result in divergence between the measured and average temperature.

$$L_{total} = f_h L_{(\lambda, T_h)} + f_c L_{(\lambda, T_c)} + f_b L_{(\lambda, T_b)} \quad (3.9)$$

where *L<sub>total</sub>* is the total spectral radiance measured by a single detector element whose waveband has a mid-point at *λ*, and *L* is the blackbody radiance emitted by isothermal components at temperatures *T<sub>h</sub>*, *T<sub>c</sub>* and *T<sub>b</sub>*. The maximum pixel temperature within a given scene will therefore not only depend on the physical properties of the target area but also on the maximum fractional area of the lava lake within an IFOV of a given detector element of a sensor array.

Absorption of volcanic gas species (e.g.  $\text{H}_2\text{O}$  and  $\text{SO}_2$ ) is not modelled here as it will have limited affect on temperatures calculated using the Normalized Emissivity Method. This is because the NEM algorithm automatically selects the band which has the largest brightness temperature and is therefore likely to avoid bands that have undergone significant amounts of wavelength dependent absorption. Field measurements have shown however that transmission across the TIR waveband (i.e. 7 - 13  $\mu\text{m}$ ) is strongly attenuated by volcanic aerosols (Sawyer and Burton, 2006). This will affect temperature estimates as even the largest brightness temperatures will have been significantly reduced. We therefore model the dependence of pixel temperatures on the presence of aerosols as well, considering the case in which either a) no aerosols are present or b) aerosols cause a 30 % reduction in transmittance across all wavelengths (Fig. 3.16).

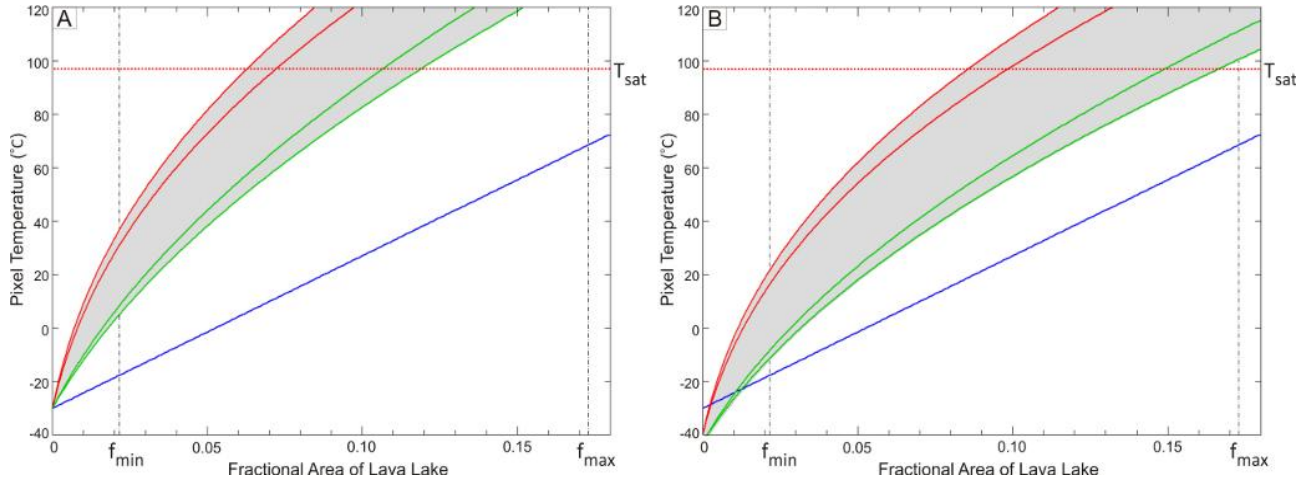


**Figure 3.16. Pixel temperature solutions (grey areas) for ASTER TIR bands as a function of the fractional area of a lava lake within a given pixel. The average temperature of sub-pixel components is given (solid blue lines). Aerosols can be either a) not present or b) cause a 30% reduction in transmittance. The maximum fractional area of the lake can range from 0.022 to 0.173 (vertical dashed lines). Temperature ranges from ASTER bands 10 and 14 are plotted as pairs of red and green lines respectively and denote response ranges for the cases in which incandescent material occupies zero or 0.1 of the lake. The saturation temperature of an ASTER TIR pixel,  $T_{\text{sat}}$ , is given as a horizontal red dotted line.**

The pixel temperature solutions (grey areas) are sensitive to the fractional area of the lava lake and can exceed the actual temperature (blue lines) by several tens of degrees. Significant scatter in maximum temperatures could therefore be produced by small (i.e. sub-pixel sized)

variations in: lake size, spatial alignment between the target and pixel IFOVs, and the proportion of incandescent cracks within the lake. Aerosols can significantly reduce temperature solutions (Fig. 3.16b) and will act to provide further variability in maximum pixel temperatures.

### 3.7.2. Background temperatures at other volcanoes

The global distribution of volcanoes and their varying topographies and compositions can lead to markedly different background temperatures from one edifice to the next. A standardized method for measuring background temperatures would facilitate comparisons between volcanoes situated around the world. We attempt to make steps toward such a standardized approach by defining a background area that is situated as close to the region of activity as possible without becoming volcanically heated and while also meeting a minimum size constraint. For Erebus and Láscar volcanoes a ring shaped background area was found to be suitable because activity is restricted to a single crater. However, different styles of volcanism (e.g. those with fissural morphologies, such as Erta 'Ale and Eyjafjallajökull) may require different background geometries (e.g. an ellipse).

To isolate a volcanic thermal signal it is necessary to estimate the background value. Furthermore, automatic anomaly detection requires that the natural variability in the background value is quantified. These can both be achieved in a straightforward, unbiased manner through the use of arithmetic averages and standard deviation. However, such background statistics could be compromised in the case that hot volcanic material (e.g. lava and/or pyroclastic flows) fall in the background area. For global monitoring applications it would therefore be necessary to screen automatically for anomalous pixels in the background area. This could be achieved through the use of in-scene statistics or expected background values as derived from time series analysis. It will probably be necessary to remove only the more extreme anomalies from the background area as subtle anomalies are unlikely to affect background statistics significantly. This is because hot volcanic products, such as lava and pyroclastic flows, tend to be channelized and narrow in size close to their source region. As such they will occupy very small proportions of a background area that encircles the entire source region.

### 3.7.3. Monitoring implications

Two clear thermal precursors and two subtle thermal precursors were identified in the Láscaar time series. The well-defined precursors are i) an increase in the size of low, moderate and high temperature anomalies as well as consistently large SWIR anomalies for the 6 - 9 months preceding the 9<sup>th</sup> October 2002 eruptive episode, and ii) a gradual decrease, followed by an increase, in the size of moderate temperature anomalies which is accompanied by high temperature anomalies for roughly 3 months preceding the final eruptive period (i.e. start date 3<sup>rd</sup> April 2006). The subtle thermal anomalies consisted of i) a gradual decrease followed by a sudden increase in the size of low and moderate temperature anomalies before the 11th December 2003 eruptive episode, and ii) a gradual decrease in low temperature anomalies over an ~6 month period preceding the 4<sup>th</sup> May 2005 eruption. Monitoring efforts at Láscaar could thus be usefully augmented by systematic spaceborne remote sensing in the future, especially given that the thermal precursors span timescales of a few months and therefore could have predictive value.

We envisage that measuring the size and intensity of thermal anomalies will provide useful constraints for volcano monitoring teams in general. For example, the detection of a large, hot body would suggest significant activity has recently occurred and may indicate the presence of a lava flow or fresh pyroclastic material. The distinction between plumes and lava flows may also be facilitated by the joint measurement of spatial and thermal information. Plumes will tend to be relatively low in temperature, extensive, irregular shaped, dynamic regions while lava flows will tend to display higher temperatures and more consistent boundaries through time which have either point (i.e. dome) or lobate (i.e. flow) geometries. Such distinction, however, will often be inconclusive for sub-pixel sized bodies as no spatial information is available and strong thermal heterogeneities can lead to unreliable pixel temperatures at this spectral resolution. Significant post-eruptive changes in the size and or intensity of thermal anomalies can help to identify the end of an eruptive episode. This is important because the duration of an eruptive episode has been shown to be statistically related to both the repose time as well as the size of the next eruption (Marzocchi and Zaccarelli, 2006).

### **3.8. Conclusion**

The spatial extent of anomalously hot pixels was introduced as a monitoring parameter for active volcanoes. Comparisons were made to short-wave infrared anomalies as well as to a previously reported thermal metric (i.e. the maximum temperature above background). We show that the size of anomalous regions better correlates to eruptive activity than maximum temperature alone. Measuring the size and intensity of thermal features can be used to improve our understanding of volcanic systems by direct observation, as in this study, or through incorporation into probabilistic or physical models. Future algorithms for volcanic activity detection may include a search for thermal anomalies which exceed a certain size and/or intensity. We note that such observations are only possible because of ASTER's combined spatial and spectral resolution. Even so, future studies would benefit from a new generation of orbital, infrared sensors with improved spatial resolution, such as NASA's proposed HypsIRI mission (Chien et al. 2009). Pixel saturation issues could also be mitigated by extending the dynamic range of detector elements.

# Chapter 4

## MODIS and ASTER Synergy for Characterizing Thermal Volcanic Activity

---

S. W. Murphy, R. Wright, C. Oppenheimer , C.R. de Souza Filho

Published in Remote Sensing of Environment, 131, 195-205, 2013.

### 4.1. Abstract

Volcanic activity is diverse in its manifestations and spans wide temporal and spatial scales. Monitoring volcanoes with any single sensor system can only provide a limited perspective on the nature of such activity because of trade-offs between spatial, temporal and spectral resolution. Spaceborne observations of volcanoes are thus optimised by utilising data from different and complementary remote sensing instruments. This study examines the combined use of the Moderate Resolution Imaging Spectroradiometer (MODIS) and the Advanced Spaceborne Thermal Emission and Reflection Radiometer (ASTER) for analyzing thermal anomalies from four separate volcanoes: Erta 'Ale (Ethiopia), Kīlauea (Hawai'i), Láscaar (Chile) and Kliuchevskoi (Russia). MODIS provides a high temporal resolution (daily) but low spatial resolution (~ 1 km) dataset and is used to measure volcanic thermal radiance. ASTER provides relatively high spatial resolution (~ 90 m) image data and is used to define the size of thermal features, albeit at a poorer

temporal frequency. Erta 'Ale and Kīlauea have been erupting continuously over the 11-year study period and their thermal emission signatures reveal a persistent baseline on which occasional increases in thermal output, associated with more profuse effusions of lava, are superimposed. Kliuchevskoi also displays occasional peaks in thermal activity due to the eruption of lava however intervening periods are characterized by weak or absent thermal anomalies. Láscaar, on the other hand, provides an example of volcanic activity that is difficult for MODIS-type sensors to detect. It is characterized by fumarolic activity that is too low in temperature and too spatially limited to be readily detectable with its coarser instantaneous field of view (i.e., pixel size). However, high resolution data from ASTER can be used to supplement and complement the MODIS dataset. Beyond characterizing the size of thermally anomalies ASTER can also provide constraints on their shape, location and orientation and is capable of detecting relatively subtle thermal anomalies given its high spatial resolution thermal infrared wavebands. These qualities permitted the identification of a thermal precursor to lava flows at Kliuchevskoi. The precursor, which was associated with a rising lava lake, is characterized as an increase in the size and intensity of ASTER-detected thermal anomalies situated in the active crater. Wavelet analysis of the MODIS dataset was also carried out. This revealed the time scales over which radiant output waxed and waned during individual eruptive episodes as well as the repose time between episodes. Such information might be useful in forecasting the likely duration and onset of future eruptions.

## **4.2. Introduction**

Volcanoes can be hazardous to both people and property yet also provide valuable insights into dynamic processes on Earth. It is necessary to monitor active volcanoes to mitigate the risks that they pose and to improve our understanding of these complex physical systems.

Volcanic activity involves the transfer of mass and heat to the Earth's surface. The surface temperature and emissivity of a physical body determine the amount of energy it radiates at any given wavelength. Planck's law describes this relationship, which is modified to account for spectral emissivity as follows:

$$L(\lambda, T) = \varepsilon_{\lambda} c_1 \lambda^{-5} / [\exp\left(\frac{c_2}{\lambda T}\right) - 1] \quad (4.1)$$

where  $L(\lambda, T)$  is spectral radiance ( $\text{W m}^{-2} \text{sr}^{-1} \mu\text{m}^{-1}$ ) as a function of wavelength ( $\lambda$ ) and kinetic temperature ( $T$ ),  $\varepsilon_{\lambda}$  is spectral emissivity, and  $c_1$  and  $c_2$  are the radiation constants (i.e.,  $c_1 = 2hc^2 = 1.19 \cdot 10^{-16} \text{ W m}^2 \text{sr}^{-1}$  and  $c_2 = hc/k = 1.439 \cdot 10^{-2} \text{ m K}$ ; where  $h$  is the Planck constant,  $c$  the speed of light and  $k$  the Boltzmann constant).

This work explores the use of polar-orbiting satellites for monitoring volcanic thermal radiance from space. The types of sensors used for this purpose can be classified into two broad categories: i) high to moderate spatial resolution (i.e.,  $< 100 \text{ m pixel}^{-1}$ ) but low temporal resolution (i.e.,  $> 10 \text{ day}$ ) imagers, and ii) high temporal (i.e.,  $1 \leq \text{day}$ ) but low spatial resolution (i.e.,  $\geq 1 \text{ km}$ ) imagers. The two categories will be referred to as i) high spatial resolution and ii) high temporal resolution for the remainder of this article. We note that although the meaning of adjectives such as ‘advanced’, ‘high’ and ‘moderate’ change with time as far as capabilities are concerned they have still been used widely to name many of the existing orbital imagers. High spatial resolution systems that have been used to monitor volcanic thermal radiance include: the Thematic Mapper onboard Landsat 4 and 5 (e.g., Francis and Rothery, 1987; Rothery et al., 1988; Glaze et al., 1989; Oppenheimer, 1991), the Optical Sensor on the Japanese Earth Resources Satellite-1 (JERS-1) (e.g., Denniss et al., 1996, Dean et al., 1998), the Enhanced Thematic Mapper Plus on Landsat 7 (e.g., Flynn et al., 2001; Wright et al., 2001; Patrick et al., 2004), the Advanced Land Imager on the Earth Observing-1 mission (e.g., Donegan and Flynn, 2004), and the Advanced Spaceborne Thermal Emission and Reflection Radiometer (ASTER) onboard the Terra satellite (e.g., Vaughan and Hook, 2006; Rose and Ramsey, 2009, Murphy et al., 2011). On the other hand high temporal resolution polar orbiters include: the Advanced Very High Resolution Radiometer (AVHRR) flown on the NOAA satellite series (e.g., Harris et al., 1997, Tramutoli, 1998), and the Moderate Resolution Imaging Spectroradiometer (MODIS) (e.g., Wright et al., 2002; Wright et al., 2004; Kervyn, 2008; Koeppen et al., 2011) onboard both the Terra and Aqua satellites. The temporal and spectral resolution of MODIS, as well as its global coverage and reliable geometric and radiometric calibration, led to its application in the world’s first automated system for global volcano monitoring, i.e., MODVOLC (Wright et al., 2002; Wright et al., 2004).

Volcanic phenomena span a wide range of temporal and spatial scales. It may take years, decades or longer for magma to migrate to the surface, whilst a pyroclastic flow can be emplaced in minutes. A volcanic ash plume can extend over thousands of kilometres yet ejecta are typically metre scale or less. This disparity means that there is no single sensor in existence that is capable of acquiring data over the spatial and temporal scales exhibited by all of Earth's volcanoes. Volcano monitoring efforts therefore need to integrate and interrogate data from networks of sensors. From a volcanologist's perspective an ideal network would include terrestrial, airborne and spaceborne sensors. In practice, since most of Earth's potentially active and active volcanoes are subject to at best only rudimentary ground-based monitoring, orbital sensors are a crucial data source for tracking global volcanism.

The Terra satellite, which carries both the ASTER and a MODIS system, offers an excellent opportunity to explore the potential of combining both high spatial and high temporal resolution datasets for monitoring volcanoes from space (e.g., Vaughan and Hook, 2006, Hirn et al., 2008, Vaughan et al., 2008). The ASTER sensor consists of three separate subsystems in the visible and near-infrared (VNIR), short-wave infrared (SWIR) and thermal infrared (TIR) with respective pixel sizes of 15, 30 and 90 m. The SWIR subsystem ceased to provide useful Earth observation data in 2008 due to a cooler malfunction although the VNIR and TIR instruments continue to operate normally. MODIS has 32 spectral channels in the VNIR, SWIR, mid infrared (MIR) and TIR wavelengths with nominal pixel resolutions ranging from 250, 500 and 1000 m. Temporal resolution for all channels is 24 hours. Multiple simultaneous viewing opportunities are possible as both sensors are carried by the same satellite platform.

The aim of this work is to compare how two different sensor classes report the temporal, spatial and thermal characteristics of a range of target volcanoes. The targets were chosen because they display different eruptive characteristics and would therefore be useful in testing the performance of high temporal resolution (i.e. MODIS class) and high spatial resolution (i.e. ASTER class) sensor systems at cataloguing different styles of volcanic activity. The term "style" here is simplified to mean whether thermal activity is any of the following: low temperature, high temperature, small, large, persistent or not persistent. A decadal time series has been used to give a longer term perspective on this.

### **4.3. Study Areas**

Four different volcanoes have been investigated: i) Kīlauea (Hawai'i), ii) Láscaar (Chile), iii) Erta 'Ale (Ethiopia) and iv) Kliuchevskoi (Kamchatka, Russia). Each site represents a markedly different type of volcanic setting: i) intra-plate 'hot spot' volcanism with frequent effusive basaltic eruptions (Kīlauea), ii) a continental-oceanic subduction zone with persistent degassing, sporadic lava dome growth and intermittent explosions (Láscaar), iii) a continental rift zone with an active lava lake (Erta 'Ale) and iv) a volcanic arc (Kliuchevskoi). These sites were selected for their contrasted settings and eruptive styles, enabling a more thorough evaluation of the capabilities and limitations of each sensor.

### **4.4. Metrics for Volcanic Thermal Activity**

This study was concerned with the characterization of thermally anomalous surfaces. Two metrics that quantify different aspects of such surfaces are defined. The first (MOD\*) uses MODIS data to describe spectral intensity. The second (AST\*) estimates the size of anomalous areas using the ASTER sensor.

#### **4.4.1. MOD\* (High temporal resolution volcanic radiance)**

The MODIS dataset used in this study is comprised of all the available nighttime, calibrated radiance scenes (i.e., MOD021KM) and their corresponding geolocation products (i.e., MOD03) acquired for each volcano by MODIS-Terra since its launch in 1999. These data are available from the Level 1 and Atmosphere Archive and Distribution System (LAADS) maintained by the NASA Goddard Space Flight Center. Over the study period (i.e., 1 January 2000 to 1 January 2012) there are 3709 scenes for Erta 'Ale, 5391 scenes for Kliuchevskoi, 4261 scenes for Kīlauea and 3772 scenes for Láscaar (i.e., a total of 17,133 MOD02 1KM scenes). The combined size of this data set (i.e., 1.7 Tb) was reduced by cropping scenes and selecting pertinent spectral channels.

The MOD\* metric is designed to represent the overall amount of MIR radiance from thermally anomalous areas. Given the IFOV of the MODIS instrument the vast majority of

thermal anomalies will be subpixel in size. A radiance measurement from a single detector element will therefore often contain contributions from volcanically active areas and non-active background areas. We have used channel 21 (i.e., 3.929 - 3.989  $\mu\text{m}$ ) to characterize the radiance from volcanically active areas and channel 32 (i.e., 11.77 - 12.270  $\mu\text{m}$ ) to characterize the radiance from non-active background areas. This is because MIR detector arrays (e.g., channel 21) are much more sensitive to volcanic temperatures (i.e., hundreds of degrees Celsius) than TIR detector arrays (e.g., channel 32). To illustrate this point let us consider an isothermal background surface at 20  $^{\circ}\text{C}$  that occupies the entire IFOV of detector elements in channel 21 and 32; the radiance from each channel will be 0.5 and 8.1  $\text{W m}^{-2} \text{sr}^{-1} \mu\text{m}^{-1}$ , respectively. In the case that the IFOV also contained a second isothermal surface with a temperature of 500  $^{\circ}\text{C}$  and area of 100  $\text{m}^2$  (i.e., 0.01% of MODIS pixel) then the radiance from each channel would be 11.72 and 9.32, respectively. That is, the TIR radiance in channel 32 will increase by 14.8% whilst the MIR radiance in channel 21 will increase by 2232%. The MOD\* metric uses this relationship to define anomalous radiance in channel 21 as follows:

$$MOD^* = \sum_{i=1}^n (L_i - L_{i,bkgd}) \quad (4.2)$$

where  $n$  is the number of anomalous pixels,  $L_i$  is the spectral radiance and  $L_{i,bkgd}$  the background spectral radiance of the  $i^{\text{th}}$  anomalous pixel in channel 21. The background radiance was calculated by using the brightness temperature in channel 32 as a proxy for the temperature of the non-active background areas. This background temperature (i.e., from TIR wavelengths) was then used to calculate background radiance (i.e., in MIR wavelengths) for channel 21. A pixel is considered to be anomalous if its Normalized Thermal Index (i.e., NTI) exceeds a threshold value. The NTI (equation 4.3) utilizes the relative sensitivity of MIR and TIR wavelengths outlined above to detect thermally active volcanic targets from space (Wright et al. 2002).

$$NTI = \frac{L_{22} - L_{32}}{L_{22} + L_{32}} \quad (4.3)$$

where  $L_{22}$  and  $L_{32}$  are spectral radiance measurements from MODIS channels 22 and 32, respectively. MODIS channels 22 and 21 cover the same spectral region but have different saturation limits (i.e., brightness temperatures of around 60 and 225 °C, respectively) and radiometric accuracy (i.e., noise equivalent temperature variation, NE $\Delta$ T, of 0.07 and 2.0 K, respectively). If saturation occurs in channel 22 then radiance from channel 21 was automatically used instead. A global threshold of -0.8 was proposed by Wright et al. (2004) to identify volcanic thermally anomalies from nighttime MODIS scenes. This global threshold was set relatively high to avoid false alarms. To increase anomaly detection sensitivity it is possible to define volcano-specific thresholds (e.g., Kervyn, 2008, Koeppen et al., 2011). To find an optimal local NTI threshold we first calculated the frequency distribution of all NTI values for each volcano (Fig. 4.1).

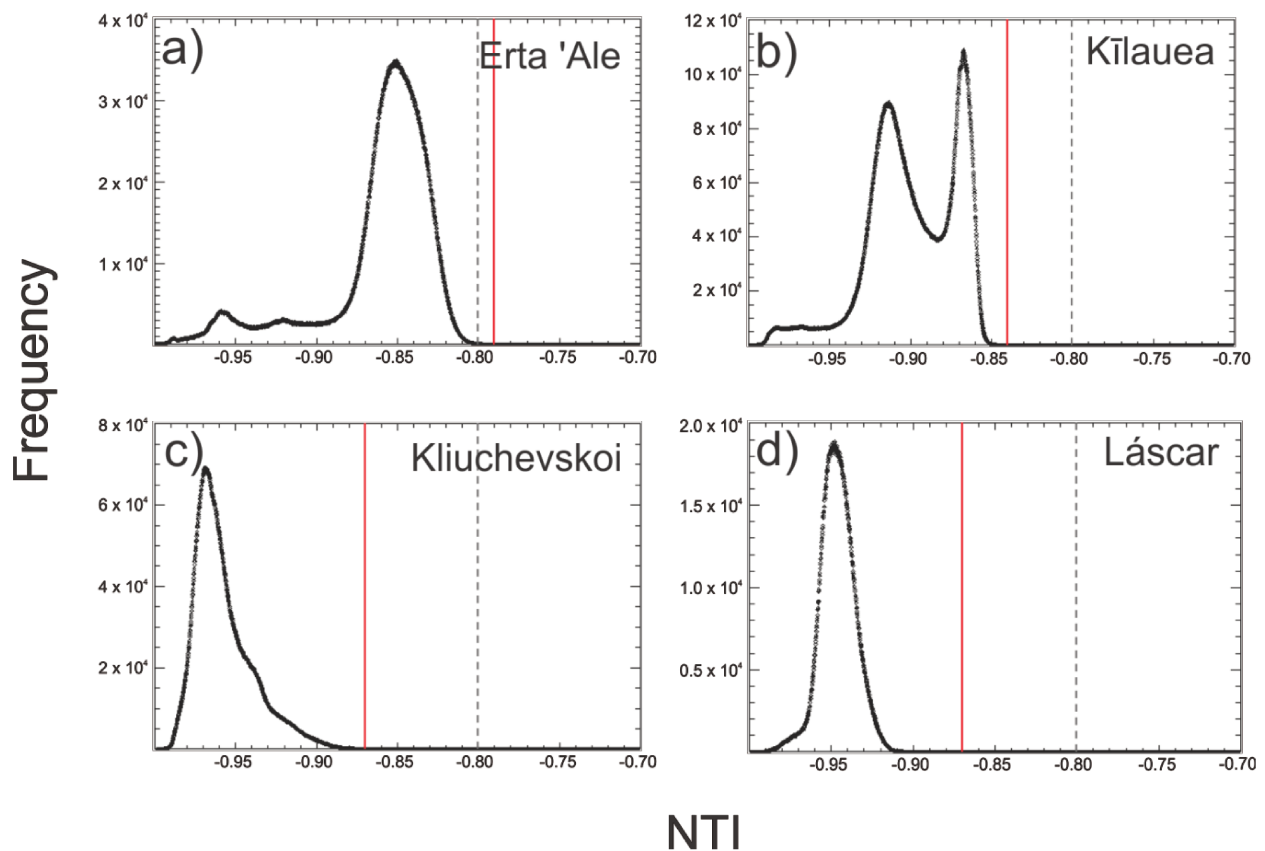


**Figure 4.1.** The frequency distribution of MODIS Normalized Thermal Index (NTI) at a) Erta ‘Ale, b) Kīlauea, c) Kliuchevskoi and d) Láscaar. Optimal local anomaly thresholds are shown using a solid, red line. The global MODVOLC threshold is shown using a dashed, grey line for comparison.

The NTI values that correspond to volcanic hot-spots represent a tiny percentage of pixels at the extreme right hand tail of the distribution, pixels that are not anomalous will correspond almost exclusively to NTI values in the rest of the distribution. An optimal threshold needs to be found to limit the number of false positives and missed anomalies. This was achieved by checking that the spatial distribution of anomalies was reasonable throughout the time series (Fig. 4.2) and that anomalies did not display seasonal variations through time (Fig. 4.3). The bimodality of the Kīlauea histogram (Fig. 4.1b) is due the presence of both land and water in the area used to calculate local NTI values at this volcano. The location of anomalous pixels were recorded on a scene by scene basis and anomaly frequency maps were calculated for each volcano (Fig. 4.2).

These maps depict the frequency with which an anomalous NTI value was detected at a given location over an 11 year period. Zero frequency areas are filled in using MODIS visible wavebands to provide a geographic context. Local NTI histograms (Fig. 4.1) were calculated from the entirety of scenes depicted in Figure 4.2, the MOD\* time series was calculated from smaller areas outlined using a white, dashed box. Figure 4.2a shows that activity at Erta ‘Ale is confined to the summit caldera. The fairly large (i.e., several km<sup>2</sup>) but low frequency region to the NNW is associated with the Alu-Dalaffilla fissure eruption of November 2008. Activity at Kīlauea is more spatially extensive and mainly corresponds with the lavas erupted on the volcano’s East Rift Zone (Fig. 4.2b). Dotted around the Big Island are areas which contained short-lived thermal activity (i.e., low probability areas). They have previously been interpreted as resulting from vegetation fires (Koeppen et al., 2011). This might also be the cause of similar low probability areas surrounding Kliuchevskoi (Fig. 4.2c). Volcanic anomalies can be observed over both Kliuchevskoi and Bezymianny. Láscar’s thermal features are constrained solely to the active summit crater (Fig. 4.2d). Clearly anomaly frequency maps display the likely location of thermally anomalous areas over time, as such, they might be useful during hazard planning exercises. They also help more generally to distinguish effusive activity (i.e., Kīlauea) from lava domes or lakes situated in craters (i.e., Láscar and Erta ‘Ale ). Kliuchevskoi combines both types of behaviour. Thus, even if we knew nothings about these volcanoes beforehand it would be possible from Figure 4.2 to determine that they represent different types of volcanic activity. Annual anomaly frequency maps for each volcano are provided in the supplementary material.

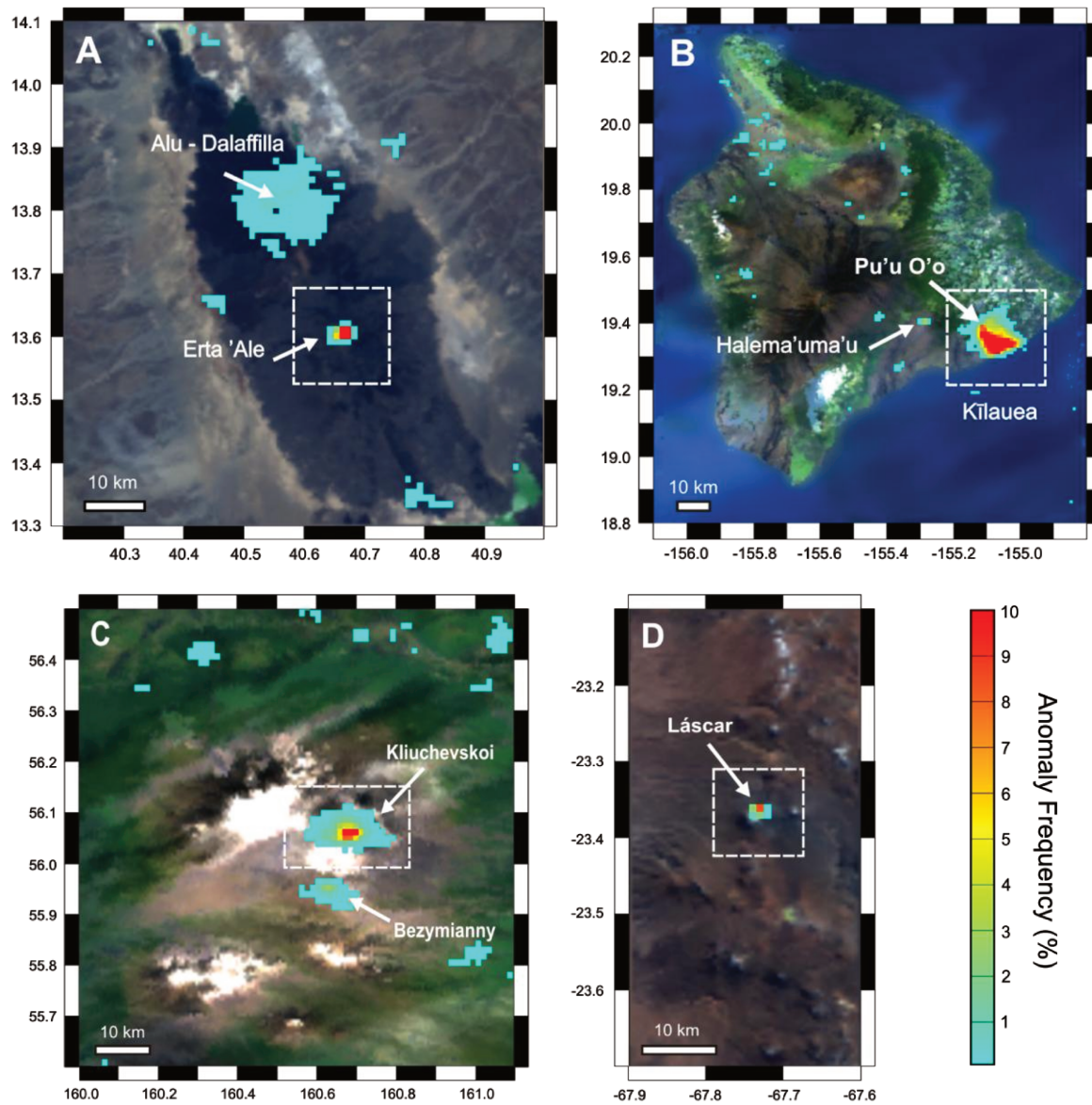


**Figure 4.2. Spatial distribution of anomaly frequency as detected by MODIS between 1st January 2000 to 1st January 2012 at a) Erta 'Ale, c) Kilauea, c) Kliuchevskoi, and d) Láscar.**

#### 4.4.2. AST\* (Size of anomalous areas)

This study uses the ASTER TIR at-surface radiance product (AST\_09T) which is geometrically, radiometrically, and atmospherically corrected by the Land Processes Distributed Active Archive Center (LP DAAC) of the United States Geological Survey (USGS). We obtain terrestrial

surface temperatures from this product using the Normalized Emissivity Method (Realmuto, 1990) with maximum emissivity set to 0.97. The ASTER Surface Kinetic Temperature (AST\_08) product, which is based on the Temperature Emissivity Separation (i.e. TES) algorithm (Gillespie et al. 1998), was not used in this study because we could not verify whether the empirical relationship between laboratory-derived emissivity values and spectral contrast would apply in an active volcanic setting. An inspection for cloud cover was carried out on the temperature image. If clouds completely obscured the volcano so that it could not be located visually in a TIR image then that scene was removed from the dataset.

The AST\* metric utilizes the relatively high spatial resolution of the ASTER sensor to measure the size of thermally anomalous areas.

$$AST^* = A \cdot n^* \quad (4.4)$$

where A is the nominal area of an ASTER pixel (i.e., 8100 m<sup>2</sup>) and n\* is the number of anomalous pixels in a given scene. ASTER pixels were identified as anomalous if their temperature above background exceeded 40 °C. This threshold was selected to ensure an extremely low false alarm rate (i.e., perhaps zero) and to avoid the incorporation of too many ephemeral, low temperature gas plumes. The motivation for filtering cool gas plumes is that they can change dramatically in size on time scales that are orders of magnitude greater than the revisit time of the sensor (i.e., minutes compared to days or weeks) and will therefore produce scatter in the data that masks other, more persistent thermal features.

Even at the spatial resolution of ASTER TIR bands (i.e., 90 m) it is likely that its individual detector elements will measure radiance from surfaces at markedly different temperatures over hot volcanic targets. Any one pixel temperature will therefore give only a qualitative measure of volcanic thermal heating. However, given that the AST\* metric is restricted to measuring the size of thermally anomalous areas, it remains robust against this effect of subpixel thermal mixing. Although anomalous pixels could be identified using pixel radiance instead of pixel temperature we have utilized the latter because it is more robust against potentially variable spectral emissivity profiles as well as wavelength dependent absorption features (e.g. due to SO<sub>2</sub> or ash aerosols). ASTER TIR channels will saturate quite frequently over hot volcanic targets (i.e., saturation brightness temperatures ≈ 97 °C), especially given their

relatively small IFOV, this issue was also avoided by limiting the AST\* metric to measuring just the size of thermal anomalies.

The temperature above background was calculated by subtracting a background temperature from the NEM temperature array. The background temperature was defined as the average pixel temperature in the background area. This area was defined as an annulus around the active crater at Erta 'Ale, Kliuchevskoi and Lásca and as a collection of user-defined points at Kīlauea. The methodology for determining the optimal size of an annulus is described in detail by Murphy et al. (2011). Hot volcanic features (e.g., lava or pyroclastic flows) occasionally crossed the background area (i.e., at Kliuchevskoi). The corresponding pixels were automatically screened from the background area using a threshold of twice the standard deviation of the entire temperature array (i.e., an area of ~ 62 km<sup>2</sup>). The search area used to find anomalous ASTER pixels included (and extended beyond) the background area to ensure that all volcanic thermal features were included in the AST\* metric.

Lava flows, pyroclastic flows and ash/gas plumes typically travel in a preferred direction from a stratocone due to local topography or wind direction. The 2D projection that these features create in an image acquired from space could, for illustrative purposes, be defined as a narrow arc (< 20°) originating from the active crater. The relative magnitude of the area of intersection between an arc (i.e. an active volcanic feature) and an annulus (i.e. the background area) and the total area of the annulus is given by:

$$\frac{\alpha}{A} = \frac{\theta}{2\pi} \quad (4.5)$$

where  $\alpha$  is the area of intersection,  $A$  is the size of the background area, and  $\theta$  is the angular width of the arc in radians. For a 20° arc (i.e., 0.35 radians) the area of intersect would be 5.6% of the background area. Therefore pixels which contain contributions from cold ash plumes or warm volcanogenic material (i.e., that were not hot enough to be automatically removed by the clipping procedure) would still have a limited effect on the background temperature. The geometry of an annulus is therefore naturally stable against the intrusion of fresh volcanogenic material. Furthermore the circular nature of the annulus acts towards balancing the preferential solar heating effects that are created by varying amounts of solar irradiance around the volcanic

edifice. Therefore the annulus approach for calculating background temperatures from stratocones is favoured in this work. At the Kīlauea shield volcano, which frequently exhibits active lava flow fields covering several km<sup>2</sup>, the annulus approach was not possible. The background area was therefore defined as a collection of user-defined points around the flow field in this case. We note that a single background temperature cannot accurately characterise such an extensive area given that significant, non-volcanic variations in terrestrial temperatures occur across it. The annulus methodology (i.e., used for all volcanoes but Kīlauea) is estimated to provide background temperatures to within 5 °C based on inspection of radial temperature gradients from the active crater. This method is described in detail by Murphy et al. (2011). The user-defined points (i.e., used for Kīlauea only) give background temperatures to within 15 °C (i.e. twice the maximum standard deviation of the background data points).

#### **4.5. Wavelet Analysis**

Wavelet analysis reveals the periodicity in a time series of data. A wavelet ( $\Psi$ ) is a wave function of finite duration (i.e., it is localized). The Morlet wavelet was used with a central frequency of six for this study. A continuous wavelet transform will convert data from the time domain to a time-frequency domain through the convolution of a time series with translated (i.e. moved in time) and scaled (i.e. stretched) versions of the original wavelet function. This involves evaluating the integral of the product of the data points with the wavelet function. Conceptually this equates to quantifying the amount of overlap between the area under the curve defined by the data points and the area under the curve defined by the wavelet function. Power is the metric of this overlap. As power is calculated for a range of translation and scale parameters the resulting wavelet transform will represent how well the wavelet and the data match at different locations in time and at different periods of oscillation. A period of oscillation is the length of time over which an oscillation occurs (i.e., it is equivalent to the reciprocal of frequency). Power was normalized by the maximum value in each transform. This provides a unitless measure of periodicity that varies from zero to one. A practical guide to wavelet analysis is given by Torrence and Campo (1998). Examples of wavelet analysis in volcanology include studies of thermal image data from handheld infrared cameras (Spampinato et al., 2012) and geochemical time series measuring plume composition (Oppenheimer et al., 2009; Boichu et al., 2010).

## 4.6. Results

### 4.6.1. Time series

Figure 4.3 shows the entire MOD\* and AST\* datasets. They span the period between 24 February 2000 (i.e., the first available scene) to 1 January 2012. Erta 'Ale and Kīlauea (Fig. 4.3 a,b) have been erupting continuously over the study period. Kliuchevskoi and Láscaar (Fig. 4.3 c,d) underwent intermittent eruptive episodes that are displayed using pink shading. Eruptive histories are mostly obtained from reports of the Global Volcanism Program of the Smithsonian Institution (Venzke et al., 2002 - ).

Erta 'Ale was frequently active throughout the 11 year study period. MOD\* values are generally below  $5 \text{ W m}^{-2} \text{ sr}^{-1} \mu\text{m}^{-1}$  (i.e., 99.3 % of data points), although peaks in thermal output do occasionally exceed this values (i.e., up to a maximum MOD\* of 14.4). There are two periods where MOD\* values remain close to zero for months at a time (i.e., June - November 2003 and October 2004 to April 2005). This may indicate that the height of the lava lake was particularly low during these periods. Conversely, episodes characterized by high lava lake levels - as observed in the field (e.g., November 2010 overflow) - correspond with peaks in MOD\* values (i.e., 7.0 in this case). Variations in lava lake height are controlled by a number of factors, including magma reservoir pressure, vesiculation and conduit-crater morphology.

The size of the thermal anomaly, as given by the AST\* metric, varies between roughly  $1 - 4 \times 10^5 \text{ m}^2$  (i.e., 1 - 5 ASTER pixels). The linear Pearson correlation coefficient between AST\* and MOD\* is 0.54. That is, the size of thermally anomalous areas as measured by ASTER does not show a particularly strong correlation with the MIR radiance measured by MODIS. This is because the radiance emitted from the lava lake varies considerably more than the size of the lava lake. Radiant output can change significantly for a given lake area, for example, through convective overturning of the lake surface and bubble burst, both of which result in varying exposure of hot, incandescent material through time.

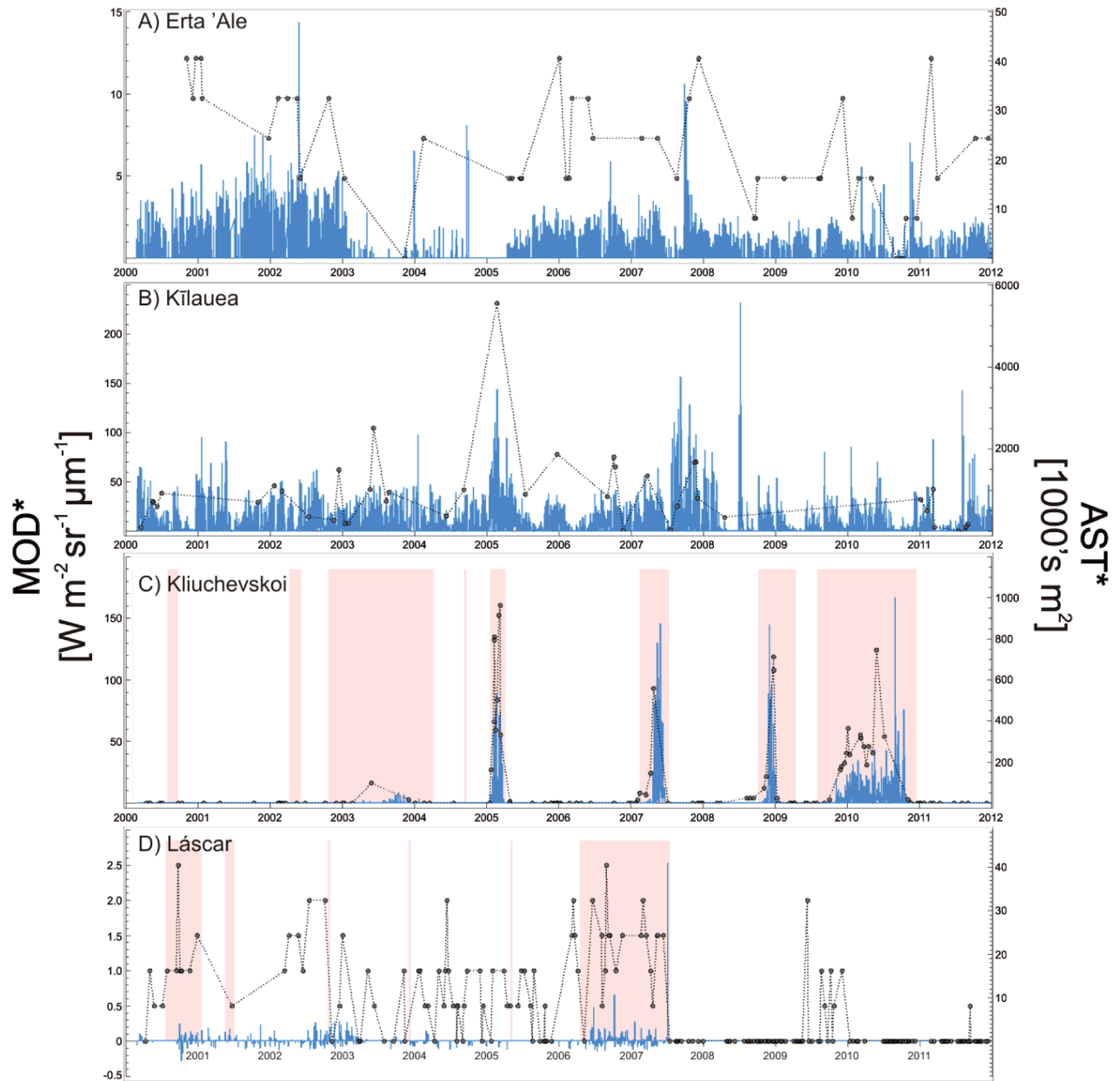


**Figure 4.3.** The MOD\* time series (blue bars) is a measure of volcanic radiance  $[\text{W m}^{-2} \text{sr}^{-1} \mu\text{m}^{-1}]$ ; the AST\* time series (filled circles with a dotted trend line) represents the size of thermally anomalous areas  $[1000\text{'s m}^2]$ . Pink bars depict discrete eruptive episodes.

Kīlauea is the most consistently active volcano in this study and is characterized by frequent fissure, flank and crater eruptions of low viscosity basalt lava. These effusive eruptions often result in tube fed flows that are capable of travelling several kilometres from the source vent. Consequently the MOD\* time series displays a relatively high average of

$7.5 \text{ W m}^{-2} \text{ sr}^{-1} \mu\text{m}^{-1}$  with peaks exceeding  $50 \text{ W m}^{-2} \text{ sr}^{-1} \mu\text{m}^{-1}$  (i.e. coincident with outbreaks from the lava tubes). Several episodes of elevated thermal emission are apparent (e.g., January-September 2005, July 2007 to April 2008, and July 2008). The latest of these is particularly significant because it was the largest in the data set (i.e., MOD\* of 232; 7<sup>th</sup> July 2008), it occurred during the eruption of three simultaneously lava fountains (BGVN 2010) and yet was completely missed by the ASTER sensor.

Although high spatial resolution imagers, such as ASTER, are more likely to miss such short lived dynamic events, the imagery that they provide offer superior constraints on the size, shape, orientation and location of thermal anomalies. For example, a lava flow field imaged simultaneously by both sensors on 7 June 2003 (Fig. 4.4) exhibits individual lava tubes of varying age that clearly form an interconnected network in the ASTER image (Fig. 4.4a), whilst it is only possible to determine the orientation and length of the overall flow field in the MODIS image (Fig. 4.4b).

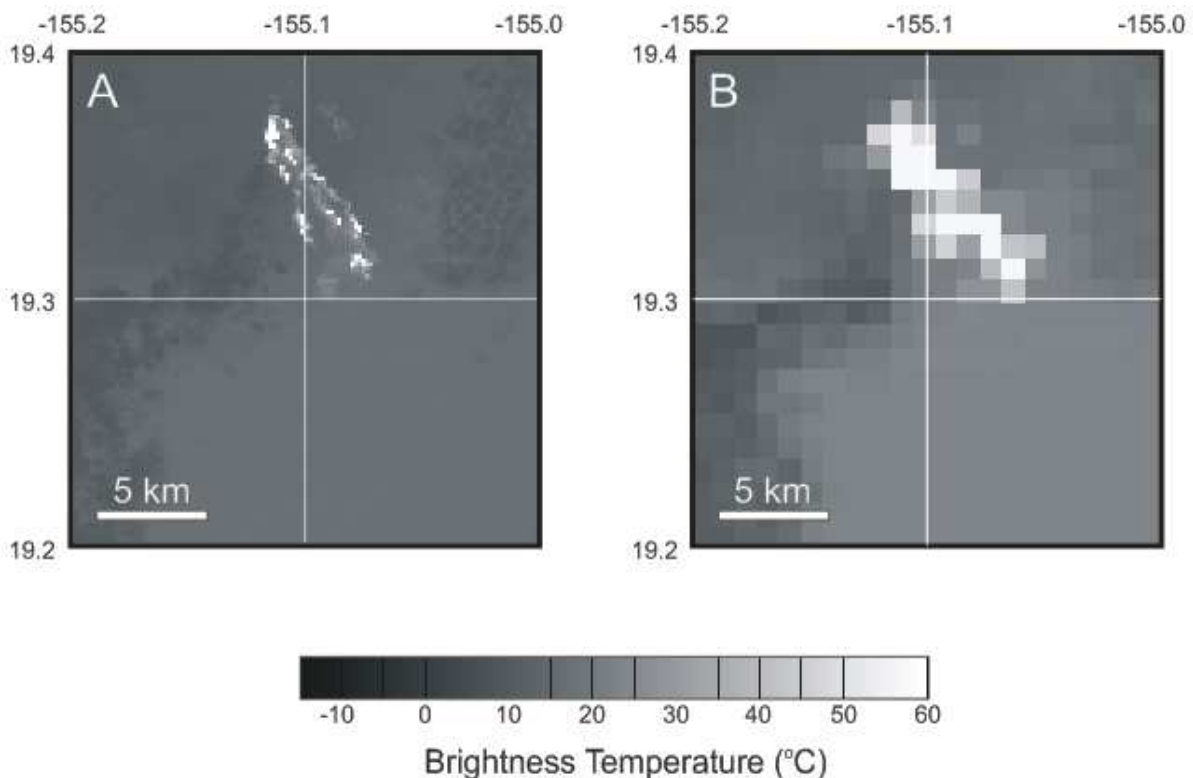


**Figure 4.4. Brightness temperatures from a) ASTER channel 10 and b) MODIS channel 22 of the Pu'u 'Ō'ō flow field on the 7<sup>th</sup> June 2003. ASTER is able to characterize the size, shape, location and orientation of individual lava flow tubes.**

High spatial resolution data, as exemplified here by ASTER, would clearly be more useful for operational assessment of i) damage to local infrastructure (e.g., buildings, roads, etc.), ii) future flow direction (especially given that surface breakouts occur from the tubes), and iii) the risk of fire (e.g., through proximity to combustible material), given timely availability of the image, or a high-level monitoring product derived from the image.

The size of thermal anomalies at Kīlauea have a mean AST\* value of  $8.9 \times 10^5 \text{ m}^2$  (i.e., 110 pixels) with a standard deviation of  $9.6 \times 10^5 \text{ m}^2$  (i.e., 118 pixels). They can therefore be very large yet also vary significantly in size through time. The most extensive anomaly in the AST\* series is  $5.55 \times 10^6 \text{ m}^2$  (i.e., 685 pixels). The correlation coefficient between AST\* and MOD\* is 0.65 (i.e. anomaly size and MIR radiance are more closely matched at this volcano than at Erta ‘Ale).

Kliuchevskoi exhibits a more sporadic eruptive style, often spending prolonged periods of time with no, or very limited signs of thermal activity (Fig. 4.3c). There are four major peaks in the MOD\* series i) 20 January to 7 April 2005, ii) 22 April to 25 June 2007, iii) 30 October 2008 to 10 January 2009, and iv) 1 November 2009 to 1 November 2010. These correspond with Strombolian eruptions and lava flows (Venzke et al., 2002 - ). The first three major peaks are fairly symmetric and last around 2-3 months. The fourth is asymmetric and last for about a year, with a prolonged period of Strombolian activity, followed by more extensive lava flows and culminating in a Vulcanian eruption (Venzke et al., 2002 - ) after which time thermal activity came to an abrupt end.

The maximum MOD\* values for the symmetric peaks are, in consecutive order: 88.6, 145.8 and 144.9. These peaks have mean MOD\* values of 10.4, 30.0 and 11.8, respectively. The fourth major peak displays a higher maximum MOD\* value (i.e., 166.7) and a lower mean MOD\* value (6.9). The maximum extents of thermal anomalies during these four major episodes range from  $5.6 \times 10^5$  to  $9.6 \times 10^5 \text{ m}^2$ . That is, they are comparable in size of Kīlauea flows, although overall slightly smaller. Correlation between AST\* and MOD\* is relatively high overall (i.e. 0.85). The increased correlation between size and intensity at Kliuchevskoi compared to Kīlauea is probably because lava flows from Kliuchevskoi’s stratocone do not form tubes. At Kīlauea however the formation of tubes means that radiance from these flows will depend on the proportion of exposed to concealed lava.

Inspection of ASTER scenes reveals a thermal precursor to two of the lava flow events (Fig. 4.5). The precursor is defined by thermal anomalies that are situated within the summit crater and that increase in both size and intensity through time. The increase in size is interpreted as resulting from an increasing amount of ponded lava in the active crater, as has been observed in the field (BGVN 2009).

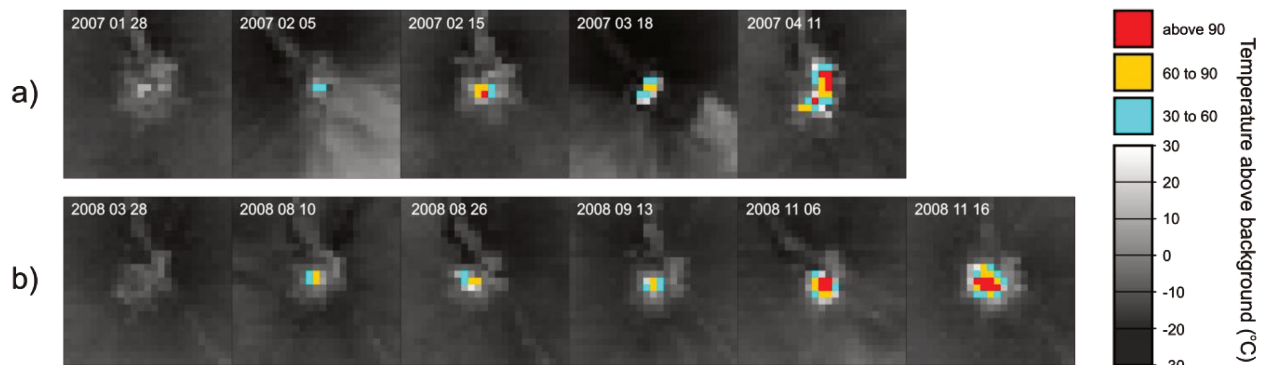


**Figure 4.5. Thermal precursors to lava flow activity at Kliuchevskoi are characterized by anomalies in the active crater that increase in size and intensity.**

The increase in intensity is due to greater radiant heat loss from the lava surface, which is dependent on both size and temperature. After the precursory infilling of the summit crater, lava breached the crater rim and descended the flanks of the volcano (BGVN 2007,2009). Such observations could be used to create simple, automated thermal precursors to lava flow activity at Kliuchevskoi and other similar volcanoes. If, for example, an alert had been based on detection of 5 or more pixels situated in the active crater with a temperature above background of at least 40 °C, then both lava flow events could have been anticipated two weeks before they were seen descending the flank. This demonstrates the utility that moderate to high spatial resolution datasets can provide when their revisit periods are adequate to capture changing levels of activity.

Láscar displays very low MOD\*, i.e., mainly lower than 0.5 and with a maximum of 2.5 (Fig. 4.3d). Scatter in MODIS anomalies, created by imperfect correction for MIR background radiance and atmospheric effects, can result in negative anomaly values. Thermal activity at this volcano, characterized by persistent degassing from fumaroles in and around the active crater, is particularly difficult for low spatial resolution sensors such as MODIS to detect because the

thermally active region is low in temperature, and relatively small in size compared to the instantaneous field of view (IFOV) of the sensor. Consequentially the radiation falling on any one detector element contains a limited contribution from the target area. ASTER, on the other hand, regularly detects thermal anomalies at Láscar. AST\* values range from roughly 10,000 to 40,000 m<sup>2</sup> in size. These anomalies are probably due to varying degrees of fumarolic activity from the active crater (Murphy et al. 2011). The higher spatial resolution (i.e. smaller IFOV) of ASTER allows it to detect relatively subtle thermal anomalies. Figure 4.6 illustrates this point by displays an ASTER image of a persistent thermal anomaly in Láscar’s active crater (Fig. 4.6a) juxtaposed with a contemporaneous MODIS image acquired over the same area (Fig. 4.6b). The anomaly is evident in the ASTER image yet remains completely undetected by the MODIS sensor.

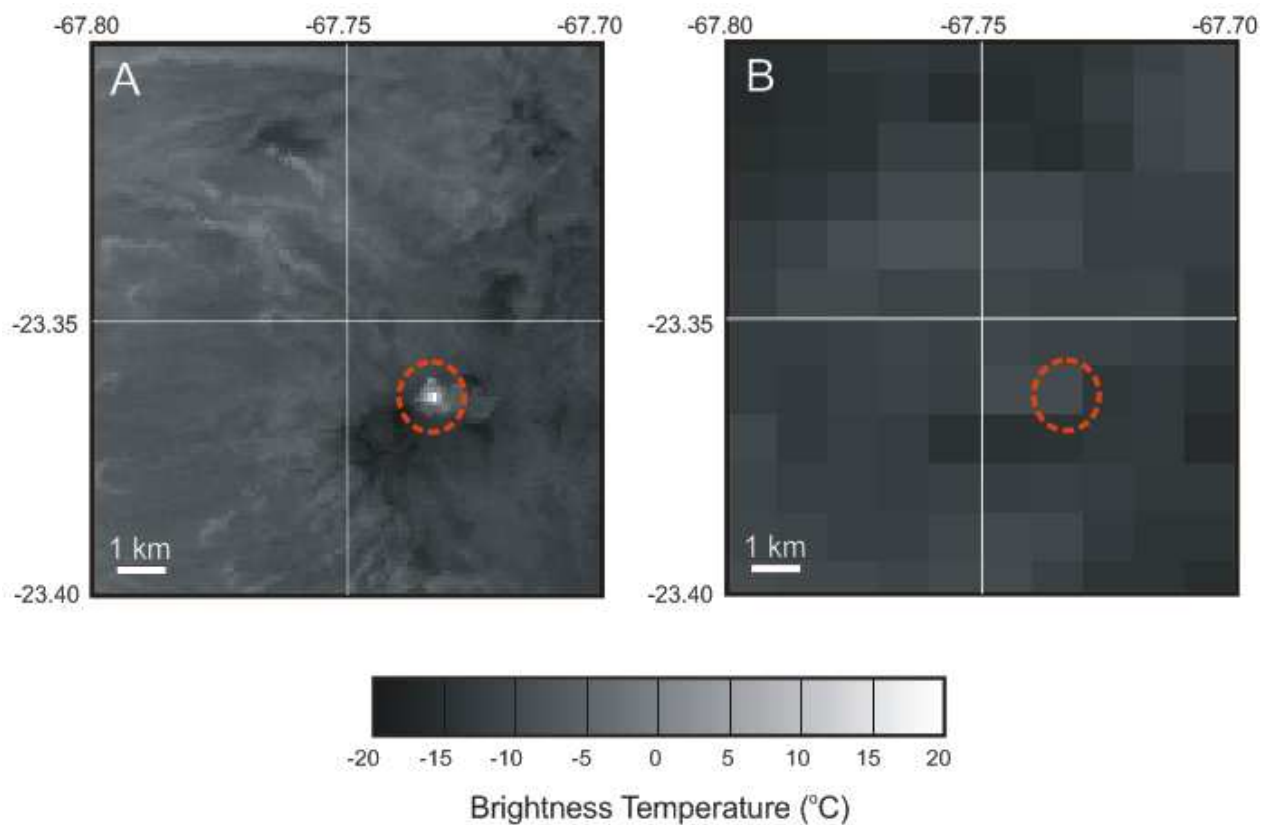


**Figure 4.6. Contemporaneous images of a) ASTER channel 10 and b) MODIS channel 22 of Láscar taken on 2<sup>nd</sup> October 2000. ASTER is capable of detecting subtle thermal anomalies that may fall below the MODIS detection limit. Láscar’s active crater is highlighted using a red dashed circle.**

#### 4.6.2. Wavelet Power Spectra

The high temporal resolution of MODIS lends itself to more detailed time series analysis. A continuous wavelet transform was applied to the MOD\* time series of a) Erta 'Ale, b) Kīlauea and c) Kliuchevskoi (Fig. 4.7). Shown for each volcano are i) the original MOD\* time series, and ii) the wavelet power spectrum.

The axes of the wavelet power spectrum are time against period of oscillation. Time is plotted in years (x-axis) and period of oscillation is plotted in years (left y-axis) using a log base 2 scale and also in the equivalent amount of days (right y-axis). Power is represented using a colour scale. Peaks in the power spectrum (i.e. warmer colours) indicate periodicity in the time series at the corresponding time and period of oscillation. During the convolution process wavelets may be translated towards (or beyond) the edge of the finite time series, especially at longer periods, producing spurious results in the corresponding part of the power spectrum. This region is known as the cone of influence and is represented in grey to leave only the reliable part of the power spectrum visible. Certain instances in time are highlighted in the power spectrum using a vertical, dashed white line. The corresponding period against power plot for each of these time slices is displayed in Figure 4.8.

Erta 'Ale (Fig. 4.7a) displays two time intervals revealing a periodicity of approximately 1/2 a year centred around June 2002 and August 2007. The latter event also shows significant periodicity at 1/16 to 1/4 of a year (i.e., 23 - 91 days). A time slice of the power spectrum at these two times (i.e. time slice 1 and 2) is displayed in Figure 4.8. These time slices also clearly show low period signals (i.e. around 2 days) that are approximately contemporaneous with sharp peaks in the MOD\* time series (Fig. 4.7ai). A strong periodicity (i.e., power = 0.93) occurs at a long period (i.e., 4 years) around the turn of 2006 (Fig 4.7a). It is associated with the spacing between the two periodicity events highlighted in time slice 1 and 2. This spacing is actually closer to 5 years than 4 but is not definable within this power spectrum because the corresponding periodicity falls into the cone of influence. To characterize longer period events, such as this one, it is necessary to have a longer time series. Less prominent peaks also appear in the power spectrum of Erta 'Ale. Most remarkable among these are perhaps the dual periodicity component at  $6.16 \times 10^{-3}$  and  $2.3 \times 10^{-2}$  years (i.e., 2 and 8 days) because they reoccur throughout

much of the time series and therefore appear to be characteristic periods of oscillation at this volcano.

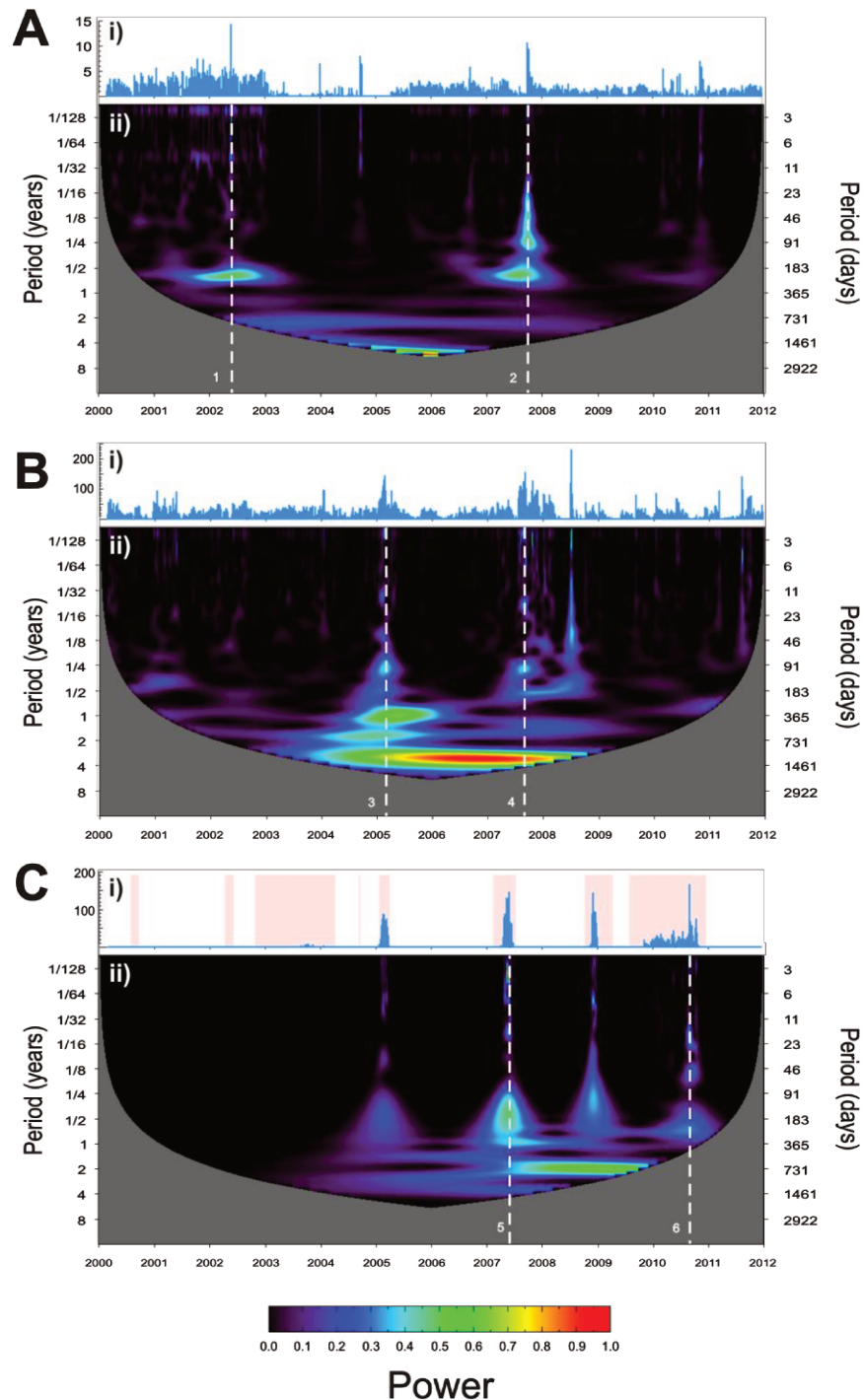
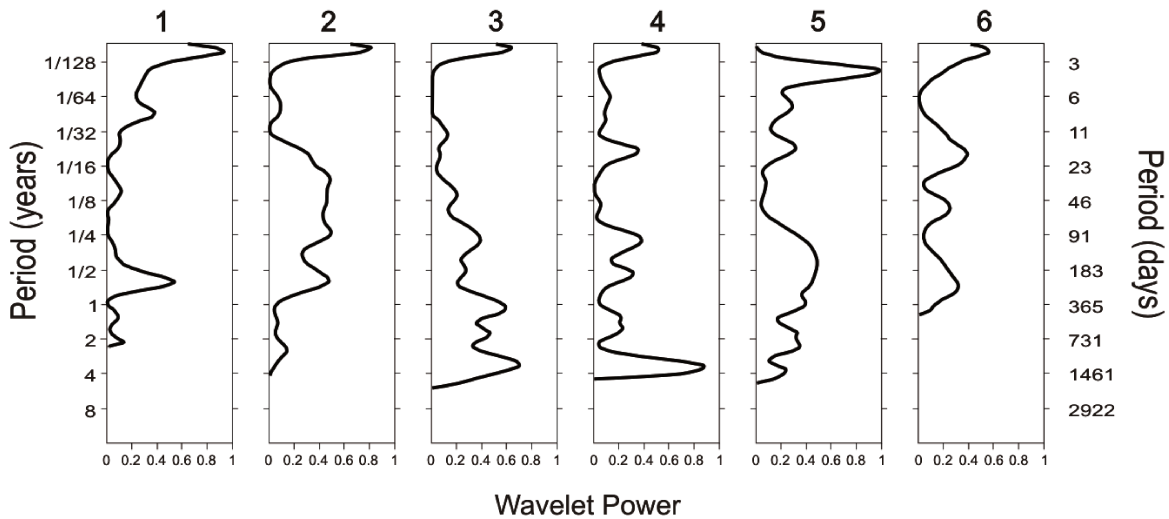


Figure 4.7. Wavelet transforms of MOD\* time series for a) Erta 'Ale, b) Kilauea and c) Kliuchevskoi. Shown are i) the original MOD\* time series and ii) its wavelet power spectrum. Time slices of the power spectrum (shown in Fig. 4.8) are depicted here using dashed white lines.



**Figure 4.8. Time slices of wavelet power against period.**

Kīlauea displays strong periodicity at a period of 2.5 years with maximum power of this feature occurring around October 2006 (Fig. 4.7bii). This long period signal is overlain at different times with shorter period oscillations. Time slices 3 and 4 (Fig. 4.8) display some of the multiple periodicity components in the Kīlauea power spectrum. The long (i.e. 2.5 year) period is the dominant feature in these time slices however both also show periodicity at around 1/4 of a year and at 2 days. Time slice 3 also shows a peak in periodicity at around 1 year which is equivalent to the duration of the overall waxing and waning in radiance in the corresponding time series (Fig. 4.7bi). A strong low period oscillation (i.e. 2.6 days) in the power spectrum occurs during a short sharp peak in MOD\* values around July 2008.

The four major eruptive episodes at Kliuchevskoi dominate both the time series and the wavelet power spectrum (Fig. 4.7cii). The three symmetric events each show a waxing and waning of measured radiance with a periodicity of approximately 0.25 to 0.5 years (e.g., time slice 5 in Fig. 4.8). The maximum periodicity event (i.e. power = 1) for Kliuchevskoi is displayed in time slice 5 (i.e., period = 3.5 days; centred on the 31<sup>st</sup> May 2007). It occurred at the same time that a new lava flow was reported to have moved down the East flank of the volcano (BGVN 2007). Periodicity during the episode with more persistent Strombolian activity (i.e., time slice 6) displays more clearly separated peaks in period at 2.5, 16.5, 47 and 204 days. The fairly regular spacing (i.e., repose) of the last three eruptive episodes resulted in a 1.5 year periodicity centred around the turn of 2009.

## 4.7. Discussion

The MODIS and ASTER sensors provide datasets with their own particular advantages and disadvantages. MODIS channel 21 will very rarely saturate, even over hot volcanic targets, and can therefore be reliably used to provide a measure of volcanic thermal radiation if the target is hot and/or large enough. The daily revisit time of the MODIS sensor also allows dynamic volcanic events to be characterized in relatively high temporal detail. This sampling frequency could be improved further still, if necessary, by inclusion of data from the other MODIS sensor (i.e., on the Aqua satellite) as might be of critical importance during a volcanic crisis. The higher spatial resolution of the ASTER sensor, on the other hand, allows the spatial characteristics of thermal anomalies to be quantified more accurately and also facilitates the detection of subtle thermal anomalies. These capabilities permitted the identification of a thermal precursor to lava flows at Kliuchevskoi. Unfortunately the probability of ASTER capturing such precursors events is limited by the fact that it is not a mapping mission (i.e. does not acquire data continuously).

The low spatial resolution of MODIS leaves the sensor incapable of monitoring the type of thermal activity expressed by Láscar during the study period (i.e., predominantly fumarolic). There are plenty of other (potentially hazardous) volcanoes around the world that are similarly difficult for MODIS to monitor. Fortunately ASTER can provide a complimentary dataset that, when used in conjunction with MODIS datasets, has a better overall temporal, spatial and radiometric resolution. This can be used to obtain more information on a greater range of volcanic activity than either sensor could offer individually.

This is the first time to our knowledge that wavelet analysis has been applied over such a long (i.e., 11 year) data set of volcanic radiance. This enabled us to identify oscillations on weekly, monthly and yearly time scales. Very short period events (i.e., a few days) can be created by a burst of thermal activity such as from a short lived lava flow or lava fountain. It is possible, however, that similar oscillations in radiance - as seen from space - might also occur due to changes in cloud cover over a thermally stable target. Very short period events should therefore be interpreted with care and scenes should be inspected for cloud cover.

Long period events could be better resolved if the overall time series were more extensive. This reflects the need for continuous collections of data over multiple years and, eventually, decades. Fortunately the next generation of high temporal resolution polar-orbiting

satellites are coming through (i.e., Suomi National Polar-orbiting Partnership (Suomi NPP), Sentinel 3, and the Global Change Observation Mission climate change series (GCOM - C)). Wavelet analysis provides new constraints on the probability of the duration and repose of future events, and could be used as input into decision making tools such as the Bayesian event tree model for eruption forecasting, i.e., BET EF (Marzocchi et al., 2008).

## **4.8. Conclusion**

This study investigated a collection of 11 year time series of MODIS and ASTER thermal anomalies (i.e., using the metrics MOD\* and AST\*, respectively) at four different volcanoes. MOD\* measures the radiance emitted by a volcano and AST\* measures the size of thermally anomalous areas. This is the first time (to our knowledge) that two sensors of this type have been used to compare such long time series of the intensity and size of thermal anomalies. We show practical examples of the relative strengths of each sensor and how they can be used to improve overall understanding of volcanic activity at a number of distinctly different volcanoes.

The high temporal resolution MOD\* metric was also analyzed using continuous wavelet transforms. Given the length of the time series it was possible to determine periods over which thermal activity waxes and wanes at a particular volcano as well as to characterize repose time between thermal events. This might be useful in guiding forecasts on the duration and onset of future eruptions. It also facilitates the comparison of the time scales over which different volcanoes erupt. The AST\* metric allowed the size of thermal anomalies to be determined in relatively high detail, it also facilitate the detection of subtle thermal anomalies, both of these characteristics led to the identification of a thermal precursor to lava flow at Kliuchevskoi. It is useful, therefore, to explore synergies between high temporal and high spatial resolution datasets.

Time series plots, images and movies can be thought of as volcano monitoring products. These products could be made automatically and provided free of charge to volcano observatories and other interested parties. This would increase the science return from existing and future missions, raise the global profile of the space agency or corporation that provides the data and also contribute positively to society, especially to those at risk from volcanic hazards, be it either directly (e.g., local inhabitants) or indirectly (e.g., airplane passengers and international businesses).



# Chapter 5

## Calculating Radiant Flux from Thermally Mixed Pixels

---

S. W. Murphy, C. Oppenheimer, C.R. de Souza Filho

To be submitted to IEEE Transactions on Geoscience and Remote Sensing

### **5.1. Abstract**

Volcanic activity involves the transfer of hot material to the Earth's surface. This can be monitored on a global scale from space using infrared imagers on board satellites. However, surface temperature gradients at volcanoes, as well as other natural heat sources such as fires and geothermal fields, typically change significantly on the scale of a single pixel footprint (i.e. the area subtended by the instantaneous field of view of a single detector element). Consequently a pixel footprint will contain multiple thermal components over such heat sources. This paper explores the calculation of radiant flux from thermally mixed pixels through model fitting of spectral radiance. This is achieved using a new approach based on spectral libraries (i.e. a collection of the radiance spectra that might be measured over active terrestrial heat sources). Two spectral libraries were built. One for short-wave infrared (SWIR) imaging spectrometers, such as those that are currently in orbit or about to be launched (e.g. Hyperion, EnMap, Hisui),

and another for imaging spectrometers with SWIR, mid infrared (MIR) and thermal infrared (TIR) channels, representing data that might be collected from a future class of imaging spectrometers (e.g. HypsIRI). Spectral radiance can be modelled to within 3% for spectrometers with just SWIR channels and to within 5 % for those with SWIR, MIR and TIR channels. We suggest that this is within the accuracy to which spectral radiance can be reliably measured from space over hot volcanic targets. Radiant flux SWIR spectrometers can be measured to within 20%; this is an improvement over existing methods. In contrast SWIR-MIR-TIR spectrometers ought to be able to measure radiant flux to within 1%. We infer that it might not be possible to reliably resolve the number, size and temperature of subpixel components from spectral information alone, and therefore suggest that radiant flux and radiant exitance are more reliable and accurate measures of thermal activity as seen from space. A practical example of our approach is demonstrated using Hyperion images of a lava flow from Kliuchevskoi volcano (Russia) in 2007. The upcoming generation of orbital spectrometers offers an opportunity to implement the proposed algorithms operationally.

## 5.2. Introduction

Volcanism is driven by heat transfer from the planet's interior to its surface. Satellites can monitor this fundamental driving force by measuring radiance from volcanic surfaces. Planck's law describes the relationship between spectral radiance, temperature and wavelength which, when modified to account for spectral emissivity, can be expressed as follows:

$$L(\lambda, T) = \varepsilon_{\lambda} c_1 \lambda^{-5} / [\exp\left(\frac{c_2}{\lambda T}\right) - 1] \quad (5.1)$$

where  $L(\lambda, T)$  is spectral radiance ( $\text{W m}^{-2} \text{sr}^{-1} \mu\text{m}^{-1}$ ) as a function of wavelength ( $\lambda$ ) and temperature ( $T$ ),  $\varepsilon_{\lambda}$  is spectral emissivity, and  $c_1$  and  $c_2$  are the radiation constants (i.e.,  $c_1 = 2hc^2 = 1.19 \cdot 10^{-16} \text{ W m}^2 \text{sr}^{-1}$  and  $c_2 = hc/k = 1.439 \cdot 10^{-2} \text{ m K}$ ; where  $h$  is the Planck constant,  $c$  the speed of light and  $k$  the Boltzmann constant). To obtain a better understanding of conditions at the target surface it is often desirable to convert radiance into units that represent more tangible characteristics of the volcano, e.g., surface temperature distribution or radiated heat output in Watts. This facilitates monitoring of changes in thermal budgets over time and comparing

activity between different volcanoes (e.g. Glaze et al. 1989). Metrics of radiant heat output include radiant flux,  $\phi$ , which is the rate of photon energy transfer (i.e. Watts), and radiant exitance,  $Q$ , which is a measure of radiant flux from a given surface (i.e. Watts per metre squared). The Stefan-Boltzmann law relates the radiant exitance from an isothermal surface to its temperature:

$$Q = \epsilon\sigma T^4 \quad (5.2)$$

where  $\epsilon$  is emissivity,  $\sigma$  is the Stefan-Boltzmann constant ( $5.67 \cdot 10^{-8} \text{ W m}^{-2} \text{ K}^{-4}$ ), and  $T$  is temperature in Kelvin. The temperature of an isothermal surface can be obtained from spectral radiance by rearranging (5.1) appropriately.

$$T(\lambda, L) = \frac{c_2}{\lambda \ln [\epsilon c_1 / L \lambda^5 + 1]} \quad (5.3)$$

However, in a volcano monitoring context, it is usually not valid to assume that a surface will be isothermal at the pixel scale. Thus radiance that reaches a single detector element of a sensor is comprised of a mixture of contributions from a continuous temperature distribution that can, at some point, be discretised (i.e. be assumed to be composed of  $n$  isothermal components) for the purposes of modelling with negligible impact on the derived quantities. The radiant flux from an area can therefore be described as follows:

$$\phi = \epsilon\sigma A \sum_{i=1}^n f_n T_n^4 \quad (5.4)$$

where  $A$  is the size of a pixel footprint, whilst  $f_n$  and  $T_n$  are the fractional area and temperature of the  $n^{\text{th}}$  subpixel thermal component. The aim of this work is to improve methods for calculating radiant flux for thermally mixed pixels. We also examine the feasibility of resolving the number, temperature and fractional area of individual subpixel components. These metrics are used in a range of disciplines including: volcanology, fire monitoring and geothermal exploration.

### 5.3. Existing methods for calculating radiant flux

Hot volcanic features such as lava flows and fumaroles are often several hundreds of degrees hotter than the ambient background temperature, and display continuous temperature distributions, with thermal gradients reaching up to and beyond  $500\text{ }^{\circ}\text{C m}^{-1}$  (e.g. Oppenheimer et al. 1993b, Wright and Flynn 2003). The surface temperatures of such features can therefore change dramatically over the length scale of one metre. Yet high spatial resolution imagers with wavebands sensitive to volcanic heating (i.e.  $2 - 12\text{ }\mu\text{m}$ ;  $100 - 1200\text{ }^{\circ}\text{C}$ ) have pixel sizes on the order of  $30 - 60\text{ m}$ . It is therefore likely that these active heat sources will be far from isothermal at the pixel scale. This is called the thermal mixing problem and a number of methodologies have been proposed to tackle it.

#### 5.3.1. Dozier Technique.

The first published attempts to determine the temperature and size of subpixel thermal components were provided by Matson and Dozier (1981) and Dozier (1981). They assumed just two thermal components in a thermally mixed pixel. This allowed them to use a MIR and a TIR channel from the Advanced Very High Resolution Radiometer (AVHRR) to define and then solve for the following simultaneous equations:

$$L_x = fL_{x,hot} + (1 - f)L_{x,cold} \quad (5.5)$$

$$L_y = fL_{y,hot} + (1 - f)L_{y,cold} \quad (5.6)$$

where  $L$  is spectral radiance,  $f$  is fractional area,  $x$  and  $y$  denote different wavebands and the subscripts hot and cold denote relative temperature. There are two equations and three unknowns (i.e. a fractional area and two temperatures). Solutions to these simultaneous equations require that one of the unknowns can be assumed *a priori*. This technique was developed for fire monitoring purposes but is extendable generally to any situation where thermally mixed pixels occur. It became known as the 'bi-spectral method' in the fire monitoring community and the 'dual-band technique' within the volcano monitoring community after being adopted by Rothery

et al. (1988). Of course, with more distinct sensor channels, multicomponent models can be evaluated (e.g. Oppenheimer, 1993a). Once subpixel characteristics (i.e. number, temperature and size of subpixel components) have been obtained it is possible to calculate radiant flux using equation 5.4 (e.g. Glaze et al. 1989)

Although used extensively in different fields, the Dozier technique does not provide a reliable measure of the subpixel characteristics from natural heat sources. This is in part due to the sensitivity of simultaneous equation solutions to the required *a priori* assumption (e.g. Oppenheimer et al. 1993b). However, when more than two spectral channels are available it is possible to avoid making such assumptions (e.g. Flynn et al. 1993). The principal reason that the Dozier technique cannot be reliably used to obtain subpixel characteristics is that the continuous temperature distribution of volcanic thermal features is not well characterized by just two or three thermal components, be they fumaroles (e.g. Oppenheimer et al. 1993b) or lava flows (e.g. Wright & Flynn 2003). Furthermore there is a tacit assumption that all subpixel areas are radiating significantly (i.e. the sum of subpixel fractional areas is unity). This is not valid in the case that the method uses just SWIR wavelengths, as ambient background surfaces (i.e.  $< 100^{\circ}\text{C}$ ) will not radiate significantly in this wavelength region. An analysis of the accuracy of the Dozier technique revealed that, even if an active surface could be assumed to be composed of just two thermal components, the 'best possible' retrieval of temperatures and fractional areas were only to within  $\pm 100^{\circ}\text{C}$  and 0.5 at one standard deviation (Giglio & Kendall 2001). Despite these shortcomings the methodology continues to be used to make semi-quantitative inferences about subpixel characteristics of thermally mixed pixels (e.g. Lombardo et al. 2006, Vaughan et al. 2010, Blakett & Wooster 2011).

### 5.3.2 Wooster Technique

Wooster et al. (2003) developed a method for determining radiant flux from thermally mixed pixels using a single mid-infrared channel without the need to assume subpixel characteristics. It was based on the fact that the Planck function (equation 5.1) can be approximated using a power law within limited temperature and wavelength ranges.

$$L(\lambda) = aT^b \quad (5.7)$$

where  $a$  and  $b$  are empirically derived constants. At a wavelength of around  $4 \mu\text{m}$  and temperature range of approximately  $300 - 1200 \text{ }^\circ\text{C}$  the exponent,  $b$ , also has a value of around 4. Thus, under these wavelength and temperature conditions, equation 7 approximates the Stefan-Boltzmann law (i.e. equation 2). This allows the following linear relationship between radiance and radiant flux to be derived.

$$Q = c(L - L_{bkgd}) \quad (5.8)$$

where  $c$  is a sensor specific empirically derived constant,  $L$  is the radiance measured from a  $4 \mu\text{m}$  channel and  $L_{bkgd}$  is the background radiance in that channel. Background radiance is typically estimated from neighbouring 'ambient' pixels. This allowed radiant flux from hot targets to be estimated to within  $\pm 30\%$  (Wooster et al. 2003). The approach was later adopted by the volcano monitoring community for monitoring radiant flux from all of the Earth's subaerially erupting volcanoes over a seven year period (Wright & Pilger 2008) and to create a twelve year time series of radiant flux from Stromboli volcano (Coppola et al. 2012).

### 5.3.3. Model-fitting Approach

Imaging spectrometers acquire a radiance spectra for each pixel location; these spectra can be modelled as follows:

$$L_n(\lambda) = \sum_{i=1}^n \epsilon_\lambda f_i L(\lambda, T_i) \quad (5.9)$$

where  $L_n(\lambda)$  is the total spectral radiance from  $n$  subpixel thermal components at a given wavelength  $\lambda$ ,  $\epsilon_\lambda$  is spectral emissivity,  $f_i$  and  $T_i$  are the fractional area and temperature of the  $i^{\text{th}}$  component, and  $L(\lambda, T)$  is blackbody radiance at  $T_i$ . Emissivity spectra are assumed to be identical for all subpixel components within a given pixel footprint; which ought to be valid in the majority of volcano monitoring cases.

It is therefore possible to obtain subpixel characteristics from hyperspectral images by model fitting. Oppenheimer et al. (1993c) achieved this using the simplex algorithm to resolve two thermal component solutions from hot volcanic surfaces imaged by the Airborne Visible/Infrared Imaging Spectrometer (AVIRIS). Wright and Flynn (2003) evaluated equation 5.9 using a Levenberg-Marquardt gradient solver. This allowed the optimal number of subpixel solutions to be found automatically. They found that just two or three components were typically required to find a reliable flux estimate (i.e. one that did not change as the number of modelled thermal components increased).

#### **5.4. Reliability of Radiant Flux estimates**

Here we provide an explanation as to why radiant flux can be reliably obtained with simple thermal component models (i.e. just two or three components) even though such models do not reliably represent the number, temperature or fractional area of subpixel components. The integral of the Planck function (i.e. equation 1) with respect to wavelength is radiant exitance (equation 5.2). Radiant exitance is therefore equivalent to the region under the graph of spectral radiance. This is directly proportional to radiant flux by the factor of a surface area (i.e. in this case the area of a pixel). Therefore to calculate radiant flux all that is required is to be able to determine the region under a graph of spectral radiance and know the pixel size of the detector. The direct approach to solve the integral of spectral radiance would involve making a sufficiently continuous number of spectral measurements. Unfortunately this is not possible due to atmospheric absorption. Therefore it is necessary to fit a model to the parts of the spectrum that we can measure. It is not really relevant whether the subpixel characteristics used in a model are themselves accurate with regards to accurately calculating radiant flux. All that matters is that the area under the radiance spectrum is well characterized. This can be achieved by using a relatively simple thermal model.

For any given model of a measured radiance spectrum the curve-fitting accuracy will always be lower than the area-fitting accuracy. That is, the proportional difference between the measured and the modelled curve will be higher than the proportional difference between the measured and modelled areas under those curves. Radiant flux estimates require good area-fitting

accuracy, conversely subpixel characterization requires good curve-fitting accuracy. Whether or not such a level of curve-fitting accuracy is practically obtainable is discussed later.

There is a multitude of ways of fitting a model to a data set. Using a gradient solver is one of them. Here we suggest an approach that is based on a spectral library. This offers notable advantages over the gradient solver approach: i) it will always converge towards (i.e. find) a solution, ii) it will always find the global minimum (i.e. the best solution that it is capable of finding) and iii) it is less computationally expensive (i.e. as solutions need only be called from memory), thus making them particularly well suited for calculations on board remote sensing platforms.

## **5.5. A Spectral Library Approach**

A spectral library, in this piece of work, is defined as a collection of radiance spectra that represent the possible range that might be measured by an orbital imaging spectrometer when acquiring data over an active volcano. Spectral libraries can be used to fit models to measured radiance spectra by finding the best match in the library to the measured data. Two classes of spectral library were created. They correspond to the two classes of orbital imaging spectrometers considered in this study i) those which have only SWIR channels and ii) those with SWIR, MIR and TIR channels. The first represents the wavelength ranges of existing, or soon to be in orbit, imaging spectrometers such as Hyperion, EnMap and Hisui. The second represents a future class of sensors such as the HypsIRI mission, which is currently being considered for development by NASA (e.g. Hook & Oaida 2010). These two categories will be referred to as i) current-class and ii) future-class for the remainder of this article. The wavebands used to create each library are assumed to be well represented by a single central wavelength (Table 5.1). The wavebands of the current-class library correspond to Hyperion channels whilst those for the future-class of sensor are based on proposed HypsIRI channels (Hook & Oaida 2010).

The current-class of sensors has a pixel size of 30 m. The future-class has a larger pixel size, i.e. 60 m, as has been proposed for the HypsIRI sensor in order to ensure high signal to noise ratios in the TIR bands. A three component thermal model was used to create the library spectra. The size of subpixel thermal components is measured in fractions of a pixel area. The fractional areas used to create the libraries range from 0.0025 to 0.95 for the current-class, and

0.00028 to 0.9992 for the future-class. The sum of subpixel components was not forced to be unity for the current-class library (i.e. because components lower than approximately 100 °C will not radiate significantly in the SWIR) but it was for the future-class library (i.e. because TIR wavelengths will be sensitive to the radiance emitted by non-active background surfaces). Increments in fractional area were not constant but instead were smallest at the lowest fractional areas and increased in size at larger fractional areas. This significantly reduced the size of each library and therefore increased the speed of library searches. The temperatures of thermal components used to make the library spectra ranged from 100 to 1110 °C for the current-class, and -30 to 1105 °C for the future-class. Cooler thermal components were included in the future-class library because such surfaces will emit significant amounts of radiance at TIR wavelengths. There were  $1.0 \times 10^7$  spectra overall in the current-class library and  $1.6 \times 10^7$  in the future-class library.

**Table 5.1. The central wavelengths used to create the spectral libraries**

current-class		future-class
wavelength (nm)	Hyperion band #	wavelength (nm)
711.7	36	1000
864.4	51	1250
1053.7	91	1530
1255.5	111	1700
1608.6	146	2100
1709.5	156	2300
2102.9	195	3980
2203.8	205	7350
2304.7	215	8280
		8630
		9070
		10530
		11330
		12050

## 5.6. Monte Carlo testing

The number of possible spectra that an imaging spectrometer could measure is extremely large. It is therefore not possible to exhaustively test a methodology for calculating radiant flux against all possible spectra that could be measured in practice. We therefore test the ability of each spectral library at calculating radiant flux using a Monte Carlo approach. This involves executing a large number of random trials. We used 2, 3, 4 and 5 component thermal models to create Monte Carlo runs (i.e. random test spectra). One million such spectra were created for each thermal component model and for each library. We found the results to be stable at this number of runs (i.e. they were consistent even for different sets of random test spectra). Monte Carlo runs were created using the following constraints. Temperatures were allowed to float freely between 0 - 1100 °C although individual thermal components were forced to be at least 50 °C apart so that higher component models did not inadvertently become lower component models. Surfaces above 900 °C could occupy no more than 0.1 of a pixel and those above 700 °C no more than 0.2, so as to reflect realistic temperature distributions over volcanic targets (Wright et al. 2011). Fractional areas could float freely between 0 and 1. The sum of fractional areas was forced to be unity for the future-class test spectra but not for the current-class. Finally Monte Carlo runs for the current-class were forced to exhibit a radiance of at least  $5 \text{ W m}^{-2} \text{ sr}^{-1} \mu\text{m}^{-1}$  at a wavelength of  $2.24 \mu\text{m}$  in order to mimic the requirements of a simple anomalous pixel detection algorithm in the SWIR. The accuracy to which a library spectra were fit to a Monte Carlo run was measured using the mean absolute proportional difference (MAPD) between the two:

$$MAPD = \sum_{i=1}^n \frac{|a_i - o_i|}{a_i} \quad (5.10)$$

where  $a$  is actual radiance (i.e. the Monte Carlo run) and  $o$  is optimal radiance (i.e. the best fitting library spectra) in the  $i^{\text{th}}$  channel of a spectrum which has  $n$  wavebands in total.

## 5.7. Hyperion data processing

The Earth Observing 1 (EO-1) satellite forms part of the New Millennium Program. The Hyperion instrument on board EO-1 is the first ever orbital imaging spectrometer. It consists of VNIR and SWIR subsystems that together provide 242 channels, 196 of which are unique and calibrated. Spectral coverage ranges from 400 to 2500 nm at a resolution of 10 nm. The spatial resolution of each pixel is 30 m. The swath width of a scene is 7.7 km which translates into a nominal temporal resolution of 200 days. However, the spacecraft can be programmed to roll to various pointing angles allowing data to be acquired up to 5 times in a 16 day period. Automated acquisition requests of Hyperion data over volcanic targets can occur when activity (e.g. thermal, seismic, etc.) is detected by NASA's Volcano Sensor Web, which includes a collection of orbital and ground-based sensors (Davies et al. 2006). Radiometric quantization of Hyperion data is 12 bits and an entire image is collected in around 30 seconds. Raw digital numbers (DN) are converted into radiance using the following scale factors.

$$L_{\lambda} = \frac{DN}{40} \text{ (for Hyperion bands 1 - 70)} \quad (5.11)$$

$$L_{\lambda} = \frac{DN}{80} \text{ (for Hyperion bands 71-242)} \quad (5.12)$$

where  $L_{\lambda}$  is spectral radiance (in  $\text{W m}^{-2} \text{sr}^{-1} \mu\text{m}^{-1}$ ) and DN is the digital number in the relevant Hyperion channel.

The nine channels used to calculate radiant flux (Table 1) were selected to ensure sufficient coverage across the measured spectrum for accurate model fitting and to guarantee that at least a few unsaturated bands were available even over the hottest target surfaces. Strong atmospheric water absorption features at 1400 and 1900 nm were avoided. When calculating radiant flux saturated pixel values were automatically avoided using the flag file in the level 1 data product. All images in our dataset were acquired at night, it was therefore not necessary to correct for reflected solar radiation. The emissivity of the target surface was set to 0.95. The resulting radiance spectra were used to calculate radiant flux by finding the best match within the SWIR spectral library.

## 5.8. Results

### 5.8.1. Monte Carlo Runs

The spectral fit (i.e. MAPD) between Monte Carlo runs and the respective libraries are very good, i.e. to within 3% for the current sensor class library and 5% for the future sensor class library (Fig. 5.1). The figure shows a cumulative histogram of spectral fit for each thermal component model, i.e. 2,3,4 and 5 components, using red, green, blue and brown lines respectively. The spectral fits for the current class library are somewhat more accurate, i.e. tend to cumulate towards unity at lower MAPD values (Fig. 5.1). This is because they only have to fit the SWIR region of a spectrum whilst the future class library has to fit the SWIR, MIR and TIR regions collectively. However the spectral fit from both libraries is more accurate than the degree to which radiance can be reliably measured from space when imaging an active volcano (see discussion). Thus the accuracy of the following retrievals for radiant flux and subpixel characteristics can be considered to be at or beyond the practical detection limit of existing or near future orbital sensors.

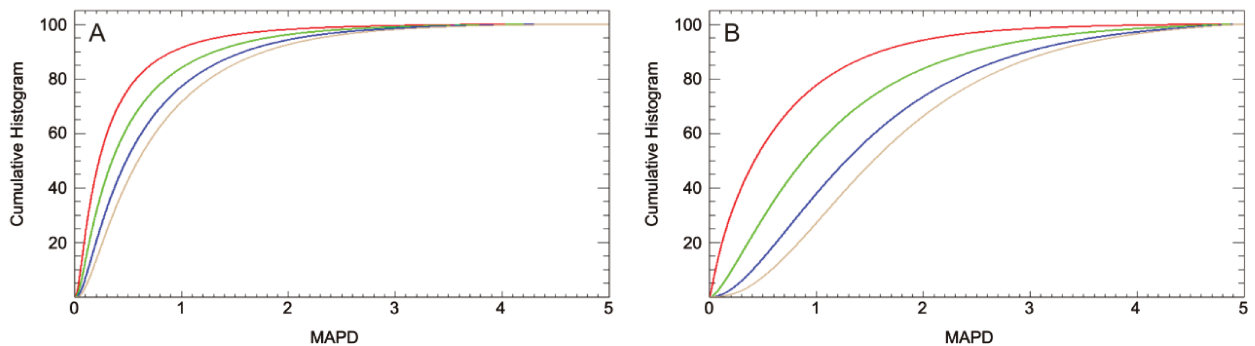


**Figure 5.1. The spectral fit of Monte Carlo runs for libraries of a) current-class sensors and b) future-class sensors. These cumulative histograms are displayed using red, green, blue and brown lines for 2, 3, 4 and 5 component Monte Carlo runs, respectively.**

Figure 5.2a shows that the radiant flux from current class of sensors can be measured to within  $\pm 20\%$ . This is an improvement over the  $\pm 30\%$  of the Wooster technique (Wooster et al. 2003). Conversely, radiant flux from future-class sensors can be measured to within  $\pm 1\%$  (Fig. 5.2b).

The dramatic increase in accuracy of the future-class sensors is due to the extra spectral information they provide.

Notably both sensor systems show that a spectral library built using a 3-component thermal model is capable of measuring radiant flux for a range of subpixel characteristics (i.e. from 2 to 5 distinct thermal components) with similar degrees of accuracy (Fig. 5.2).

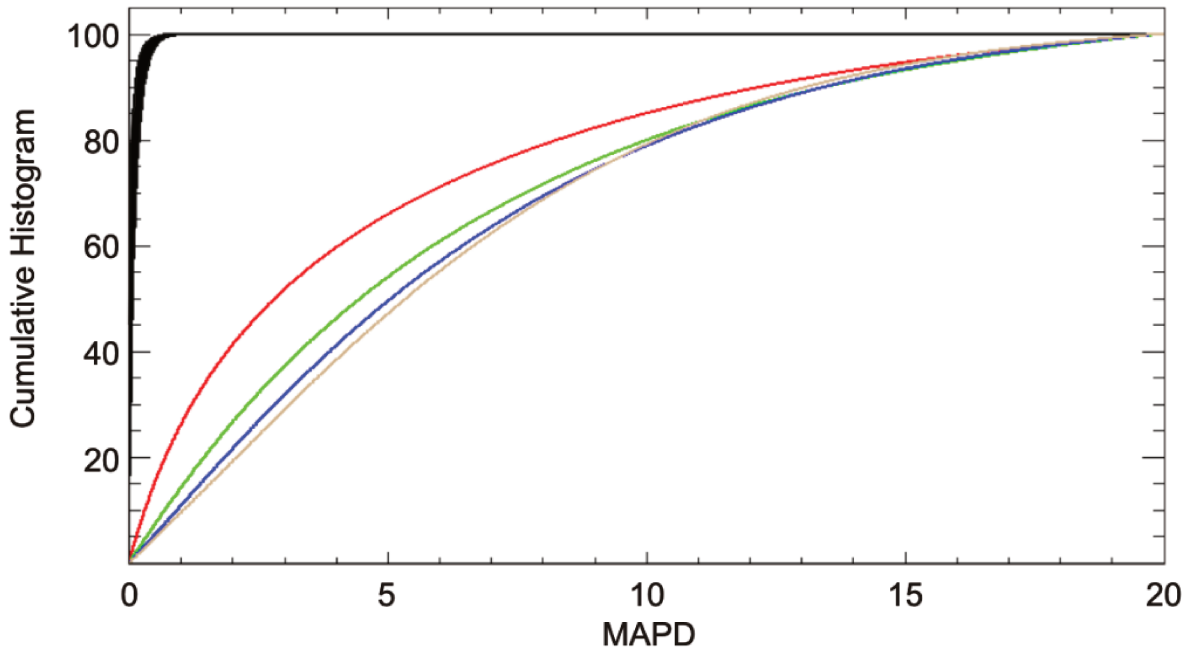


**Figure 5.2. Accuracy of radiant flux measurements. Cumulative histograms for the current-class library are shown in red, green, blue and brown for 2, 3, 4 and 5 component Monte Carlo runs, respectively. The histograms for the future-class library fit within the black region.**

The ability for the 3-component spectral libraries to accurately determine subpixel characteristics can be directly explored using the corresponding 3-component Monte Carlo runs. The accuracy of temperature retrievals for these three components, i.e. maximum, middle and minimum temperatures, are depicted using red, green and blue lines, respectively (Fig. 5.3).

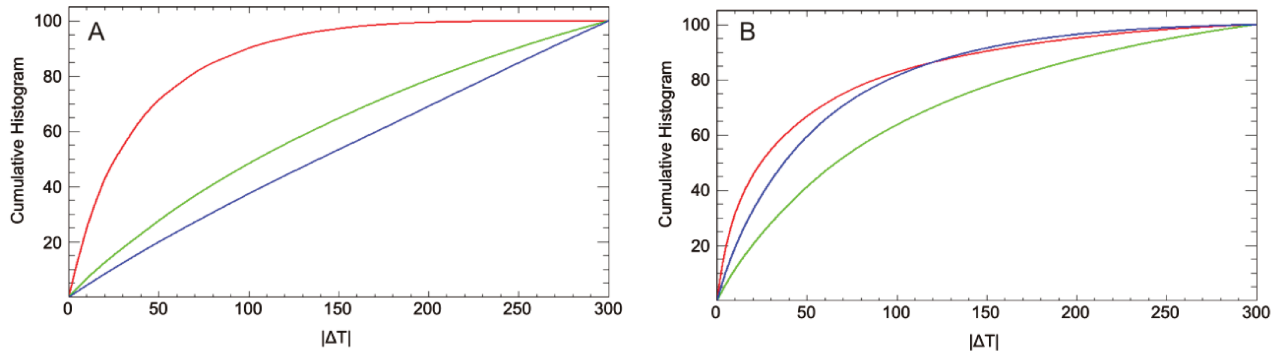


**Figure 5.3. The accuracy of subpixel temperatures characterization for a) the current-class library and b) the future-class library. These cumulative histograms display the deviation of model maximum (red), middle (green) and minimum (blue) temperatures from the actual value.**

Maximum temperatures are relatively more accurate from the current sensor library (Fig. 5.3a), i.e. they can be reliably constrained to within about 150 °C. Overall however thermal components are poorly constrained for both classes of sensor, with temperature estimates only reliably obtained to within 300 °C of the actual value for all thermal components.

The accuracy to which fractional areas can be estimated is plotted in Figure 5.4. Maximum, middle and minimum areas are depicted using red, green and blue lines respectively. Minimum fractional area estimates are somewhat more accurate for the current class of sensors. Again, however, these subpixel characteristics are poorly constrained. Fractional areas can only be reliably defined to within 40% of the pixel size for both sensor classes.

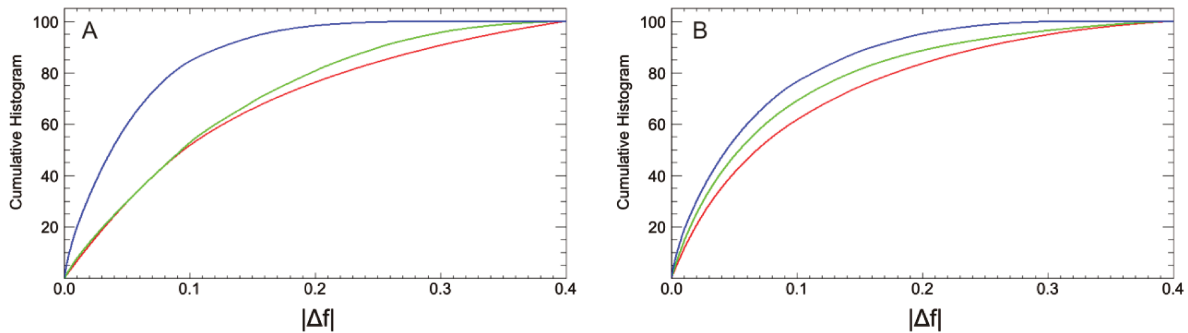


**Figure 5.4. The accuracy of subpixel fractional areas for a) the current-class library and b) the future-class library. These cumulative histograms display the deviation of model maximum (red), middle (green) and minimum (blue) fractional areas from the actual value.**

Thus unless spectral radiance can be measured and modelled to within an accuracy of greater than 3% for the current-class sensors and 5% for the future-class sensors, it is not possible to reliably measure subpixel characteristics accurately from spectral information alone. This has significant repercussions for any methodology that attempts to resolve subpixel characteristics from multispectral or hyperspectral imagery. We therefore suggest that radiant flux estimates are significantly more accurate and reliable measures of thermal volcanic activity and should be given preference over attempting to resolve subpixel characteristics.

### 5.8.2. Radiant Flux from a Lava Flow at Kliuchevskoi, Russia

Kliuchevskoi began an eruptive episode on the 15 February 2007 with the onset of Strombolian activity (BGVN 2007). Three Hyperion images were acquired during the ensuing episode on the 18 April, 22 May and 13 June 2007. Radiant flux [W] and radiant exitance [ $\text{W m}^{-2}$ ] maps were calculated from these scenes using a spectral library approach. Also provided for each scene are: total radiant flux ( $\phi_{\text{total}}$ ) in megawatts [MW], average radiant exitance (i.e.  $Q_{\text{mean}}$ ) in watts per metre squared [ $\text{W m}^{-2}$ ], and the size of thermally anomalous areas (A) in thousands of metres squared [1000's  $\text{m}^2$ ].

During this episode the volcano displayed a variety of eruptive products, including: Strombolian eruptions, lava flows on the NW and E flanks, fumarolic activity, mudflows, frequent gas-and-steam plumes as well as ash plumes (i.e. up to about 8 km in height and extending 2000 km from the volcano) and Vulcanian eruptions (Vencke 2002-).

The first scene (Fig. 5.5i) is coincident with Strombolian activity in the crater and increased fumarolic activity (BGVN 2007). It displays the maximum average radiant exitance within these scenes due to the hot, spatially limited output from fresh Strombolian activity. Thermal activity is still constrained to the active crater at this time. The second scene (Fig. 5.5ii) is concurrent with lava flow down the N flank of the volcano and shows the greatest overall radiant flux due to the relatively extensive and hot flow surface. Smaller flow fronts are visible and are orientated to the NNW and SE. This image was acquired during a phase of Vulcanian eruptions that occurred on the 11, 16 and 22-24 May. The final scene on the 13th June (Fig 5.5iii) shows the radiant flux from a different lava flow that began descending the SE flank of the

volcano on the 31 May (BGVN 2007), i.e. 2 weeks before the image was acquired. It shows the lowest average radiant exitance signifying that it was cooler than the previous flows at the time of acquisition. The axis of this flow is cooler than the margins. Strong phreatic bursts were seen from the front of the lava flow during interaction with glacial ice (BGVN 2007).

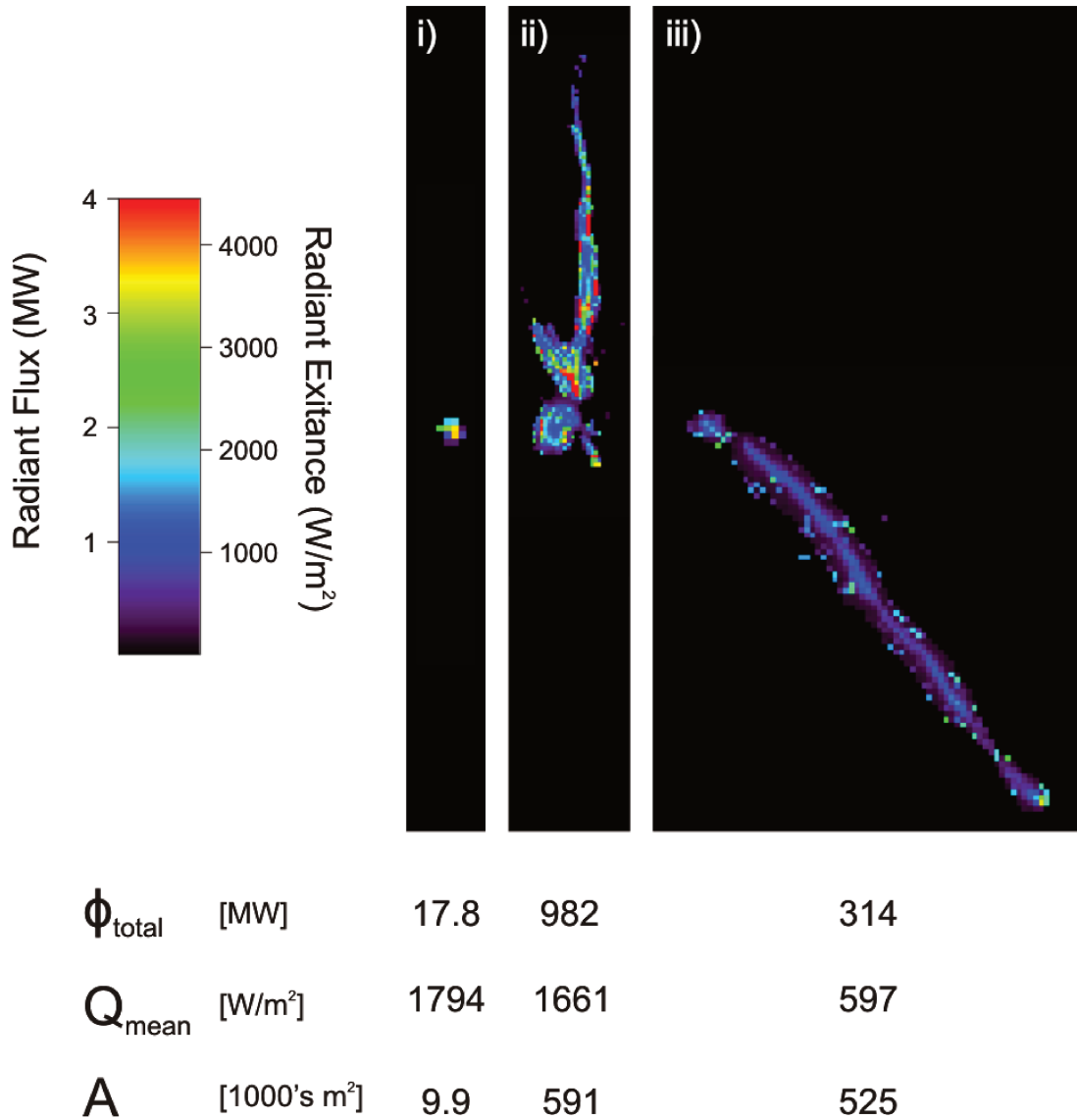


**Figure 5.5. Radiant flux from Kliuchevskoi calculated using Hyperion data acquired on i) 18 April, ii) 22 May and iii) 13 June 2007. The colour bar depicts radiant flux [MW] and equivalent radiant exitance [1000's W/m<sup>2</sup>]. The total radiant flux ( $\phi_{\text{Total}}$ , average radiant exitance ( $Q_{\text{mean}}$ ), and size of thermal anomalous area ( $A$ ) are also given. North is approximately up.**

## 5.9. Discussion

There are a number of reasons why measurements of radiance emitted from volcanoes are not perfectly accurate. They include: i) the point spread function of a detector element extending beyond the nominal pixel size of a sensor, ii) hysteresis in a sensor system along a scan line over hot target, iii) imperfect atmospheric corrections (especially in the presence of volcanic fumes and/or aerosols, as well as the difficulty in constraining reflected atmospheric irradiance in daytime scenes), iv) spectral emissivity corrections (i.e. which depend on composition and surface roughness, and therefore age of the target area, as well as wavelength and potentially temperature; furthermore emissivity might not always be homogenous at the subpixel scale), v) inaccuracies in the geolocation overlap between different wavebands, vi) the non-instantaneous amount of time over which radiance is collected, vii) sensor noise, and viii) the spectral width of individual channels. The majority of these issues apply in other applications where radiance emitted from a terrestrial target is measured from space (e.g. fire monitoring and geothermal exploration).

Therefore, although in theory a more detailed spectral library could provide a better spectral fit and therefore flux estimate, in practice it would not. This is because the model fitting accuracy already equals or exceeds the accuracy to which volcanic, geothermal or fire-based radiance can be measured from space. The reason that accurate radiant flux estimates are relatively easy to obtain whilst accurate subpixel characteristics are not is because the two require very different amounts of model fitting accuracy. Relatively small spectral differences can signify a large change in temperature or fractional area of subpixel components; whereas the corresponding change in the area under the radiance spectra will remain small.

## 5.10. Conclusion

We have shown that it is possible to use spectral libraries to calculate radiant flux from space for efficient on-the-fly processing. This method is transferable to field based or airborne sensors. The ability to reliably resolve the temperature and area of subpixel components in thermally mixed pixels would require that spectral radiance be both measured and modelled to within 3 - 5% accuracy. Given the sources of error inherent in measurements of spectral radiance from volcanic,

and other natural thermally emitting targets (e.g. fires and geothermal area), it might not be possible to ever reliably resolve subpixel characteristics using spectral information alone. Even so, it is still possible to obtain reliable flux estimates, especially when sufficient spectral coverage (e.g. SWIR, MIR and TIR channels) is available.

# Chapter 6

## Future Prospects and Conclusion

---

The principal findings from each study presented in this thesis are outlined below. After which future satellite missions that could be used to monitor thermal volcanic activity from space are described. Finally the overall conclusions derived from this work are presented.

### **6.1. Recapitulation**

Chapter 1 outlined the motivation behind this thesis, the overall objectives of the work, and the scope of what has been presented. Chapter 2 introduced the fundamental scientific principles of remote sensing from space using infrared wavelengths, described the past and present orbital imagers that can be used for this purpose and outlined the work of previous authors in the field. Issues concerning the state-of-the-art were also highlighted.

Chapter 3 explored the use of different metrics of thermal activity in ASTER scenes and how these metrics correlated to eruptive activity. This was carried out for two different volcanic targets, i.e. Erebus (Antarctica) and Láscar (Chile), using a decadal time series of images. The first metric, which was the most widely adopted by previous authors, measures the single hottest pixel temperature. It was shown that this metric produced considerable scatter at Erebus, even though radiant output from this volcano is known to be remarkably consistent. This was interpreted as being largely due to the difficulty this metric has at reliably describing small hot

features such as lava lakes. On the other hand this single hottest pixel metric was able to produce more meaningful insight at Láscaar as thermal anomalies are more spatially extensive and typically exhibit lower thermal gradients. Even so, characterizing thermal activity using a single pixel value will inevitably lack spatial information. To be able to distinguish between, for example, large cool anomalies and small hot anomalies, a new metric of thermal activity was introduced that quantifies the size of low, moderate and high temperature anomalies. This metric was more robust against subpixel effects at Erebus and provided more profound insights into thermal activity at both volcanoes, allowing new thermal precursors to be identified at Láscaar.

Thermal metrics using ASTER's TIR bands typically depend on the definition of a background temperature. It was shown that existing methods for selection of this parameter were sensitive to the slope and aspect of the volcanic edifice as well as the solar azimuth. A new method for calculating more robust background temperatures was therefore put forward. Anomalously hot TIR pixels were detected by statistically detecting an abnormal deviation above the background temperature. Thermal anomalies in ASTER SWIR bands were also identified. This aided in further constraining interpretations of eruptive activity.

Chapter 4 investigated the use of sensors with different temporal and spatial resolutions to synergistically characterize thermal volcanic activity. The MODIS and ASTER sensors were used for this purpose as both are situated on the Terra satellite and therefore provided multiple contemporary viewing opportunities. The data sets covered an 11 year time series at four distinctly different volcanoes: Erta 'Ale (Ethiopia), Kīlauea (Hawai'i), Láscaar (Chile) and Kliuchevskoi (Russia). MODIS was used to measure volcanic radiance and was able to characterize dynamic changes through time as well as to capture ephemeral events. ASTER constrained the size, shape, location and orientation of thermal anomalies and was able to detect relatively subtle thermal activity. This allowed the size and intensity of thermal anomalies to be compared for different styles of volcanism, i.e. lava lake, Hawaiian, Strombolian, Vulcanian and passive degassing. Wavelet analysis of volcanic radiance, as measured by MODIS, characterized the timescales over which individual episodes waxed and waned, as well as the repose between them.

Chapter 5 introduced a new method for calculating radiant flux from thermally mixed pixels. It was based on fitting a model to a measured radiance spectrum by finding the best match in a spectral library. The accuracy and reliability of this approach was tested using a large

collection of random, synthetic spectra (i.e. Monte Carlo runs). It was shown that model fitting accuracy was quite high (i.e. 3 - 5 %). The possibility of obtaining the size and temperature of subpixel components through model fitting was explored. It was found that neither size nor temperature could be reliably constrained, even given the model fitting accuracy. This suggests that it might not ever be possible to obtain subpixel characteristics from spectral information alone. This adds extra significance to metrics that can be obtained reliably, such as radiance, radiant flux and radiant exitance.

## 6.2. Future of infrared sensors

The future for infrared monitoring of volcanoes from space is an exciting one. National and multinational contributions will provide a greater supply of new, state-of-the-art satellite sensors. The next generation of state-funded missions of use in measuring volcanic radiance from space are summarized in Table 6.1.

**Table 6.1. Up and coming, state-funded satellites of use for infrared volcano monitoring.**

satellite sensor	High Spatial								High Temporal		
	Landsat DCM		Sentinel 2	EnMAP	ALOS - 3		HyspIRI		Sentinel 3	GCOM-C1	GOES - R
launch	OLI	TIRS			Hisui (M)	Hisui (H)	H	Thermal	SLSTR	SGLI	imager
	2013	2013	2013	2015	> 2015	> 2015	> 2018	> 2018	2013	2014	2015
pixel size (m)	15 - 30	100	10 - 60	30	5	30	60	60	500 - 1000	250 - 1000	500 - 2000
revisit (days)	16	16	2 - 5	4 - 21	30	90	19	5	0.5	2 - 3	0.5 - 15 mins
# bands	9	2	12	228	4	57	> 200	8	11	17	16
VNIR	√		√	√	√	√	√		√	√	√
SWIR	√		√	√		√	√		√	√	√
MIR								√	√		√
TIR		√						√	√	√	√
Quantization (bits)	12	12	12	14	12	12	?	?	14	12	
Latency (hours)	24	24	24 (?)	< 264	?	?	DB	DB	3	?	< 1

### 6.2.1. High Spatial Resolution Missions

The Landsat Data Continuity Mission (LDCM), which will extend the heritage of the successful Landsat series of the National Aeronautics and Space Administration (NASA), was launched successfully on 11th February 2013. The United States Geological Survey (USGS) are expected to take control of LDCM ~100 days after launch, at which point data will become available to all users at no cost. Sentinel 2, of the European Space Agency (ESA), will provide high spatial resolution datasets at remarkably high temporal resolution for its class (i.e. 5 days at the equator with up to 2 day repeat visit time when using the emergency pointing mode). The German Aerospace Centre (DLR) will launch the Environmental Mapping and Analysis Program (EnMap) which shall provide an unprecedented number of spectral bands for civilian use and have  $\pm 30^\circ$  pointing capabilities that will permit revisit times of up to 4 days. The third Advanced Land Observation Satellite (ALOS - 3) of the Japan Aerospace Exploration Agency (JAXA) will contain the Hyperspectral Imager Suite (HISUI) sensor which is seen as a follow-up to ASTER. It will contain a VNIR multispectral radiometer and a SWIR hyperspectral radiometer.

NASA plans to launch the Hyperspectral Infrared Imager (HyspIRI) mission sometime after 2020. It is being designed with volcanic applications specifically in mind and, as such, has extremely promising specifications. It is intended to include hyperspectral VSWIR monitoring capabilities geolocated to multispectral MIR and TIR bands of equal pixel size. The temporal resolution of the hyperspectral imagery will be 19 days, whilst the multispectral bands will have a 5 day temporal resolution. Data will be collected continuously during day and night and will be transmitted via direct broadcast.

### 6.2.2. High Temporal Resolution Missions

ESA will launch Sentinel 3 in 2013. This mission shall include a Sea and Land Surface Temperature Radiometer (SLSTR) which will emulate MODIS capabilities and provide imagery within 3 hours of acquisition. This minimal latency between radiance reaching the sensor and data delivery to the end-user is extremely important for real-time volcano monitoring. JAXA is in the process of executing the Global Change Observation Mission (GCOM) which

consists of two satellite series. The GCOM - C series are intended for monitoring climate change and could also prove useful for volcano monitoring given that each system will have a 250 m SWIR band, two 500 m TIR bands and 2 - 3 day visit period.

Geostationary satellite data is set to be taken to a new level with the launch of GOES - R (i.e. scheduled for 2015) which shall provide coverage of the Americas. The main Earth observation instrument on it will be the Advanced Baseline Imager (ABI), which will provide 11 more channels than previous GOES imagers, 7 of those being in MIR and TIR. It will offer a standard geostationary temporal resolution of 15 minutes for the full visible disc, 5 minutes over the continental USA and, remarkably, up to 30 seconds over regions of interest. Its spatial resolution in the IR bands will be two times higher (i.e. 2 km pixels) than previous imagers in this satellite series.

### 6.2.3. Non-Governmental Satellite Sensors

Beyond government organizations space is increasingly opening up to new areas of society. The University of Hawaii at Manoa, for example, is currently building a low cost, power efficient thermal infrared imaging spectrometer, i.e. the Thermal Hyperspectral Imager (THI), which is designed for use on board a micro-satellite bus. This will be achieved by encasing commercial off-the-shelf (COTS) products in a pressure vessel, an approach that could allow many other academic institutions to build their own satellite sensors. Private firms have been providing satellite imagery for decades of course but their cost is typically prohibitive for volcano monitoring purposes. However, it might be possible to convince some firms to acquire and share data of (at least a few) active volcanoes on a regular basis. This makes for an exciting prospect given the capabilities of some of the planned commercial satellites. For example, DigitalGlobe's WorldView-3 will provide multispectral imagery with 8 SWIR channels at a temporal resolution of 1 - 5 days and at a remarkably high spatial resolution of 3.7 m.

### 6.2.4. Unmanned Aerial Vehicles

Aerial data is set to become ever more accessible given the rise of accessible COTS unmanned aerial vehicles (UAVs). Advances in UAV technology may even make it possible to obtain continuous collection of low cost data, that is, similar to the role currently played out by satellite

imagers, but with ultrahigh resolution and less atmospheric effects. This would require automatic take off and landing capabilities and/or the ability to stay airborne for prolonged periods of time (i.e. weeks), if the high cost of consistent human interaction is to be avoided. The former could be achieved using rotor-blade powered vehicles (e.g. helicopters and quadrotors) the latter using atmospherically buoyant aircraft (e.g. blimps and balloons). Ideally UAVs would be stationed permanently at a target volcano for long time series data collection but their high mobility also makes them excellent for emergency response.

#### 6.2.5. User demand

Remote sensing data is becoming an ever greater part of everyday life. Well established websites now provide free, user-friendly volcano monitoring products (e.g. those hosted by the University of Alaska Fairbanks, [avo.images.alaska.edu](http://avo.images.alaska.edu), and the University of Hawaii at Manoa, [modis.higp.hawaii.edu](http://modis.higp.hawaii.edu)). As familiarity with such data products increases so will demand. Furthermore, given the increasing tendency for government organizations to provide satellite data at no cost to the end user, new approaches to volcano monitoring are likely to arise. For example, applications for mobile devices could provide data products (e.g. images, movies, time series, etc) directly to interested parties automatically. Increased interconnectedness through technology may stimulate further demand for research into automatic volcano monitoring systems and ever more intuitive and informative user-friendly products.

### **6.3. Conclusions**

The overall conclusions of this thesis are given below.

i) Satellites are well placed to observe thermal volcanic activity on a global basis. However, it is necessary to use multiple orbital sensors, which collectively cover all infrared wavelengths and various spatial and temporal scales, if the full range of observable volcanic thermal phenomena is to be monitored. This is because different spectral regions are better suited to imaging targets with different temperature distributions. Generally speaking, thermal infrared sensors are more sensitive to cooler targets, whilst mid infrared and shortwave infrared sensors are relatively

sensitive to hotter targets. Reliable quantitative data can only be acquired within the detection and saturation limits of a sensor, whether these limits are reached or not is in part dependent on spatial resolution. Beyond radiometric considerations, eruptive products themselves occur over extremely diverse spatial and temporal scales. Thus it is necessary to develop sensor synergies.

ii) Reliable and meaningful metrics are required to quantify thermal activity. Thermal mixing at the subpixel scale might exclude the possibility of reliable temperature retrievals given that inverse modelling of radiance spectra require a measurement reliable beyond that which can be reliably obtained from volcanic targets. Furthermore, the subpixel models required to execute this process may themselves be overly simplified representations of true surface temperature distributions. Alternative measurements such as radiance, radiant flux and exitance, which can be obtained reliably from thermally heterogeneous targets, are therefore probably superior metrics for volcano monitoring purposes and other analogous activities (e.g. the monitoring of fires and geothermal areas).

iii) Beyond measuring thermal emissions from an individual pixel it is constructive to think of thermal anomalies as groups of pixels with collective spatial characteristics. For example, quantifying the overall size of anomalous areas provides a metric that accounts for all thermally anomalous pixels, and was shown to facilitate comparisons with field reports. Advances in this direction could look to also quantify the shape, location and orientation of thermally active areas and to analyze these spatial characteristics through time. This could provide information that might help to diagnose the cause of such anomalies and the risks they may pose to people and property.

iv) One of the key aims of volcanology is to forecast hazardous events. New thermal precursors to eruptive events were identified in this thesis using infrared imagery of volcanoes. It is likely that others exist. Their discovery would be greatly facilitated by providing such data in a user-friendly format that is accessible to those who may not be remote sensing specialists. This would, for example, aid advanced time series analysis (e.g. wavelet transforms) to flourish; in turn this could be used to supplement other input data in mathematical forecasting tools (e.g. Bayesian Belief Networks).



# Capítulo 6

## Perspectivas Futuras e Conclusões

---

Uma recapitulação dos principais desenvolvimentos e conclusões específicas alcançadas nesta tese é fornecida abaixo. Adicionalmente, é fornecida uma descrição dos futuros satélites que poderão ser utilizados para o monitoramento da atividade termal de vulcões. Ao final do capítulo, serão tecidas conclusões gerais derivadas do trabalho como um todo.

### **6.1. Recapitulação**

No Capítulo 1 foram apresentadas as motivações da pesquisa de doutorado, assim como o escopo e os objetivos gerais da tese. No Capítulo 2 foram abordados os princípios científicos fundamentais de sensoriamento remoto utilizando comprimentos de onda do infravermelho. Foram ainda descritos os principais sensores orbitais, desativados e em operação, utilizados para detecção de radiação eletromagnética infravermelha, incluindo sínteses sobre contribuições extraídas da literatura quanto à aplicação desses dados em estudos sobre vulcões.

No Capítulo 3 explorou-se o uso de diferentes métricas de atividade térmica em cenas ASTER e como essas métricas estão correlacionadas à atividade eruptiva. Este trabalho foi realizado para dois diferentes alvos vulcânicos, i.e. Erebus (Antártica) e Láscar (Chile),

utilizando uma série temporal de imagens adquiridas ao longo de uma década. A primeira métrica, amplamente adotada na literatura, mede a temperatura mais quente de um pixel individual. Quando aplicada ao Erebus, um vulcão conhecido por um padrão termal notavelmente consistente, esta métrica produziu uma dispersão considerável devido, em grande parte, à sua dificuldade em caracterizar pequenos corpos quentes, como lagos de lava. Por outro lado, essa métrica do pixel mais quente foi mais eficaz na caracterização da atividade no vulcão Láscar visto que, neste alvo, as anomalias térmicas são espacialmente mais extensas e apresentam menores gradientes térmicos. Mesmo assim, a caracterização da atividade termal utilizando-se um valor de pixel, inevitavelmente, ocasionará a falta de informação espacial. Para abordar esse assunto e ser capaz, por exemplo, de distinguir entre grandes anomalias relativamente frias e pequenas anomalias relativamente quentes, uma nova métrica de atividade térmica foi introduzida quantificando o tamanho de anomalias de áreas com temperatura baixa, moderada e alta. Esta métrica foi mais robusta contra efeitos de subpixel e forneceu informações mais consistentes sobre a atividade térmica em ambos os vulcões, permitindo que novos precursores térmicos fossem identificados no vulcão Láscar.

Métricas térmicas que utilizam bandas TIR do sensor ASTER tipicamente dependem da definição de uma temperatura de *background*. No Capítulo 3 ficou demonstrado que os métodos existentes para a seleção dessa temperatura são sensíveis à inclinação e aspecto do edifício vulcânico, bem como ao azimute solar. Um novo método para calcular as temperaturas de *background* foi desenvolvido. Pixels com assinaturas anormalmente quentes nas imagens das bandas TIR do ASTER foram detectados por apresentarem um desvio, estatisticamente anormal, acima da temperatura de *background*. Anomalias térmicas nas imagens das bandas SWIR foram também identificadas, o que auxiliou numa melhor interpretação da atividade eruptiva.

No Capítulo 4 investigou-se a utilização de sensores com diferentes resoluções temporais e espaciais para sinergisticamente caracterizar a atividade vulcânica térmica. Os sensores MODIS e ASTER, ambos do satélite Terra, foram utilizados para este fim, fornecendo múltiplas aquisições contemporâneas. Os dados cobriram uma série temporal de 11 anos, considerando-se quatro vulcões distintos: Erta ‘Ale (Etiópia), Kīlauea (Havaí), Láscar (Chile) e Kliuchevskoi (Rússia). Os dados do MODIS foram utilizados para medir a radiação vulcânica e caracterizar mudanças dinâmicas ao longo do tempo, bem como para capturar eventos efêmeros. Os dados do ASTER permitiram a delimitação do tamanho, forma, localização e orientação de anomalias

térmicas, incluindo a detecção de atividades térmicas relativamente sutis. Isso possibilitou a comparação do tamanho e intensidade de anomalias térmicas em diferentes estilos de vulcanismo, ou seja, em um lago de lava, em erupções do tipo havaiano e estromboliano, e em situações de desgaseificação passiva. A radiância emitida pelos vulcões e medida pelo sensor MODIS foi submetida a análise pelo método de *wavelets*, o que permitiu a caracterização dos períodos de tempo em que a atividade vulcânica cresceu e diminuiu em eventos individuais, assim como os períodos de quiescência vulcânica.

O capítulo 5 introduz uma nova metodologia para calcular fluxo radiante de pixels termalmente heterogênicos que foi baseado na modelagem de espectros de radiância através de uma biblioteca espectral. A precisão e confiabilidade desta abordagem foi analisada utilizando uma vasta coleção de espectros sintéticos (i.e. espectros Monte Carlo). Os modelos produzidos tiveram alta precisão (i.e. 3 - 5 %). Também foi estudada a possibilidade de obter o tamanho e temperatura dos componentes *subpixel* através de modelagem. Os resultados mostram que o tamanho e temperatura não poderiam ser confiavelmente determinados mesmo com nível de precisão obtido pela modelagem. Este resultado sugere que não é possível obter características *subpixel* somente através de informação espectral.

## **6.2. Futuros Sensores Infravermelhos**

O futuro do monitoramento dos vulcões por sensores operando no infravermelho a bordo de plataformas orbitais é bastante animador. Contribuições uninacionais e multinacionais irão proporcionar um número cada vez maior de satélites com melhor configuração e desempenho em relação aos seus antecessores. Uma síntese da próxima geração de missões financiadas por órgãos governamentais de vários países é apresentada na Tabela 1.

### 6.2.1. Missões de alta resolução espacial e espectral

O *Landsat Data Continuity Mission* (LDCM), que sucederá série Landsat do *National Aeronautics and Space Administration* (NASA), foi lançado no dia 11 de fevereiro de 2013. O *United States Geological Survey* (USGS) assumirá o controle do LDCM em cerca de 100 dias após a decolagem, a partir de quando os dados estarão disponíveis sem custo para todos os usuários. O satélite

Sentinel 2, com lançamento previsto para 2013 pela Agência Espacial Europeia (ESA), deve oferecer imagens de alta resolução espacial (10 a 60 m), com alta resolução temporal para a sua classe (i.e. 5 dias no equador em modo normal; e 2 dias utilizando o modo de emergência). O Centro Aeroespacial Alemão (DLR) deve lançar até 2015 o *Environmental Mapping and Analysis Program* (EnMap) - um sensor hiperespectral que fornecerá o maior número de bandas espectrais para uso civil futuro e com capacidade de apontamento de  $\pm 30^\circ$ , permitindo a revisita de um alvo em até 4 dias. O terceiro *Advanced Land Observation Satellite* (ALOS - 3) da Agência de Exploração Aeroespacial do Japão (JAXA) conterà o *Hyperspectral Imager Suite* (HISUI), um sensor visto como uma espécie de continuação do sensor ASTER, com um radiômetro multiespectral no VNIR e um radiômetro hiperespectral no SWIR.

**Tabela 1. Satélites futuros para monitoramento de vulcões na faixa espectral do infravermelho.**

satélite sensor	Alta Resolução Espacial				Alta Resolução Temporal						
	Landsat DCM		Sentinel 2	EnMAP	ALOS - 3		HyspIRI		Sentinel 3	GCOM-C1	GOES - R
	OLI	TIRS			Hisui (M)	Hisui (H)	H	Thermal	SLSTR	SGLI	imager
launch	2013	2013	2013	2015	> 2015	> 2015	> 2018	> 2018	2013	2014	2015
pixel (m)	15 - 30	100	10 - 60	30	5	30	60	60	500 - 1000	250 - 1000	500 - 2000
revisit (days)	16	16	2 - 5	4 - 21	30	90	19	5	0.5	2 - 3	0.5 - 15 <u>mins</u>
# bands	9	2	12	228	4	57	> 200	8	11	17	16
VNIR	√		√	√	√	√	√		√	√	√
SWIR	√		√	√		√	√		√	√	√
MIR									√		√
TIR		√						√	√	√	√
Quantização (bits)	12	12	12	14	12	12	?	?	14	12	
Latência (hours)	24	24	24 (?)	< 264	?	?	DB	DB	3	?	< 1

A NASA planeja lançar o *Hyperspectral Infrared Imager* (HyspIRI) em algum momento em torno de 2020. Este sensor está sendo concebido para múltiplas aplicações em Geociências, incluindo monitoramento de vulcões, e compreende especificações extremamente promissoras. Pretende-se incluir um imageador hiperespectral no VSWIR, o qual produzirá imagens co-registráveis a outras produzidas por uma suíte de sensores multiespectrais no MIR e TIR, com o mesmo tamanho de pixel. A resolução temporal do imageador hiperespectral será de 19 dias enquanto do sensor multiespectral será de 5 dias. Os dados serão coletados continuamente durante o dia e noite.

### 6.2.2. Missões de alta resolução temporal

A ESA lançará a plataforma Sentinel 3 em 2013. Esta missão deve incluir o *Sea and Land Surface Temperature Radiometer* (SLSTR), que emulará as capacidades do MODIS, fornecendo imagens-produto em até 3 horas após a aquisição. Esta latência mínima entre a radiância atingindo o sensor e a entrega dos dados é extremamente importante para monitoramento de vulcões em tempo real.

A JAXA está em processo de execução do *Global Change Observation Mission* (GCOM), que consiste de duas séries de satélites. Um deles, o GCOM - C, será destinado ao monitoramento de mudanças climáticas e também poderá ser útil ao monitoramento de vulcões, visto que cada sistema terá um banda no SWIR com pixels de 250 m e um período de visita de 2 a 3 dias.

Dados de satélite geoestacionários também deverão ser alçados a um novo patamar com o lançamento do *Geostationary Operational Environmental Satellite* - série R (GOES - R), previsto para 2015, que fornecerá cobertura das Américas. O instrumento principal de observação da Terra será a *Advanced Baseline Imager* (ABI), que oferecerá 11 canais a mais do que as missões GOES precedentes, 7 dos quais posicionados em comprimentos de onda do MIR e TIR. O ABI oferecerá uma resolução temporal padrão de 15 minutos para as Américas como um todo; 5 minutos sobre o Estados Unidos e até 30 segundos sobre regiões de interesse. Sua resolução espacial nas bandas do infravermelho será duas vezes mais alta (i.e. 2 km por pixel) do que sensores anteriores da série GOES.

### 6.2.3. Sensores não-governamentais

Além das missões de organizações governamentais previstas, a exploração espacial será cada vez mais aberta para iniciativas na área acadêmica e comercial. A Universidade do Havaí, em Manoa, por exemplo, está construindo um espectrômetro de baixo custo, com cobertura no infravermelho termal, denominado de *Thermal Hyperspectral Imager* (THI), o qual está sendo projetado para uso a bordo de um micro-satélite. Esse objetivo será alcançado utilizando-se peças e produtos comerciais (COTS) prontos e semi-prontos, os quais serão montados numa câmara de vácuo. Esse tipo de abordagem pode permitir que outras instituições acadêmicas construam seus

próprios sensores orbitais. Empresas privadas têm fornecido imagens de satélite por décadas, entretanto, o seu custo é normalmente proibitivo para fins de monitoramento de vulcões. Atualmente há esforços no sentido de convencer algumas empresas a adquirir e compartilhar dados de pelo menos alguns vulcões ativos de uma forma consistente. Este é uma possibilidade animadora por causa das capacidades dos satélites comerciais sendo desenvolvidos. Por exemplo, o *WorldView-3* da *DigitalGlobe* fornecerá imagens multiespectrais com oito bandas no SWIR e uma resolução temporal de 1 a 5 dias, além de uma alta resolução espacial de 3,7 m.

#### 6.2.4. Veículos Aéreos Não Tripulados (VANTs)

Dados aéreos estão prestes a se tornar cada vez mais acessíveis, dado o aumento de acessibilidade de veículos aéreos não tripulados (VANTs). Avanços na tecnologia VANT podem proporcionar dados adquiridos de forma contínua e de baixo custo, ou seja, semelhante aos satélites, mas com resolução espacial superior e efeitos atmosféricos minimizados. Em geral, a operação humana de novas tecnologias é de alto custo. Para minimizar esta dependência, os VANTs exigiriam decolagem e aterrissagem automáticas (a partir de helicópteros comuns e helicópteros quadrotores) e/ou a capacidade de permanecer no ar por períodos prolongados de tempo (i.e. semanas) (a partir de plataformas flutuantes na atmosfera). Idealmente, os VANTs seriam estacionados permanentemente em um vulcão para obter dados ao longo tempo, mas a sua alta mobilidade também os tornaria excelentes para responder a emergências.

#### 6.2.5. Demanda do usuário

Dados de sensoriamento remoto estão se tornando uma parte cada vez maior da vida cotidiana. Sites bem estabelecidos já fornecem produtos de monitoramento de vulcões num formato simples e sem custos (por exemplo, aqueles hospedado pela Universidade de Alaska Fairbanks ([avo.images.alaska.edu](http://avo.images.alaska.edu)) e da Universidade do Haváí ([modis.higp.hawaii.edu](http://modis.higp.hawaii.edu))). A familiaridade com estes produtos somente tende a aumentar e, por consequência, também a demanda. Além disso, dada a intenção crescente de organizações governamentais em fornecer dados de satélite sem custo ao usuário final, novas abordagens para monitoramento de vulcões provavelmente surgirão. Por exemplo, aplicativos para dispositivos móveis (ex. *smart phones* e *tablets*)

poderiam fornecer produtos (ex. imagens, filmes, séries de tempo, etc) direta e automaticamente aos interessados. O aumento da interconectividade também deve estimular ainda mais a demanda para a pesquisa em sistemas de monitoramento automático de vulcões, e para produtos cada vez mais intuitivos e informativos.

### **6.3. Conclusões**

As conclusões desta tese são apresentadas a seguir.

i) Para caracterizar a gama completa dos fenômenos exibidos pelos vulcões é necessário observá-los em várias escalas espaciais e temporais e todos os comprimentos de onda do infravermelho. Esta necessidade surge do fato que produtos de erupções têm uma variação enorme em tamanho, aproximadamente entre 1 e 1.000.000 metros, e podem se manifestar em períodos de tempo que variam de minutos a meses. Ademais, a radiação emitida por tais produtos é fortemente dependente da temperatura dos mesmos. Para garantir que a atividade vulcânica seja imageada dentro dos limites de detecção e saturação de pelo menos um dos canais espectrais, é essencial observar tal atividade em vários comprimentos de onda no infravermelho. É por isso que o desenvolvimento de sinergias entre diversos sensores é crucial.

ii) A heterogeneidade termal na escala de um pixel provavelmente exclui a possibilidade de calcular a temperatura de alvos vulcânicos com confiança pelos seguintes motivos: 1) medidas de radiação não podem ser obtidas com o grau suficiente de precisão e 2) os modelos que formam a base do cálculo da temperatura tendem a ser simples demais e, portanto, não representam a distribuição verdadeira da temperatura superficial. Medidas alternativas como radiação, fluxo radiante e excitância, que podem ser obtidas confiavelmente mesmo em superfícies termalmente heterogêneas, são portanto mais adequadas para o monitoramento de vulcões e outras atividades análogas (ex., monitoramento de incêndios e áreas geotermiais).

iii) Além de quantificar atividade termal em pixels individuais é útil tratar tal atividade como conjuntos de pixels com características espaciais coletivas. Por exemplo, quantificar o tamanho de áreas termalmente ativas facilita comparações com atividade observada em campo. Novos

avanços neste assunto poderiam incluir a quantificação da forma, localização e orientação de áreas que são termalmente ativas e a análise das mudanças nestas características espaciais no tempo. Informações sobre o comportamento de atividade termal no espaço e no tempo podem ajudar a diagnosticar os processos vulcânicos por trás destas atividades e a interpretação dos riscos que elas trazem.

iv) Um dos objetivos principais do estudo de vulcões é a previsão de erupções. Esta tese identificou novos precursores à atividade vulcânica utilizando imagens do infravermelho. É provável que outros precursores existam. A sua descoberta seria facilitada com o acesso de tais imagens em um formato amigável para quem não seja necessário um especialista em sensoriamento remoto. O fornecimento de dados processados pode ser feito de forma automatizada com as metodologias desenvolvidas neste trabalho de doutorado. A distribuição gratuita de dados processados para qualquer pessoa interessada poderia ajudar em avanços, por exemplo, na análise de séries de tempo (ex. através *wavelets*) o que, por sua vez, permitiria contribuir na previsão de erupções.

## References

---

Bulletin of the Global Volcanism Network. Lásca. 2000. 25 (6).

Bulletin of the Global Volcanism Network. Lásca. 2003. 28 (3).

Bulletin of the Global Volcanism Network. Lásca. 2004. 29 (1).

Bulletin of the Global Volcanism Network. Lásca. 2005. 30 (5).

Bulletin of the Global Volcanism Network. Lásca. 2006. 31 (4).

Bulletin of the Global Volcanism Network. Lásca. 2007. 32 (9).

Bulletin of the Global Volcanism Network. Kilauea. 2010. 35 (01): 10

Bulletin of the Global Volcanism Network. Kliuchevskoi. 2007. 32 (6)

Bulletin of the Global Volcanism Network. Kliuchevskoi. 2009. 34 (3)

Bulletin of the Global Volcanism Network. Kliuchevskoi. Weekly Reports, 3-9 November 2010.

Bulletin of the Global Volcanism Network. Soufrière Hills. 1995. 20 (6).

Amelung, F., Jonsson, S., Zebker, H., and Segall, P., 2000, Widespread uplift and 'trapdoor' faulting on Galapagos volcanoes observed with radar interferometry: *Nature*, v. 407, p. 993-996.

- Blackett, M., and Wooster, M.J., 2011, Evaluation of SWIR-based methods for quantifying active volcano radiant emissions using NASA EOS-ASTER data: *Geomatics, Natural Hazards and Risk*, v. 2, p. 51-78.
- Boichu, M., Oppenheimer, C., Tsanev, V., and Kyle, P.R., 2010, High temporal resolution SO<sub>2</sub> flux measurements at Erebus volcano, Antarctica: *Journal of Volcanology and Geothermal Research*, v. 190, p. 325-336.
- Calkins, J., Oppenheimer, C., and Kyle, P.R., 2008, Ground-based thermal imaging of lava lakes at Erebus volcano, Antarctica: *Journal of Volcanology and Geothermal Research*, v. 177, p. 695-704.
- Carter, A.J., Girina, O., Ramsey, M.S., and Demyanchuk, Y.V., 2008, ASTER and field observations of the 24 December 2006 eruption of Bezymianny Volcano, Russia: *Remote Sensing of Environment*, v. 112, p. 2569-2577.
- Carter, A.J., and Ramsey, M.S., 2009, ASTER- and field-based observations at Bezymianny Volcano: Focus on the 11 May 2007 pyroclastic flow deposit: *Remote Sensing of Environment*, v. 113, p. 2142-2151.
- Chien, S., 2009, Onboard Science Processing Concepts for the HypSIRI Mission: *Intelligent Systems, IEEE*, v. 24, p. 12-19.
- Chrétien, S., and Brousse, R., 1989, Events preceding the great eruption of 8 May, 1902 at Mount Pelée, Martinique: *Journal of Volcanology and Geothermal Research*, v. 38, p. 67-75.
- Coppola, D., Piscopo, D., Laiolo, M., Cigolini, C., Delle Donne, D., and Ripepe, M., 2012, Radiative heat power at Stromboli volcano during 2000-2011: Twelve years of MODIS observations: *Journal of Volcanology and Geothermal Research*, v. 215, p. 48-60.
- Csatho, B., Schenk, T., Kyle, P., Wilson, T., and Krabill, W.B., 2008, Airborne laser swath mapping of the summit of Erebus volcano, Antarctica: Applications to geological mapping of a volcano: *Journal of Volcanology and Geothermal Research*, v. 177, p. 531-548.

- Dash, P., Gottsche, F.M., Olesen, F.S., and Fischer, H., 2002, Land surface temperature and emissivity estimation from passive sensor data: theory and practice-current trends: *International Journal of Remote Sensing*, v. 23, p. 2563-2594.
- Davies, A.G., Calkins, J., Scharenbroich, L., Vaughan, R.G., Wright, R., Kyle, P., Castano, R., Chien, S., and Tran, D., 2008, Multi-instrument remote and in situ observations of the Erebus Volcano (Antarctica) lava lake in 2005: A comparison with the Pele lava lake on the jovian moon Io: *Journal of Volcanology and Geothermal Research*, v. 177, p. 705-724.
- Davies, A.G., Chien, S., Baker, V., Doggett, T., Dohm, J., Greeley, R., Ip, F., Castano, R., Cichy, B., Rabideau, G., Tran, D., and Sherwood, R., 2006, Monitoring active volcanism with the autonomous sciencecraft experiment on EO-1: *Remote Sensing of Environment*, v. 101, p. 427-446.
- De Silva, S.L., and Francis, P.W., 1991, *Volcanoes of the Central Andes*, Springer-Verlag.
- Dean, K., 1996, Monitoring volcanoes in the North Pacific region using satellite imagery, modelling and meteorological data, *Pan Pacific Hazards Conference: Vancouver*, p. 1-29.
- Dean, K., Servilla, M., Roach, A., Foster, B., and Engle, K., 1998, Satellite monitoring of remote volcanoes improves study efforts in Alaska: *Eos Transactions*, v. 79, p. 413-423.
- Denniss, A.M., Harris, A.J.L., R.W., C., Francis, P.W., and Rothery, D.A., 1996, The 1993 Lascar pyroclastic flow imaged by JERS-1.: *International Journal of Remote Sensing*, v. 17, p. 1975-1980.
- Donegan, S.J., and Flynn, L.P., 2004, Comparison of the response of the landsat 7 enhanced thematic mapper plus and the earth observing-1 advanced land imager over active lava flows: *Journal of Volcanology and Geothermal Research*, v. 135, p. 105-126.
- Dozier, J., 1981, A method for satellite identification of surface-temperature fields of subpixel resolution: *Remote Sensing of Environment*, v. 11, p. 221-229.
- Esser, R.P., Kyle, P.R., and McIntosh, W.C., 2004, Ar-40/Ar-39 dating of the eruptive history of Mount Erebus, Antarctica: volcano evolution: *Bulletin of Volcanology*, v. 66, p. 671-686.

- Fialko, Y., and Simons, M., 2001, Evidence for on-going inflation of the Socorro magma body, New Mexico, from interferometric synthetic aperture radar imaging: *Geophysical Research Letters*, v. 28, p. 3549-3552.
- Flynn, L.P., Harris, A.J.L., Rothery, D.A., and Oppenheimer, C., 2000, High spatial resolution thermal remote sensing of active volcanic features using Landsat and hyperspectral data, *in* Mouginis-Mark, P., Crisp, J.A., and Fink, J.H., eds., *Remote Sensing of Active Volcanism*, Volume 116: Washington, DC, American Geophysical Union, p. 161-177.
- Flynn, L.P., Harris, A.J.L., and Wright, R., 2001, Improved identification of volcanic features using Landsat 7 ETM+: *Remote Sensing of Environment*, v. 78, p. 180-193.
- Flynn, L.P., Mouginismark, P.J., Gradie, J.C., and Lucey, P.G., 1993, Radiative temperature measurements at Kupaianaha lava lake, Kilauea volcano, Hawaii: *Journal of Geophysical Research-Solid Earth*, v. 98, p. 6461-6476.
- Flynn, L.P., Mouginismark, P.J., and Horton, K.A., 1994, Distribution of thermal areas on an active lava flow field - Landsat observations of Kilauea, Hawaii, July 1991: *Bulletin of Volcanology*, v. 56, p. 284-296.
- Francis, P.W., and Rothery, D.A., 1987, Using the Landsat Thematic Mapper to detect and monitor active volcanoes: An example from northern Chile: *Geology*, v. 15, p. 614-617.
- Fukushima, Y., Cayol, V., and Durand, P., 2005, Finding realistic dike models from interferometric synthetic aperture radar data: The February 2000 eruption at Piton de la Fournaise: *Journal of Geophysical Research-Solid Earth*, v. 110.
- Garratt, J.R., 1992, Extreme Maximum Land Surface Temperatures: *Journal of Applied Meteorology*, v. 31, p. 1096-1105.
- Gawarecki, S.J.L., R. J. P.; Nordberg, W., 1965, Infrared spectral returns and imagery of the earth from space and their application to geologic problems., *Science and Technology Series - American Astronomical Society, NASA*, p. 13-33.
- Giggenbach, W.F., Kyle, P.R., and Lyon, G.L., 1973, Present Volcanic Activity on Mount Erebus, Ross Island, Antarctica: *Geology*, v. 1, p. 135-136.

- Giglio, L., Descloitres, J., Justice, C.O., and Kaufman, Y.J., 2003, An enhanced contextual fire detection algorithm for MODIS: *Remote Sensing of Environment*, v. 87, p. 273-282.
- Giglio, L., and Kendall, J.D., 2001, Application of the Dozier retrieval to wildfire characterization - A sensitivity analysis: *Remote Sensing of Environment*, v. 77, p. 34-49.
- Gillespie, A., Rokugawa, S., Matsunaga, T., Cothorn, J.S., Hook, S., and Kahle, A.B., 1998, A temperature and emissivity separation algorithm for Advanced Spaceborne Thermal Emission and Reflection Radiometer (ASTER) images: *Ieee Transactions on Geoscience and Remote Sensing*, v. 36, p. 1113-1126.
- Glaze, L., 1989, Measuring thermal budgets of active 639 volcanoes by satellite remote sensing: *Nature*, v. 338, p. 144-146.
- Harpel, C.J., Kyle, P.R., Esser, R.P., McIntosh, W.C., and Caldwell, D.A., 2004, Ar-40/Ar-39 dating of the eruptive history of Mount Erebus, Antarctica: summit flows, tephra, and caldera collapse: *Bulletin of Volcanology*, v. 66, p. 687-702.
- Harris, A.J.L., Flynn, L.P., Keszthelyi, L., Mougini-Mark, P.J., Rowland, S.K., and Resing, J.A., 1998, Calculation of lava effusion rates from Landsat TM data: *Bulletin of Volcanology*, v. 60, p. 52-71.
- Harris, A.J.L., Keszthelyi, L., Flynn, L.P., Mougini-Mark, P.J., Thornber, C., Kauahikaua, J., Sherrod, D., Trusdell, F., Sawyer, M.W., and Flament, P., 1997, Chronology of the episode 54 eruption at Kilauea Volcano, Hawaii, from GOES-9 satellite data: *Geophysical Research Letters*, v. 24, p. 3281-3284.
- Harris, A.J.L., Wright, R., and Flynn, L.P., 1999, Remote monitoring of Mount Erebus volcano, Antarctica, using polar orbiters: Progress and prospects: *International Journal of Remote Sensing*, v. 20, p. 3051-3071.
- Hirn, B., Di Bartola, C., and Ferrucci, F., 2008, Spaceborne Monitoring 2000-2005 of the Pu'u 'O'o-Kupaianaha (Hawaii) Eruption by Synergetic Merge of Multispectral Payloads ASTER and MODIS: *Ieee Transactions on Geoscience and Remote Sensing*, v. 46, p. 2848-2856.

- Hook, S., and Oaida, B., 2010, NASA 2009 HypSIRI Science Workshop Report, JPL Publication: Pasadena, CA, Jet Propulsion Laboratory, National Aeronautics and Space Administration.
- Hooper, A., Prata, F., and Sigmundsson, F., 2012, Remote Sensing of Volcanic Hazards and Their Precursors: Proceedings of the Ieee, v. 100, p. 2908-2930.
- Jonsson, S., Zebker, K., Cervelli, P., Segall, P., Garbeil, H., Mougini-Mark, P., and Rowland, S., 1999, A shallow-dipping dike fed the 1995 flank eruption at Fernandina Volcano, Galapagos, observed by satellite radar interferometry: Geophysical Research Letters, v. 26, p. 1077-1080.
- Kelly, P.J., Kyle, P.R., Dunbar, N.W., and Sims, K.W.W., 2008, Geochemistry and mineralogy of the phonolite lava lake, Erebus volcano, Antarctica: 1972-2004 and comparison with older lavas: Journal of Volcanology and Geothermal Research, v. 177, p. 589-605.
- Kervyn, M., Ernst, G.G.J., Harris, A.J.L., Belton, F., Mbede, E., and Jacobs, P., 2008, Thermal remote sensing of the low-intensity carbonatite volcanism of Oldoinyo Lengai, Tanzania: International Journal of Remote Sensing, v. 29, p. 6467-6499.
- Koeppen, W.C., Pilger, E., and Wright, R., 2011, Time series analysis of infrared satellite data for detecting thermal anomalies: a hybrid approach: Bulletin of Volcanology, v. 73, p. 577-593.
- Krueger, A.J., 1983, Sighting of El Chicon Sulfur Dioxide clouds with the NIMBUS-7 Total Ozone Mapping Spectrometer: Science, v. 220, p. 1377-1379.
- Kyle, P.R., Moore, J.A., and Thirlwall, M.F., 1992, Petrologic Evolution of Anorthoclase Phonolite Lavas at Mount Erebus, Ross Island, Antarctica: Journal of Petrology, v. 33, p. 849-875.
- Lombardo, V., Buongiorno, M.F., and Amici, S., 2006, Characterization of volcanic thermal anomalies by means of sub-pixel temperature distribution analysis: Bulletin of Volcanology, v. 68, p. 641-651.

- Lu, Z., Wicks, C., Dzurisin, D., Thatcher, W., Freymueller, J.T., McNutt, S.R., and Mann, D., 2000, Aseismic inflation of Westdahl volcano, Alaska, revealed by satellite radar interferometry: *Geophysical Research Letters*, v. 27, p. 1567-1570.
- Marzocchi, W., Sandri, L., and Selva, J., 2008, BET\_EF: a probabilistic tool for long- and short-term eruption forecasting: *Bulletin of Volcanology*, v. 70, p. 623-632.
- Marzocchi, W., and Zaccarelli, L., 2006, A quantitative model for the time-size distribution of eruptions: *Journal of Geophysical Research-Solid Earth*, v. 111.
- Matson, M., and Dozier, J., 1981, Identification of subresolution high temperature sources using a thermal IR sensor: *Photogrammetric Engineering and Remote Sensing*, v. 47, p. 1311-1318.
- Matthews, S.J., Gardeweg, M.C., and Sparks, R.S.J., 1997, The 1984 to 1996 cyclic activity of Lascar volcano, northern Chile: cycles of dome growth, dome subsidence, degassing and explosive eruptions: *Bulletin of Volcanology*, v. 59, p. 72-82.
- Matthews, S.J., Jones, A.P., and Gardeweg, M.C., 1994, Láscar volcano, Northern Chile; Evidence for steady-state disequilibrium: *Journal of Petrology*, v. 35, p. 401-432.
- Miller, T.P., and Casadevall, T.J., 2000, Volcanic Ash Hazards to Aviation, *in* Sigurdsson, H., ed., *Encyclopedia of Volcanoes*, Academic Press, p. 915-930.
- Mouginis-Mark, P. and Domergue-Schmidt, N., 2000. Acquisition of Satellite Data for Volcano Studies. In: P. Mouginis-Mark, J.A. Crisp and J.H. Fink (Editors), *Remote Sensing of Active Volcanism*. American Geophysical Union, Washington, DC, pp. 9-24.
- Murphy, S.W., de Souza Filho, C.R., and Oppenheimer, C., 2011, Monitoring volcanic thermal anomalies from space: Size matters: *Journal of Volcanology and Geothermal Research*, v. 203, p. 48-61.
- Murphy, S.W., Wright, R., Oppenheimer, C. and Filho, C.R.S., 2013. MODIS and ASTER synergy for characterizing thermal volcanic activity. *Remote Sensing of Environment*, 131(0): 195-205.

- Nakada, S., 2000, Hazards from pyroclastic flows and surges, *in* Sigurdsson, H., ed., Encyclopedia of Volcanoes, Academic Press, p. 945 - 955.
- Oppenheimer, C., 1991, Lava flow cooling estimated from Landsat Thematic Mapper infrared data - The Lonquimay eruption (Chile, 1989): Journal of Geophysical Research-Solid Earth, v. 96, p. 21865-21878.
- Oppenheimer, C., 1993, Thermal distributions of hot volcanic surfaces constrained using 3 infrared bands of remote-sensing data: Geophysical Research Letters, v. 20, p. 431-434.
- Oppenheimer, C., Francis, P.W., Rothery, D.A., Carlton, R.W.T., and Glaze, L.S., 1993a, Infrared image analysis of volcanic thermal features - Lascar Volcano, Chile, 1984-1992: Journal of Geophysical Research-Solid Earth, v. 98, p. 4269-4286.
- Oppenheimer, C., Rothery, D.A., and Francis, P.W., 1993b, Thermal distributions at fumarole fields - Implications for infrared remote-sensing of active volcanoes: Journal of Volcanology and Geothermal Research, v. 55, p. 97-115.
- Oppenheimer, C., Rothery, D.A., Pieri, D.C., Abrams, M.J., and Carrere, V., 1993c, Analysis of airborne visible infrared imaging spectrometer (AVIRIS) data of volcanic hot-spots: International Journal of Remote Sensing, v. 14, p. 2919-2934.
- Oppenheimer, C., Lomakina, A.S., Kyle, P.R., Kingsbury, N.G., and Boichu, M., 2009, Pulsatory magma supply to a phonolite lava lake: Earth and Planetary Science Letters, v. 284, p. 392-398.
- Oppenheimer, C., Moretti, R., Kyle, P.R., Eschenbacher, A., Lowenstern, J.B., Hervig, R.L., and Dunbar, N.W., 2011, Mantle to surface degassing of alkalic magmas at Erebus volcano, Antarctica: Earth and Planetary Science Letters, v. 306, p. 261-271.
- Patrick, M., Dean, K., and Dehn, J., 2004, Active mud volcanism observed with Landsat 7 ETM+: Journal of Volcanology and Geothermal Research, v. 131, p. 307-320.
- Pavez, A., Remy, D., Bonvalat, S., Diament, M., Gabalda, G., Froger, J.L., Julien, P., Legrand, D., and Moisset, D., 2006, Insight into ground deformations at Lascar volcano (Chile) from SAR interferometry, photogrammetry and GPS data: Implications on volcano

- dynamics and future space monitoring: *Remote Sensing of Environment*, v. 100, p. 307-320.
- Pedersen, R., and Sigmundsson, F., 2006, Temporal development of the 1999 intrusive episode in the Eyjafjallajökull volcano, Iceland, derived from InSAR images: *Bulletin of Volcanology*, v. 68, p. 377-393.
- Pergola, N., Marchese, F., and Tramutoli, V., 2004, Automated detection of thermal features of active volcanoes by means of infrared AVHRR records: *Remote Sensing of Environment*, v. 93, p. 311-327.
- Pieri, D., and Abrams, M., 2005, ASTER observations of thermal anomalies preceding the April 2003 eruption of Chikurachki volcano, Kurile Islands, Russia: *Remote Sensing of Environment*, v. 99, p. 84-94.
- Pitman, E.B., Nichita, C.C., Patra, A., Bauer, A., Sheridan, M., and Bursik, M., 2003, Computing granular avalanches and landslides: *Physics of Fluids*, v. 15, p. 3638-3646.
- Prata, A.J., 1989, Infrared radiative transfer calculations for volcanic ash clouds: *Geophysical Research Letters*, v. 16, p. 1293-1296.
- Prata, A.J., Bluth, G., Carn, S.A., V.J.R., R., and Watson, I.M., 2012, Gas emissions from volcanoes, *in* Dean, K., and Dehn, J., eds., *Volcanoes of the North Pacific; Observations from space*, Springer Praxis.
- Prata, A.J., and Prata, A.T., 2012, Eyjafjallajökull volcanic ash concentrations determined using Spin Enhanced Visible and Infrared Imager measurements: *Journal of Geophysical Research-Atmospheres*, v. 117.
- Prata, A.J., Rose, W.I., Self, S., and O'Brien, D.M., 2003, Global, long-term sulphur dioxide measurements from TOVS data: A new tool for studying explosive volcanism and climate, *in* Robock, A., and Oppenheimer, C., eds., *Volcanism and the Earth's Atmosphere*, Volume 139: Washington, DC, American Geophysical Union, p. 75-92.
- Pritchard, M.E., and Simons, M., 2002, A satellite geodetic survey of large-scale deformation of volcanic centres in the central Andes: *Nature*, v. 418, p. 167-171.

- Ramsey, M., and Dehn, J., 2004, Spaceborne observations of the 2000 Bezymianny, Kamchatka eruption: the integration of high-resolution ASTER data into near real-time monitoring using AVHRR: *Journal of Volcanology and Geothermal Research*, v. 135, p. 127-146.
- Read, W.G., Froidevaux, L. and Waters, J.W., 1993. Microwave Limb Sounder measurement of stratospheric SO<sub>2</sub> from the Mt-Pinatubo volcano. *Geophysical Research Letters*, 20(12): 1299-1302.
- Realmuto, V., 1990, Separating the effects of temperature and emissivity: Emissivity spectrum normalization, 2nd TIMS Workshop: Pasadena, CA: Jet Propul. Lab, JPL Publication, p. 90-55.
- Rose, S., and Ramsey, M., 2009, The 2005 eruption of Kliuchevskoi volcano: Chronology and processes derived from ASTER spaceborne and field-based data: *Journal of Volcanology and Geothermal Research*, v. 184, p. 367-380.
- Ross, J.C., 1847, *A Voyage of Discovery and Research in the Southern and Antarctic Regions*: London, John Murray.
- Rothery, D.A., Francis, P.W., and Wood, C.A., 1988, Volcano monitoring using short wavelength infrared data from satellites: *Journal of Geophysical Research-Solid Earth and Planets*, v. 93, p. 7993-&.
- Sawyer, G.M., and Burton, M.R., 2006, Effects of a volcanic plume on thermal imaging data: *Geophysical Research Letters*, v. 33.
- Scientific Event Alert Network. Nevado del Ruiz. 1985. 05 and 07 (10).
- Smithsonian Institution. Bezymianny Weekly Reports. May 2010
- Smithsonian Institution, d. Láscar Eruptive History
- Spampinato, L., Oppenheimer, C., Cannata, A., Montalto, P., Salerno, G.G., and Calvari, S., 2012, On the time-scale of thermal cycles associated with open-vent degassing: *Bulletin of Volcanology*, v. 74, p. 1281-1292.

- Steffke, A.M., and Harris, A.J.L., 2011, A review of algorithms for detecting volcanic hot spots in satellite infrared data: *Bulletin of Volcanology*, v. 73, p. 1109-1137.
- Tassi, F., Aguilera, F., Vaselli, O., Medina, E., Tedesco, D., Delgado Huertas, A., Poreda, R., and Kojima, S., 2009, The magmatic- and hydrothermal-dominated fumarolic system at the Active Crater of Lascar volcano, northern Chile: *Bulletin of Volcanology*, v. 71, p. 171-183.
- Torrence, C., and Compo, G.P., 1998, A Practical Guide to Wavelet Analysis: *Bulletin of the American Meteorological Society*, v. 79, p. 61-78.
- Tramutoli, V., 1998, Robust AVHRR techniques (RAT) for environmental monitoring: theory and applications, *in* Cecchi, G., and Zilioli, E., eds., *Earth Surface Remote Sensing II*, Volume 3496: Proceedings of the Society of Photo-Optical Instrumentation Engineers (Spie), p. 101-113.
- Vaughan, R.G., and Hook, S.J., 2006, Using satellite data to characterize the temporal thermal behavior of an active volcano: Mount St. Helens, WA: *Geophysical Research Letters*, v. 33.
- Vaughan, R.G., Kervyn, M., Realmuto, V., Abrams, M., and Hook, S.J., 2008, Satellite measurements of recent volcanic activity at Oldoinyo Lengai, Tanzania: *Journal of Volcanology and Geothermal Research*, v. 173, p. 196-206.
- Vaughan, R.G., Keszthelyi, L.P., Davies, A.G., Schneider, D.J., Jaworowski, C., and Heasler, H., 2010, Exploring the limits of identifying sub-pixel thermal features using ASTER TIR data: *Journal of Volcanology and Geothermal Research*, v. 189, p. 225-237.
- Venzke, E., W., W.R., McClelland, L., Simkin, T., Luhr, J.F., Siebert, L., Mayberry, G., S., S., and (eds.), 2002-, *Global Volcanism, 1968 to the Present.*, Global Volcanism Program Digital Information Series, Smithsonian Institution.
- Watson, I.M., Realmuto, V.J., Rose, W.I., Prata, A.J., Bluth, G.J.S., Gu, Y., Bader, C.E., and Yu, T., 2004, Thermal infrared remote sensing of volcanic emissions using the moderate

- resolution imaging spectroradiometer: *Journal of Volcanology and Geothermal Research*, v. 135, p. 75-89.
- Wicks, C.W., Thatcher, W., Dzurisin, D., and Svarc, J., 2006, Uplift, thermal unrest and magma intrusion at Yellowstone caldera: *Nature*, v. 440, p. 72-75.
- Wooster, M.J., 2001, Long-term infrared surveillance of Lascar Volcano: contrasting activity cycles and cooling pyroclastics: *Geophysical Research Letters*, v. 28, p. 847-850.
- Wooster, M.J., Zhukov, B., and Oertel, D., 2003, Fire radiative energy for quantitative study of biomass burning: derivation from the BIRD experimental satellite and comparison to MODIS fire products: *Remote Sensing of Environment*, v. 86, p. 83-107.
- Wright, R., Flynn, L., Garbeil, H., Harris, A., and Pilger, E., 2002, Automated volcanic eruption detection using MODIS: *Remote Sensing of Environment*, v. 82, p. 135-155.
- Wright, R., and Flynn, L.P., 2003, On the retrieval of lava-flow surface temperatures from infrared satellite data: *Geology*, v. 31, p. 893-896.
- Wright, R., Flynn, L.P., Garbeil, H., Harris, A.J.L., and Pilger, E., 2004, MODVOLC: near-real-time thermal monitoring of global volcanism: *Journal of Volcanology and Geothermal Research*, v. 135, p. 29-49.
- Wright, R., Flynn, L.P., and Harris, A.J.L., 2001, Evolution of lava flow-fields at Mount Etna, 27-28 October 1999, observed by Landsat 7 ETM+: *Bulletin of Volcanology*, v. 63, p. 1-7.
- Wright, R., Garbeil, H., and Davies, A.G., 2010, Cooling rate of some active lavas determined using an orbital imaging spectrometer: *Journal of Geophysical Research-Solid Earth*, v. 115.
- Wright, R., Glaze, L., and Baloga, S.M., 2011, Constraints on determining the eruption style and composition of terrestrial lavas from space: *Geology*, v. 39, p. 1127-1130.
- Wright, R., and Pilger, E., 2008a, Radiant flux from Earth's subaerially erupting volcanoes: *International Journal of Remote Sensing*, v. 29, p. 6443-6466.

Wright, 2008b, Satellite observations reveal little inter-annual variability in the radiant flux from the Mount Erebus lava lake: *Journal of Volcanology and Geothermal Research*, v. 177, p. 687-694.

Yamaguchi, Y., Kahle, A.B., Tsu, H., Kawakami, T., and Pniel, M., 1998, Overview of Advanced Spaceborne Thermal Emission and Reflection Radiometer (ASTER): *Geoscience and Remote Sensing, IEEE Transactions on*, v. 36, p. 1062-1071.